# Invasion of soft active matter into capillaries
## A study of selected models and geometries

Felix Maria Kempf


München 2021

# Invasion of soft active matter into capillaries
# A study of selected models and geometries

**Felix Maria Kempf**

Dissertation
an der Fakultät für Physik
der Ludwig-Maximilians-Universität
München

vorgelegt von
Felix Maria Kempf
aus München

München, den 9. Februar 2021

Erstgutacher/in: Prof. Dr. Erwin Frey
Zweitgutachter/in: Prof. Dr. Julia Yeomans
Tag der mündlichen Prüfung: 19. März 2021

# Zusammenfassung

Die Physik aktiver Materie ist ein Teilgebiet der Physik, das sich mit so unterschiedlichen Systemen wie synthetischen selbstangetriebenen Kolloiden, Gruppen von kleinen Robotern, Mischungen von Biofilamenten und Motorproteinen, eukaryotischen Zellen, schwimmenden Spermien oder Bakterien und Tierschwärmen beschäftigt. Diese Systeme haben die gemeinsame Eigenschaft, dass sie aus einer großen Anzahl einzelner Teilchen bestehen, die unter Energieverbrauch angetrieben werden und stehen damit im Gegensatz zu "passiven" Teilchen, die sich nur durch Brownsche Bewegung bewegen. Verschiedene Modelle für solche Systeme wurden vorgeschlagen, einige mit dem Ziel, eine universelle Beschreibung für eine breite Klasse von Systemen aktiver Materie zu liefern, andere zugeschnitten auf bestimmte Beispielkonstellationen. Dazu gehören Kontinuumsmodelle, Modelle in Form von wechselwirkenden aktiv angetriebenen Einzelteilchen oder Beschreibungen von ausgedehnten Objekten mit interner Dynamik.

In dieser Arbeit werden zwei numerische Fallstudien von wachsender aktiver Materie, die durch die äußere Geometrie in ihrer Bewegungsfreiheit eingeschränkt ist, vorgestellt. Wir analysieren die Invasion eines aktiven Nematen in einen geraden Kanal mit einem hydrodynamischen Kontinuumsmodell und die Invasion eines zellulären Pottsmodells (CPM) für Epithelzellen in Kanäle mit konstantem oder variablem Durchmesser. Schlussendlich vergleichen wir die Ergebnisse beider Studien.

Die Arbeit ist in sieben Kapitel unterteilt:

**Kapitel 1 - Einführung**
Zu Beginn geben wir eine kurze Einführung in Systeme aktiver Materie und erörtern die Gründe, die für deren Untersuchung sprechen, sowohl aus Sicht der Physik als auch der Biologie. Wir motivieren daraus die Wahl der in dieser Arbeit gewählten Studien.

**Chapter 2 - Modelle kollektiver Bewegung**
In diesem Kapitel geben wir einen kurzen Überblick über verschiedene theoretische Ansätze zur Untersuchung von Systemen aktiver Materie und vergleichen diese zueinander.

**Kapitel 3 - Eindringen aktiver Materie in eine Kapillare**
*gemeinsam mit Romain Mueller, Erwin Frey, Julia M. Yeomans und Amin Doostmohammadi.*
Biologisch aktive Materialien wie bakterielle Biofilme und eukaryotische Zellen wachsen in begrenzten mikroskopischen Räumen. Wir zeigen durch numerische Simulationen, dass Begrenzung als mechanische Führung dienen und zu verschiedenen Moden kollektiver Invasion führen kann, wenn sie mit der Wachstumsdynamik und der intrinsischen Aktivität biologischer Materialien zusammen spielt. Wir analysieren die Dynamik einer wachsenden Grenzfläche zwischen aktiver Materie und einer umgebenden Flüssigkeit in einem Kanal und klassifizieren die auftretenden Moden kollektiver Invasion basierend auf der Aktivität der Teilchen, die diese wachsenden Materie bilden. Während bei kleinen und mittleren Aktivitäten das aktive Material als zusammenhängende Einheit wächst, stellt sich heraus, dass sich oberhalb einer gewissen Aktivitätsschwelle kleine Verbunde davon aus dem Hauptfeld lösen. Wir charakterisieren außerdem die mechanischen Mechanismen, die den Übergängen zwischen den verschiedenen Invasionsmoden zugrunde liegen und quantifizieren deren Einfluss auf die Geschwindigkeit der Invasion insgesamt. Eine Momentaufnahmen einer solchen Simulation ist zur Veranschaulichung links in Abbildung 1 dargestellt. Dieses Kapitel wurde in [1] veröffentlicht.

**Kapitel 4 - Filme und Tröpfchen: aktive Materie auf einer Oberfläche**
Unter Verwendung des gleichen Modells wie in Kapitel 3 beschreiben wir das Verhalten von Filmen und Tröpfchen aus einem aktivem Material auf einer ebenen Oberfläche. Diese vereinfachten Anordnungen erlauben es uns, die Besonderheiten aktiver Flüssigkeiten im Vergleich zu analogen Systeme im thermischen Gleichgewicht zu untersuchen. Wir finden heraus, dass der Endzustand des Systems im Allgemeinen von der Stärke der aktiven Kräfte abhängt. So werden Filme oberhalb einer bestimmten

Aktivitätsschwelle instabil. Tröpfchen können einen stationären Zustand erreichen, in dem die Form und die innere Struktur des Tröpfchens durch die Stärke der Aktivität bestimmt ist. Wir können zeigen, dass dieser stationäre Zustand durch ein Gleichgewicht von Advektion durch aktive Kräfte und Diffusion bestimmt wird.

**Kapitel 5 - Intermezzo: Zelluläre Systeme als aktive Materie**
Bevor wir in Kapitel 6 ein Modell für kollektive Zellmigration untersuchen geben wir einen kurzen Überblick über die Eigenschaften von sich koordiniert bewegenden Zellen und erklären, warum sie als aktive Materie betrachtet werden können.

**Kapitel 6 - Zelluläres Pottsmodel in einem Flaschenhals**
*mit Andriy Goychuk und Erwin Frey.*
Zellmigration ist von großer Bedeutung für das Verständnis von Phänomenen wie Morphogenese, Metastase bei Krebserkrankungen oder Wundheilung. In diesen Situationen ist die Bewegunsfreiheit der Zellen oftmals durch Hindernisse beschränkt. In dieser Arbeit zeigen wir anhand von Computersimulationen mit einem zellulären Pottsmodell (CPM), dass das Vorhandensein einer Engstelle in einem ansonsten geraden Kanal großen Einfluss auf die interne Organisation einer eindringenden monozellulären Schicht und die Bewegung einzelner Zellen darin hat. Vergleichbar mit Zuständen in Gläsern oder viskoelastischen Materialen stellen wir fest, dass die Zellschicht gleichzeitig Eigenschaften von klassischen Festkörpern und klassischen Flüssigkeiten aufweist. Die lokale Ordnung entspricht im Mittel einem regelmäßigen hexagonalen Gitter, während die relative Bewegung der Zellen nicht beschränkt ist. Im Vergleich zu einem Kanal ohne Verengung beobachten wir, dass eine Engstelle die Bildung regelmäßiger hexagonaler Anordnungen im Epithel bremst und zu einer Ansammlung und einem rückwärts gewandten Fluss von Zellen vor der Engstelle führt, wodurch auch die Invasionsgeschwindigkeit in ihrer Gesamtheit beeinflusst wird. Diese Phänomene hängen in ihrem Ausmaß von den Abmessungen der verschiedenen Kanalabschnitte sowie von der Form des Trichterbereichs ab, der die breiteren mit den engeren Teilbereichen verbindet. Eine typische Situation ist in Abbildung 1 auf der rechten Seite dargestellt.

**Kapitel 7 - Schlussfolgerungen**
Zum Abschluss vergleichen wir die Ergebnisse der beiden in dieser Arbeit vorgestellten Studien zum Invasionsverhalten aktiver Materie und arbeiten die grundlegenden Unterschiede der beiden verwendeten Modelle heraus. Ausgehend davon schlagen wir den Bogen zur Einleitung und stellen diese Ergebnisse in den größeren Kontext der Erforschung aktiver Materie.

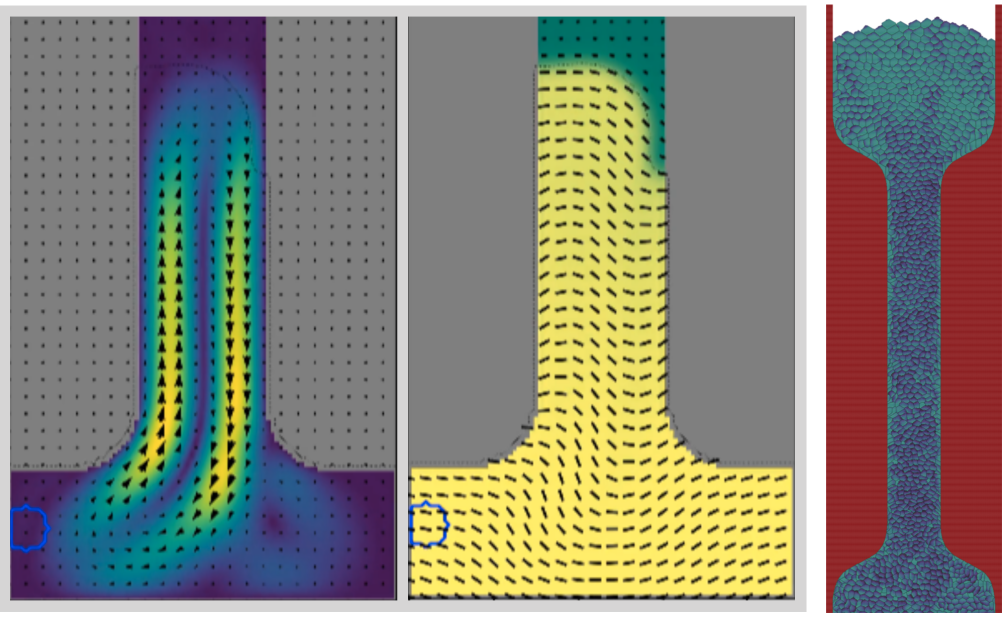

**Abbildung 1** *Momentaufnahmen der Systeme aus den Kapiteln 3 und 6.*
*Linke Seite:* Momentaufnahme der Invasion des aktiven Nematen in einen geraden Kanal. (links: Geschwindigkeitsfeld, rechts: nematische Ordnung). *Rechte Seite:* Epithelzellen, simuliert mit einem zellulären Pottsmodell, durchqueren eine flaschenhalförmige Anordnung.

# Summary

Active matter physics is a field concerned with systems as diverse as synthetic self-propelled colloids, groups of small robots, mixtures of biofilaments and motor proteins, eukaryotic cells, swimming sperm or bacteria, and animal flocks. These have the common property that they are composed of a large number of individual constituents that are propelled under the consumption of energy in contrast to "passive" particles that only move by Brownian motion. Various models have been proposed for such systems, some aimed at offering a universal description for a broad class of active matter systems, some tailored to specific example setups. These include continuum models, models in terms of interacting actively driven single particles or descriptions of extended objects with internal dynamics.

This work presents two computational case studies of growing active matter constrained by geometry. We analyse the invasion of an active nematic into a straight channel with a hydrodynamic continuum model and invasion of a Cellular Potts Model (CPM) for epithelial cells into channels with constant or varying diameter. Finally, we compare the results of both studies.

The thesis is divided into seven chapters:

**Chapter 1 - Introduction**
In the beginning, we give a short introduction into active matter systems and discuss reasons for their study from a physics as well as a biology perspective. We also motivate the choice for the studies picked in this thesis.

**Chapter 2 - Modelling collective motion**
In this chapter, we briefly review and relate different theoretical approaches to studying active matter systems.

**Chapter 3 - Invasion of active nematics into a capillary**
*With Romain Mueller, Erwin Frey, Julia M. Yeomans, and Amin Doostmohammadi.*
Biological active materials such as bacterial biofilms and eukaryotic cells thrive in confined microspaces. We show through numerical simulations that confinement can serve as a mechanical guidance to achieve distinct modes of collective invasion when combined with growth dynamics and the intrinsic activity of biological materials. We assess the dynamics of the growing interface between an active material and a surrounding fluid in a capillary and classify these collective modes of invasion based on the activity of the constituent particles of the growing matter. While at small and moderate activities the active material grows as a coherent unit, we find that blobs of active material collectively detach from the cohort above a well-defined activity threshold. We further characterise the mechanical mechanisms underlying the crossovers between different modes of invasion and quantify their impact on the overall invasion speed. A simulation snapshot is shown on the left side of Figure 1 for illustration. This chapter has been published in [1].

**Chapter 4 - Films and droplets: active matter on a wall**
Employing the same model as in chapter 3, we describe the behaviour of films and droplets of active material on a flat surface. These simplified configurations allow us to investigate the features of active fluids in comparison against analogous systems in thermal equilibrium. We find that the final state of the system in general depends on the strength of active forces: films become unstable above a certain activity threshold and droplets can reach a steady state, in which the shape and the internal structure of the droplet are related to activity. This steady state can be shown to be determined by a balance of advection caused by active stresses and diffusion.

**Chapter 5 - Intermezzo: Cellular systems as active matter**
Before studying a model for collective cell migration in chapter 6, we give a brief overview on the properties of systems of collectively moving cells and how they can be regarded as active matter.

**Chapter 6 - Cellular Potts Model in a bottleneck**

*With Andriy Goychuk and Erwin Frey.*

Cell migration is of major importance for the understanding of phenomena such as morphogenesis, cancer metastasis, or wound healing. In many of these situations cells are under external confinement. In this work we show by means of computer simulations with a Cellular Potts Model (CPM) that the presence of a bottleneck in an otherwise straight channel has a major influence on the internal organisation of an invading cellular monolayer and the motion of individual cells therein. Comparable to a glass or viscoelastic material, the cell sheet is found to exhibit features of both classical solids and classical fluids. The local ordering on average corresponds to a regular hexagonal lattice, while the relative motion of cells is unbounded. Compared to an unconstricted channel, we observe that a bottleneck perturbs the formation of regular hexagonal arrangements in the epithelial sheet and leads to pile-ups and backflow of cells near the entrance to the constriction, which also affects the overall invasion speed. The scale of these various phenomena depends on the dimensions of the different channel parts, as well as the shape of the funnel domain that connects wider to narrower regions. A typical situation is shown Figure 1 on the right side.

**Chapter 7 - Conclusions**

To conclude, we compare findings from the two invasion studies presented in this thesis and work out the fundamental differences in both models used. Based on this, we close the loop to the introduction and put these results in the context of active matter research.

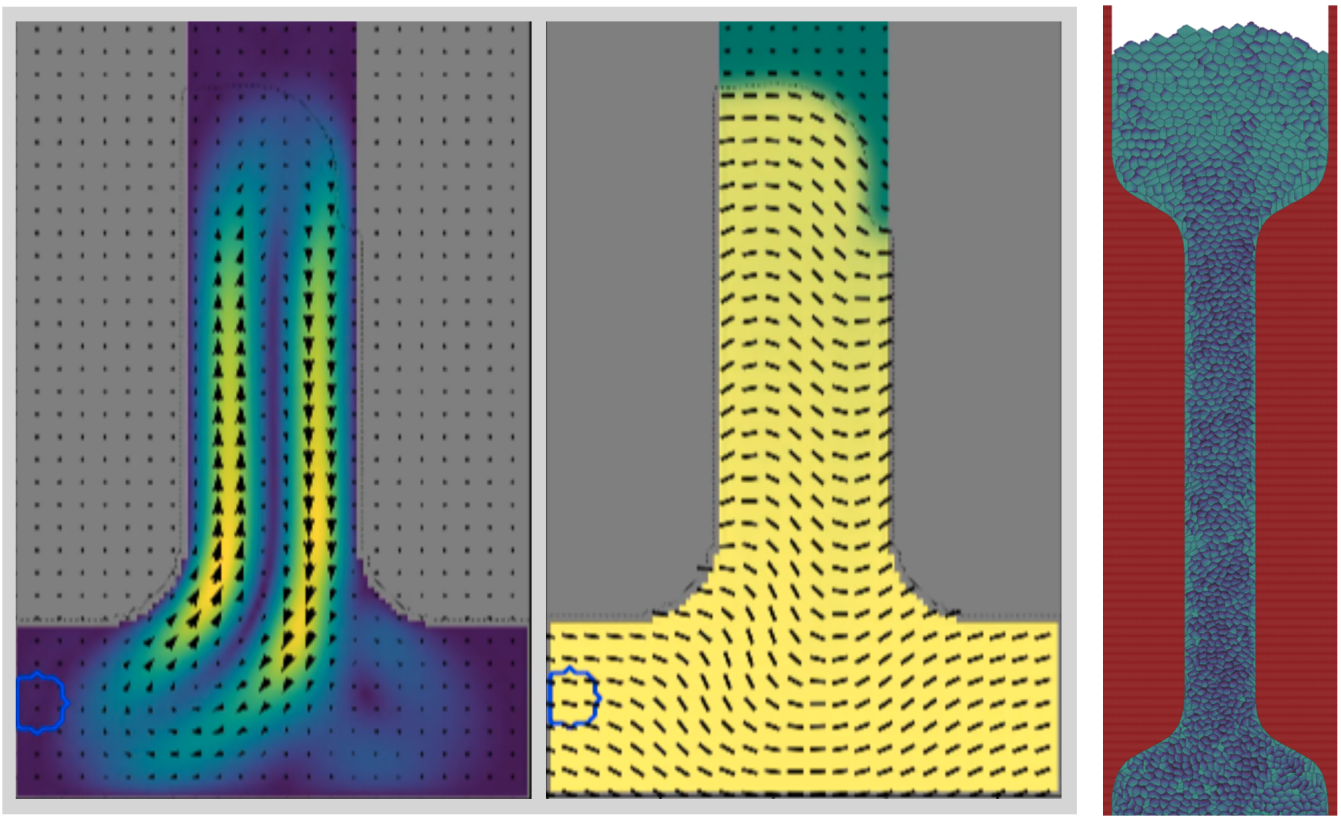

**Figure 1** *Screenshots of systems investigated in chapters 3 and 6.*
*Left panel:* screenshot of invading active nematic into a straight channel (left: velocity field, right: nematic order). *Right panel:* Epithelial cells simulated with a cellular Potts model (CPM) passing through a bottleneck configuration.

# Contents

# 1 Introduction

*Die Wissenschaft von heute ist der Irrtum von morgen.*
*Today's science is tomorrow's error.*
— Jakob Johann von Uexküll

The field of active matter is a relatively young one in physics. Its object of study are systems composed of particles that are *active*, here specificallly meaning that they generate forces[2–4]. Such *local* force generation means that energy is pumped into the system *locally* driving it away from thermal equilibrium. Therefore, active systems are a special type of non-equilibrium systems. In many cases, systems under study consist of a large number of constituents that are small compared to the size of the full system (and in this sense are often called *microscopic*). Fields traditionally concerned with many-particle systems are condensed matter physics and statistical mechanics. Hence, models and methods from these fields are often adapted to investigate active matter systems.

This very open definition fits many different realisations of systems in the laboratory as well as outside of it to be regarded as active systems (see for example the reviews: [4–9]). There are synthetic examples like vibrated granules, colloids that are propelled by electromagnetic forces or chemical reactions, or groups of small robots that drive around on surfaces. Yet, the main interest in the topic comes from the various biological examples of active systems across various scales: cytoskeletal structures, mixtures of biofilaments and motor proteins, collections of eukaryotic cells, swimmers like sperm or bacteria, bacterial colonies, but also flocks of insects, mammals, fish, or birds. The reader interested in more exhaustive and detailed descriptions of different examples for active systems is referred to the works referenced above and below (and the works referenced therein).

Because of its applicability to biological systems, the long-term vision of many researchers is that active matter could deliver "a theory of the mechanics and statistics of living matter with a status comparable to what's already been done for collections of dead particles." (Siriam Ramaswamy, cited after [3]).

This touches on the central question on which I want to give some thoughts in the next section 1.1: *why study active matter?* With the arguments given there in mind, I then want to give an outlook on the research presented in this thesis (section 1.2), before we will look into the different ways of modelling active systems in chapter 2.

## 1.1 Why study active matter?

A good overview over prominent voices from the field on why they are interested in active systems can be found in [3]. My personal impression is that sometimes too little time is spent on reflecting about the intentions behind the study of active matter. The following is a rather personal account on that from my side where I would like to present and briefly explain three possible reasons.

**Exploring the rich phenomenology.** Active systems in their various realisations show a wide range of phenomena which cannot be observed in comparable non-active systems, i.e. systems in thermal equilibrium. Exploring, characterising, and categorising this richness is interesting in itself and sustained by ongoing technical progress, e.g. in microscopy and growing experience in experimental techniques. Besides directed research with a certain research question to answer or hypothesis to test, explorative research is an important part of science. Among the properties of active systems that are interesting from the physicist's point of view are:

- Large density fluctuations[10–15].
- Phase separation (then called *motility-induced phase-separation*) and various effects like trapping or sorting of swimmers connected to the breaking of detailed balance[7, 16, 17].
- Spontaneous symmetry breaking into strongly correlated motion, either polarised into one direction (then called *flocking*)[12–14, 18–23] or in opposing directions along lanes[24].
- Glass-like dynamics[25–29].
- Complex spatio-temporal patterns including defect dynamics and turbulence[22, 30–37].

This richness in experimental observations is complemented by the richness in models that we will discuss in chapter 2. The interplay between both, theory and experiment, can spark new ideas for investigations.

The research presented in this thesis is mainly motivated in this sense, at least in my view. Although we have potential biological systems in mind, where our research could be of interest, it is mainly about testing out existing models in new settings, as will be explained in section 1.2.

**The (theoretical) physics aspect: active matter systems as non-equilibrium model systems.** Historically, physicists have been very successful in describing systems at or close to thermal equilibrium: Starting in the 19th century with abstract

descriptions of heat engines an impressive apparatus of thermodynamics, statistical physics, fluid dynamics, etc. has been evolved to describe all sorts of different systems[38–40]. Specifically with the works of Onsager[41, 42], also methods for non-equilibrium physics have been developed. However, these do not work "too far away" from thermal equilibrium. Actually, equilibrium systems are rather a special case and large parts of our world are out of equilibrium, among that most of what we call "living".

Now, from a theoretical perspective it is of course a pressing question to find ways to describe non-equilibrium systems and in particular to nail down differences between equilibrium and non-equilibrium systems. Here, active matter physics provides a broad range of experimental as well as computational model systems.

In this sense, active matter systems serve as example systems in the endeavour to find criteria that can be used to classify non-equilibrium systems[43–45]. Various works discuss whether and how concepts known from equilibrium statistical physics like phases, temperature, pressure, fluctuation-dissipation theorems, or equations of state can be generalised or reformulated in order to be useful for the understanding of active matter[46–53].

All this work can not only lead to a better understanding of the active matter systems themselves, but in the best case leads us to a more profound understanding of statistical physics and thus the systems it describes in general. It might also open new perspectives on equilibrium systems as a special case of a more general class of systems.

**The biology aspect: towards a theory of living matter?** This approach is complementary to the last one although this difference is often overlooked: While from the physics perspective the idea was to use biological or biochemical systems to gain insights about genuinely physical questions, the biological side of the question is: can we use the methods from physics to gain understanding of living organisms? It should be clear that this is not at all the same question as both professions follow different research questions. While for example, finding an equation of state for active systems would be a great achievement for physics, most biologists would probably not judge it as too useful for their work. They traditionally look at living systems from a different perspective and are more interested in functional relations specific to the organisation and development of life than in universal statistical quantities.

At first glance, using the physics toolbox to analyse biological systems seems a very good idea as these techniques have shown great success. Although there are many examples where this has worked out very well (e.g. the studies of Purcell on bacterial swimming[54] or the quantitative methods employed by Luria and Delbrück that helped proofing the mutation-selection based theory of evolution[55]), I want to bring forward potential limitations to this idea.

There is the saying: *if you have a hammer everything looks like a nail*. The tools you use affect how you see a system. This is not a principal limitation, but one has to be aware of the danger of trying to analyse or model a system with methods that do not really fit for the system and research question just because one is very convinced of these methods from experiences in other fields.

A deeper problem maybe lies in the fundamental difference between both fields, put in one phrase: *physics is reductionist while biological systems are inherently complex*. *Complexity* of course is a difficult and rather vague term, but the general idea is the following: physics often allows explanations that are based on few fundamental effects (e.g. model of the electronic structure of the hydrogen atom) that still deliver results that are very close to the real experimental observations (e.g. spectrum of the hydrogen atom). Such models can be sufficient to deliver a basic understanding of more complex systems (e.g. spectra of higher elements may not be computed exactly analytically, but their appearance can be understood). It has turned out to work beautifully to strip down systems to a "minimal core" and use highly idealised models to explain the guiding principles of the whole larger system. This allows reduction of complexity by simplification and approximation. Just think of very simplistic concepts like the harmonic oscillator that is useful in many different situations.

Additionally, the way systems are treated in physics is highly reductionistic. With this I mean the idea that systems can be deconstructed in parts between which the interaction - as a very good approximation - is negligible compared to the effects of the parts of the systems. Assuming this, you can understand the system by analysing and understanding suitably chosen subsystems independently and then taking together the results from these analyses. In other words, physical models are often "linear" or different effects are thought as approximately independent or "orthogonal". Taking equilibrium thermodynamics as an example: due to the convenient fact that equilibrium systems can be described by thermodynamic potentials, it works nicely to consider changes in two appropriately chosen variables (e.g.volume and temperature) independently in an idealised quasistatic process, even though they might occur simultaneously. This reasoning is also fundamental for perturbation theory that is applied across all fields of physics. The perturbation is assumed to come "on top" of the unperturbed system, e.g. if a Hamiltonian determines the dynamics, the perturbative Hamiltonian is simply added to the unaltered Hamiltonian for the unperturbed system.

Physicists are used to these methods working out. Actually, this is not at all natural and many past and present thinkers were trying to understand why this is the case[56], a prominent example is Eugene Wigner[57]. Even more, one has to be very careful when transferring these methods to other fields of science where there is no experience with their application. The problem is blind utilisation of methods from physics in other fields that just do not allow such simplification. Such mistakes

have been made in the application of idealised mathematical models, often inspired by models from physics, to financial markets. A very prominent example is the Black-Scholes formula for option pricing: Wrong assumptions on the stochastic properties of the system led to failure of the model and major financial turbulences in the real world[58]. In general, there are fundamental concerns whether at all modelling is a sensible approach to systems like financial markets that are dominated by large fluctuations and a large number of complex interactions[59, 60].

Furthermore, physics laws have often found to be highly universal: Navier-Stokes equations work for all kinds of chemically different one-component fluids or many different materials follow exactly the same scaling at phase transitions, only a few *material parameters* have to be adapted. The success of these and other theories has led to the idea that nature's laws are universal being deeply engraved in the thinking of many physicists. Also many models for active matter are derived from simple assumptions and hence some physicists seem to believe that they could serve as a universal theory for living systems, as Ramaswamy's quote at the beginning of this chapter might suggest. This however silently assumes that biological, or more general active, systems also follow universal laws. This actually is a strong assumption taking into account the diversity and complexity of biological systems like bacterial colonies or the internal workings of a single cell.

From all these aspects, I will try to draw a conclusion. As mentioned above, applying methods from physics to biological systems has been successful, but organisms and their interactions are a very diverse and complex field and it is not clear how far the deconstructivist methods and the idealised models of physics will carry. For active matter physics, this means that there probably will not be a universal theory to describe all collective phenomena in biology, but it can still contribute to the understanding of certain systems. A very good example is how a model of single particles with simple interaction rules developed in the context of active matter helped to understand the key mechanisms that govern swarm behaviour in real starling flocks[61]. However, the same study also found problems with matching quantitative predictions from the model to their experiments: As the authors put it: "This dialectic between highly detailed versus ultrasimplified models is a very typical trait of the somewhat complicated relationship between biology and physics. In our opinion, the core of the problem is that there is a sort of trade-off between predictive power and understanding." This introduces another aspect: what to expect from models? And maybe this is the key aspect to the question of the purpose of active matter theories in biology. Even though a universal theory of living systems might not be feasible, active matter theory still could help in at least two ways: providing general, (to a certain degree) universal theories that help the understanding of key mechanisms but lack quantitative predictive power on the one side and delivering quantitative, but less general models that are specifically tailored to certain systems on the other.

I hope that I could convince you that active matter physics is a valid field of research for several reasons, but also that it is important to become aware of your goals in the process. Do I want to use biological systems as model systems to answer physics' questions or do I want to use tools from physics to make progress in biological problems? Or do I just want to explore the fascinating variety of phenomena? The answer to these questions can affect the choice of appropriate experiments and theoretical models although, of course, intentions can overlap. In the context of biologically motivated research, additional dangers are lurking. As a physicist one has to be very attentive to the interests of biologists and their way of thinking. Only if one is critical of its own assumptions and habits acquired during the study of physics, such projects can be successful. In the same way one has to become aware of the possible limitations of the physics toolbox when applied to biological systems that might be fundamentally different in important aspects.

## 1.2 Motivation and outline of this thesis or: why active matter and geometry?

As outlined before, there are plenty of open directions in active matter research. Among these, one is the interaction of different types of active matter with external structures or the dynamics of active matter under confinement. Examples are as diverse as:

- single or several microswimmers close to a wall or in environments with obstacles[7, 62–66],
- *in-vitro* experiments in channel-like geometries with epithelial cells[67–74], bacteria[23, 75, 76], and mixtures of biofilaments and molecular motors[36, 37, 77, 78],
- spontaneous emergence of flow in cells confined to rectangular or circular geometries[73, 79],
- and related *in-vivo* phenomena like guidance by surrounding tissue in cancer cell migration[80, 81] and substrate-interaction in biofilm formation[82, 83].

The work presented in this thesis mainly consists of two different computational case studies concerned with the interplay between geometric confinement and growth in active matter. Growth is another property present in many biological active systems: under the appropriate conditions bacteria and eukaryotic cells proliferate on timescales that are comparable to the duration of experiments or physiological processes (doubling times on the order of hours to days). This is an essential factor in morphogenesis, cancer metastasis[84–86], or spreading of bacteria[87–89]. We

use two different models, a continuum model for an active nematic and a Cellular Potts Model for epithelial cells, and analyse their behaviour in different invasion setups where active matter grows into a confined environment.

In the sense of the previous section, the motivation is thus twofold: The main goal is the exploration of further properties of established models, which are already proven to describe certain aspects of experimental systems correctly, by simulating them in new setups. However, we also hope that our work sparks new ideas for the analysis of experimental data and contributes to an improved understanding of the mechanisms relevant to experiments where active matter is found in comparable configurations.

In the next chapter, we will give an overview over existing approaches to modelling active matter. In chapter 3, we then present the first invasion study of an active nematic into a straight channel. Here the focus lies on the interplay between flow-fields, the shape of the invasion front, and overall invasion speed. After that, in chapter 4, we want to investigate a simpler setup and briefly look into films and droplets of an active nematic on a flat surface with a no-slip boundary-condition. Although not concerned with growth and invasion, this is a good way to show certain properties of the model used in comparison to thermal systems.

As a short introduction to the second part where a computational Cellular Potts Model is used that is tailored to simulating cellular systems, we will discuss how specifically cells can be seen as active matter in chapter 5. Then in chapter 6, we will present our simulations of a cellular sheet invading into a channel of varying diameter before attempting a summary for the whole thesis in chapter 7.

# 2 Modelling collective motion

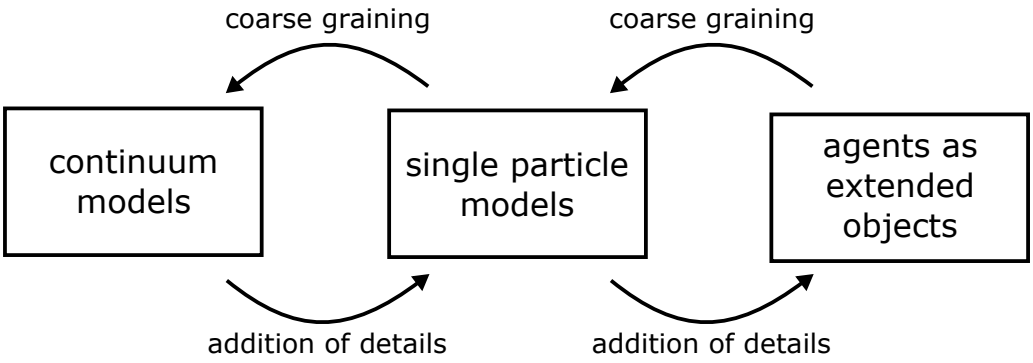


**Figure 2.1** *Schematic illustration of the relations between model classes.* Continuum models describe systems on larger scales. More detailed descriptions of individual agents require more refined concepts of the mechanisms they follow. These mechanisms have to be defined explicitly. Similarly, when single particle models are extended to models of extended objects with internal structure. Then, rules have to be established that regulate the shape and the internal structure. In the other direction, at least in principle, it should be possible to replace explicitly defined mechanisms by effective, and more "simple" interactions, and arrive at a model for larger scales. This procedure is known as coarse-graining. Performing coarse-graining explicitly for a given microscopic model can be difficult and ambiguous, so often equations are derived from general assumptions (e.g. the symmetries of the system) or constructed semi-phenomenologically. Then this connection is more of hypothetical nature.

As outlined in the introductory chapter 1, there is no single established "grand theory" for active matter. In contrast, there are various different approaches to studying active matter by means of mathematical modelling. Which one to choose depends on the system to describe and the purpose of the investigation, i.e. which of the system's properties should be reproduced and whether the goal is an exact reproduction of results or just providing a qualitative explanation of observations: different models have different strengths and weaknesses and show different phenomenology.

Many models start from the traditional idea of condensed matter physics that matter is built up from many interacting constituents[38]. These can be extended and have internal structure as in Cellular Potts Models (CPM) or phase field models discussed in section 2.3. Alternatively the constituents might be seen as particles without internal structure whose present internal "state" is represented by numbers,

not fields. This class of models stands at the very beginning of active matter models with the works by Vicsek *et al.*[18] and is presented in section 2.2. Conceptually it should be possible to come from models with internal structures of the constituents to single particle models by *coarse-graining*, i.e. by looking at the system at a coarser scale where the internal dynamics are not resolved but can be summarised in *effective* scalar state variables.

One step further, at an even coarser scale, single particles are not resolved anymore at all and matter is described as a continuum, or a field. Observables are then macroscopic field variables. These can be seen as local averages over microscopic quantities. Naturally, single particle dynamics can not be described anymore. Such models are sometimes derived by coarse-graining from descriptions of systems based on individual constituents[90–93], but doing so explicitly can be difficult. More often, continuum models are therefore set up semi-phenomenologically or from fundamental properties like conservation laws and symmetries. Ideally, continuum models should be the most general ones as "microscopic" properties of the system are not explicitly present anymore. As such, many different microscopic models should lead to the same continuum model. Features of systems differing at the microscale should then show up as different values for material constants in the contiuum model, but not lead to a different mathematical structure of the model as long as the microscopic models are sufficiently related. A short discussion of continuum models will be presented in section 2.1. However, this does not necessarily mean that continuum models are "simpler". They can carry a lot of constants and unintuitive higher order terms. The connections between different model types are also illustrated in Figure 2.1.

There are other models for active matter that can be fit into this classification, also models can be categorised differently, of course. Important properties of models are embodied symmetries, types of interaction, existence of time-reversal symmetry, or conserved quantities. For example, momentum-conserving models are called *wet* models, because momentum conservation is facilitated by a fluid that surrounds the active components. Not momentum-conserving models in contrast are called *dry*. A very good review that covers many models of all different types is [94]. More detailed information can be found there, in the following I will just give an overview.

## 2.1 Continuum models

In continuum models, or field theories, physical quantities $X$ are described as spatial- and time-dependent fields $X(\mathbf{r}, t)$. The time evolution of these observables is then determined by partial differential equations (PDEs): $\partial_t X(\mathbf{r}, t) = ...$ where the right hand-side in principle can be any function of the observables and their spatial derivatives (of any order). What quantities are considered depends on the

systems under consideration. If the right hand-side cannot be fully determined from a microscopic model, often general physical principles are invoked to make educated guesses. Such principles can be conservation laws, very often symmetry considerations, or detailed balance conditions. Also stochasticity can be introduced by adding noise terms making the PDEs Langevin equations.

For example in the well-known Navier-Stokes equations, the observables are density, velocity and pressure. The equation is then determined by thermodynamic principles and the conservation of fluid mass (Onsager theory[41, 42]). The same observables also appear in many active matter models, but there are much more options. Different types of active matter field theories derived in this way can be categorised with the *Halperin-Hohenberg classification*. A good and very intelligible overview of these and how they compare to "classical" ones can be found in [95].

Historically, an early continuum model was defined by Toner and Tu[19–21]. It was motivated with describing *polar flocks*, like bird flocks and is in close connection to a single particle model presented in section 2.2. In essence it describes self-propelled particles that move unidirectionally and influence each other in a way that they align their direction of motion. Hence, the main observable, next to particle density, is a vector describing the travelling direction of the flock at a certain location. The model in two dimensions is similar to the $2D$ XY model[38]. Apart from that, it was rather motivated by heuristic and symmetry arguments, not systematically derived. The Toner-Tu model shows interesting properties like an order-to-disorder phase transition or sound-wave propagation. It was also due to these unexpected findings that active matter became as popular as it is by now. Later extensions had even richer phenomenology like anormalous turbulence[96]. It was successfully applied to experimental sytems, like driven colloids[14] or bacterial swarms[31, 97]. Similar reasoning as for the Toner-Tu model can be applied to models for other systems with observables of different symmetry (scalar, tensorial) or with a background fluid present[95, 98].

One way to derive field equations for self-propelled particles from microscopic principles is via a Boltzmann equation[99–106]. The Boltzmann equation describes the evolution of the one-particle phase-space distribution $f(\mathbf{r}, \theta, t)$ where $\theta$ denotes the particle orientation. The time evolution of this density is then determined by advection in the direction of particle motion, diffusion, and particle-particle interactions. Macroscopic observables $X(\mathbf{r}, t)$ are obtained as expectation values over the single-particle density and the corresponding time-evolution equations can be derived from the PDE for $f(\mathbf{r}, \theta, t)$, e.g. for the particle density $\rho(\mathbf{r}, t) = \int \mathrm{d}\theta \; f(\mathbf{r}, \theta, t)$. Alternatively one can solve directly for $f(\mathbf{r}, \theta, t)$ with numerical methods[107, 108].

Another systematic approach is to start from fundamental conservation laws to derive fundamental equations for mass, energy, momentum, angular momentum, and entropy in a system assumed to be close to equilibrium[109, 110]. Then,

activity can be implemented in a systematic way by means of Onsager relations[41, 42]. With these and the choice of a free energy for the system, a plethora of different hydrodynamic systems can be designed. The resulting equations can be seen as generalised Navier-Stokes equations with additional observables. The limitation is that only linear extensions from equilibrium are possible in this framework. The derivation is presented in detail with examples in [110].

One theory that can be obtained through such considerations is the theory of active nematics[111–113]. These models are inspired by the nematic phase of liquid crystals and extended by an active stress term that mimics microscopic dipole forces. As such, in contrast to the Toner-Tu model, the order parameter here is not a vector but a tensor that is invariant under rotations of 180°. The model is motivated by assemblies of microswimmers like sperm or bacteria whose flagellar motions produce dipolar force fields[114]. Meanwhile, the model has been successfully applied to various experimental systems: bacteria[115], mixtures of biofilaments and molecular motors[8, 30], and several types of eukaryotic cells[35, 116, 117]. Characteristic for this model is the formation of $\pm 1/2$-valued defects whose dynamics are distinct from equilibrium systems due to the active forces[118–124]. That is well matched in experiments[30, 32, 121]. For higher activities, the defects also play an important role in the model's transitions to low Reynolds-number turbulence, a class of turbulence peculiar to active systems and distinct from the commonly known high Reynolds-number (inertial) turbulence[37, 120, 125–127]. Motivated by the generality of this model, we use it for our studies in chapters 3 and 4 where we investigate the behaviour of active matter in different situations of confinement. More detailed explanations can be thus found in chapter 3.

## 2.2 Single particle models

Hand in hand with the continuum models, models simulating individual active particles were developed[7]. These models often rely on direct computational implementation where the trajectories of all particles are simulated and statistical quantities are calculated directly from these. However, they can also be used as a foundation to derive field theories, as mentioned before[92].

A simple version of a single particle model are active Brownian particles[128]. In contrast to particles that follow the laws of diffusive Brownian motion, active Brownian particles in addition also move by active self-propulsion. Technically, these models are usually fomulated in terms of a Langevin equation. In the simplest case this can be implemented as a particle with constant velocity $v_0$ whose direction of locomotion is subject to rotational diffusion, but also more complicated mechanisms are possible. A prominent example is so-called run-and-tumble motion where periods of directed motion are stochastically interrupted by *tumbling events* where the particle

chooses a new random orientation for its further path[16]. To mimic the strategies of bacteria when searching for nutrients or other chemotactic organisms, the rate of reorientations can in addition be coupled to an external field[54]. Interestingly, active Brownian particles and run-and-tumble dynamics can lead to equivalent physical behaviour at macroscopic scale under certain conditions[104]. These models allow large freedom in defining interactions between individual particles. This includes interactions via potentials that can be spherical or tailored to particles of different shape, but also inelastic collisions[94].

Corresponding to this variety in definitions, these models show a rich phenomenology, for example complex phase-behaviour and transitions[129] and defects in high-density phases[130]. A classical observation is motility-induced phase-separation (MIPS): beyond a certain activity, the system spontaneously separates into a high-density phase and a low-density, gas-like phase[16, 52, 104, 131–133].

While the interactions between particles in the active Brownian models are largely "physical", in principle interactions can also be defined phenomenologically. An example for this are Viscek-type models with an effective alignment-interaction between particles that are motivated by natural flocks[12, 18]. Here, particles adopt the mean orientation of the particles in their vicinity, whereupon variations are possible: the criterion that defines *vicinity* can be metric (all particles closer than a certain distance) or topological (closest $n$ particles), alignment can be polar or nematic, and additional interaction potentials can be added[94]. The most striking property of Vicsek-type models, that also is at the origin of the large interest in them, is the spontaneous flocking transition: Regulated by system noise and particle density, particles form coordinated "flocks" of high density and identical orientation that span the full system. This transition faithfully appears in Viscek models, however the exact nature of the transition (continuous or discontinuous) depends on the details of the interactions in the model. The aforementioned Toner-Tu contiuum theory[19–21] is closely related to Vicsek models and produces similar coordinated motion. It is also the model mentioned in the introduction that was used in the study of starlings[61].

Closer to real physical systems are models that in detail implement the mechanisms of biological or artificial microswimmers in their surrounding fluid[54, 64, 134–137]. These models are significantly more complex as hydrodynamic simulation of the fluid is required, but relevant in the understanding of real biological examples as e.g. bacteria or sperm live in liquid environments.

In general, as Langevin equations are easy to solve with present-day computers, single particle models can without much effort be designed to meet specific properties of certain experimental systems. This is an important reason to why they are so popular and numerous. A classic example is the motility assay where biofilaments are pushed forward by molecular motors[22, 138]. Here, the polymers are described

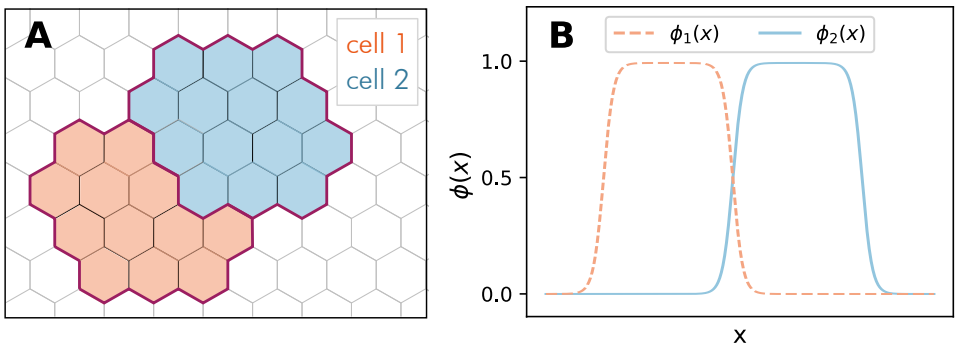


**Figure 2.2** *Illustration of Cellular Potts Models (CPMs) and phase field models.* (A) In CPMs, cells occupy several tiles on a lattice. Every lattice site belongs to one cell exclusively (different cells shown in different colours). (B) In phase-field models, the inside of cell $i$ is defined as the region where the corresponding field $\phi_i$ has a value larger than 0.5. The illustration is for a one-dimensional model after [139].

as connected active particles and simple phenomenological interaction rules allow to reproduce the experimental results qualitatively[24].

## 2.3 Cellular Potts Models (CPMs) and phase field models

One degree more detailed than single particle models are models that simulate extended particles of variable shape and with internal structure. Models of this kind are preliminarily used in cellular systems whose properties will be explained in more detail in chapter 5.

One class of such models are Cellular Potts Models (CPMs)[140–142]. CPMs are two-dimensional lattice models where individual cells are described as connected areas on the lattice. In spirit of the Potts Model any lattice-site can be occupied by only one cell, by numbering all cells in the system the state of a lattice-point can be identified with the number of the occupying cell (for illustration see Figure 2.2A). The dynamics are governed by a kinetic Monte-Carlo algorithm. The corresponding free energy contains terms that regulate cell size and circumference as well as cell-cell and cell-substrate interaction terms. Additionally spatially varying fields defined inside the cells can emulate internal mechanisms that determine the cells' behaviour as a basic notion of cell mechanics. We will use this model in chapter 6 to simulate an assembly of cells invading into a channel. A more detailed description of a CPM can be found there.

Phase-field models in contrast describe cells via spatially varying fields $\phi_i(\mathbf{r}, t)$. Every cell is represented by one field, see sketch in Fig. 2.2B. A Cahn-Hilliard type

free energy ensures that all fields assume the value 1 over a compact region that is small compared to the systems size and 0 elsewhere with a narrow transition region. Then by definition the inside of a cell $i$ is where the corresponding field $\phi_i(\mathbf{r}, t) > 0.5$, the outside where $\phi_i(\mathbf{r}, t) < 0.5$. The free energy additionally contains terms of the type $\phi_i(\mathbf{r}, t)\phi_j(\mathbf{r}, t)$ that create repulsive interaction and prevent overlap of fields. The dynamical equations for the $\phi_i(\mathbf{r}, t)$ usually ensure that cell-volume is conserved.

From another perspective, phase field models are a generalisation of the Cahn-Hilliard model and have originally been used to model multiphase substances like binary alloys[143], but were later on used to model cellular systems as well[144–147]. To simulate cellular processes inside the cell, it can be coupled to field theories like the ones described in section 2.1, for example to a polar vector field[93, 148, 149] or a nematic field[150].

# 3 Invasion of active nematics into a capillary

*This chapter was originally published with me as first author in [1] together with Romain Mueller, Erwin Frey, Julia Yeomans, and Amin Doostmohammadi. Contents from this source have been reproduced here, with permission from the Royal Society of Chemistry. For details of the license see Appendix 3.1.*

## 3.1 Motivation

Understanding the mechanisms by which living (active) systems such as cells and bacteria invade and navigate through their surroundings is of pivotal importance in many physiological and pathological processes. Depending on the physical and chemical properties of their microenvironment active matter can show distinct modes of invasion, from single cell migration to groups of cells moving as a collective. The latter has been identified as the primary mode of cancer cell invasion[84, 151]. Similarly collective migration is the prime mode of growth and invasion by bacterial biofilms[87–89].

Among physical environmental factors, geometrical constraints have a strong influence on the dynamics of collective migration in biological matter. Various physiological processes such as bacterial filtering rely on active matter living within pores, cavities, and constrictions[152]. *In vivo*, cancerous cells are known to preferentially move along pre-existing tracks of least resistance, such as myelinated axons or blood vessels, when invading into healthy tissue[80, 81]. Similarly, during biofilm formation interaction between the bacterial colony and the surface it grows on is of major importance[82, 83]. The relevance of the interaction between biological matter and confining geometries in many physiological processes has prompted extensive experiments. In particular, *in-vitro* experiments on epithelial cells[67–73], bacteria[23, 76], and mixtures of biofilaments and molecular motors[36, 77] have shown that confinement to channel-like geometries generically alters the flow of biological matter in a significant way. Striking examples are the crossover from chaotic flows of bacteria[23, 75] and microtubule/motor protein mixtures[37, 78] to polarised movement along the long channel axis and the emergence of shear flow in fibroblast cells[73] confined within rectangular geometries. Moreover, theoret-

ical and computational studies of active matter interacting with a periodic array of obstacles have shown a reduction in the effective diffusion coefficient of active particles with increasing density of obstacles[17] and modification of the active dispersion within periodic arrays in the presence of applied flows[65].

While recent research has been primarily focused on the crosstalk between the confinement and the activity of the particles in order to determine patterns of motion, a complete understanding of the patterns of collective invasion and spreading also requires a detailed investigation of growth dynamics. From the physical perspective, such interplay between activity, confinement, and growth can be accompanied by additional complexities arising from hydrodynamic interactions between growing active matter and the confinement, orientation dynamics of elongated active particles, and emergent collective phenomena such as active turbulence[31, 96, 120, 125, 153] and active topological defects[35, 118, 119, 154]. Due to this interconnection of complex physical processes, the mechanistic understanding of active matter invasion within geometrical constraints remains largely unexplored. Recent numerical analyses of a self-propelled particle model[155], neglecting orientational dynamics and hydrodynamic effects, have shown that the physics of growing active matter can explain some of the observed experimental phenomena[67], such as caterpillar motion of the advancing front and the enhancement of collective migration speed in thin capillaries, by assuming a coupling between the curvature of the front and the motility of the particles at the leading edge.

Here we use a generic model of active matter that accounts for hydrodynamics, orientational effects, and growth to investigate collective patterns of active matter invasion of capillaries. We identify three different regimes of invasion, each with distinct interface shapes, flow patterns, orientational ordering, and topological defect dynamics. In particular, we show that above a certain threshold in the strength of the active forces, highly dynamic deformations are formed at the interface between the invading active matter and the surrounding medium. At higher activities, we also find a second threshold beyond which blobs of active matter begin to detach from the growing active column to enhance the invasion of free space. We explain the first crossover in terms of intrinsic hydrodynamic instabilities of the bulk active matter accompanied by additional instabilities arising from the presence of the growing interface. The latter can be understood by the ability of active stresses to overcome the stabilising effect of the surface tension and pinching off the growing interface. Together, our study reveals several possible invasion patterns and collective dynamics when active matter invades a capillary constriction thus providing a framework for further experimental investigations.

## 3.2 Model definition and methods

We employ a two-phase model of active nematohydrodynamics[112] to explore the growth of an active layer into otherwise isotropic surroundings within a confined channel and use a hybrid lattice Boltzmann (LB) method to numerically solve the equations[156]. This choice was motivated by the generality of this class of continuum models which is due to the fact that only local conservation laws, a nematic interaction between the systems' constituents, and perpetual injection of energy at the smallest length-scale are assumed. Models of this kind reproduce a variety of non-equilibrium flows such as stable arrays of vortices or chaotic flows, together with diverse stationary and non-stationary patterns of nematic ordering and topological defects[117, 118, 120, 121, 125, 157–159]. On a phenomenological level, these are successful in modelling the collective dynamics in biological systems in cases such as microtubule/motor-protein mixtures[30, 118, 158], cellular monolayers[35, 160–162], or bacteria[163]. In addition to the bulk dynamics, the interaction with walls or obstacles of different shape can add further complexity. Theoretically, using the active nematohydrodynamics framework, a transition to spontaneous flows in channels has been predicted[164, 165], as well as more complex states with intricate interplay of defects and vortices, and a transition to active turbulence[123, 126, 166].

### 3.2.1 Governing equations

We consider a two-dimensional model of a two-phase system consisting of an isotropic fluid phase and an active nematic phase[112]. The orientational order in the nematic phase is characterised by the symmetric and traceless nematic tensor $Q_{\alpha\beta} = S\left(2n_\alpha n_\beta - \delta_{\alpha\beta}\right)$[167] with $S$ (magnitude of the nematic order) and $n_\alpha$ (director) indicating the magnitude and the direction of the nematic order, respectively. The relative density of the nematic phase is measured by a scalar phase field $\phi$ which is 0 in the purely isotropic and 1 in the purely nematic phase.

The free energy density of the system is given by (using the Einstein summation convention):

$$f = \frac{1}{2}D\phi^2(1-\phi)^2 + \frac{1}{2}C_{LQ}\left(\phi - \frac{1}{2}Q_{\alpha\beta}Q_{\alpha\beta}\right)^2 + \frac{1}{2}K_\phi\partial_\gamma\phi\partial_\gamma\phi + \frac{1}{2}K_Q\partial_\gamma Q_{\alpha\beta}\partial_\gamma Q_{\alpha\beta}, \quad (3.1)$$

where $D$, $C_{LQ}$, $K_\phi$, and $K_Q$ are positive material constants. Since $Q_{\alpha\beta}Q_{\alpha\beta} = 2S^2$, the second term ensures a tight coupling between the magnitude of the nematic order $S$, and the phase field $\phi$. Together with the first term, which corresponds to a

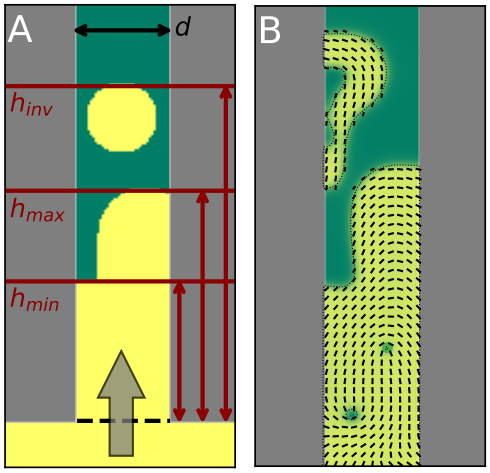


**Figure 3.1** *Simulation setup* (A) Schematic drawing of simulation setup. The active phase (yellow) invades from the broader reservoir (region below black dashed line) where it can grow into the narrower capillary (width $d$) that is initially filled with isotropic liquid (green). The broad gray arrow illustrates the invasion direction. Different heights are marked for later discussion of observables: $h_{\mathrm{max}}$, the highest point of the active phase which is connected to the reservoir, $h_{\mathrm{inv}}$, the highest point that any patch of active phase reaches, and $h_{\mathrm{min}}$, the highest point where the capillary is filled with active fluid to the full width. (B) A representative simulation snapshot to illustrate the dynamics. Black bars mark the director field; the two green speckles inside the nematic phase are cores of +1/2 topological defects.

Cahn-Hilliard free energy[38, 168], this leads to well-defined interfaces between a nematic ($S = 1, \phi = 1$) and an isotropic ($S = 0, \phi = 0$) phase (Fig. 3.1). The third and fourth terms are elastic energies. The first, third, and fourth terms contribute to the surface energy and the fourth term also penalises bulk deformations in $Q_{\alpha\beta}$. The free energy then reads

$$\mathcal{F} = \int \mathrm{d}^2\mathbf{r}\, f. \tag{3.2}$$

The order parameters evolve according to the following equations:

$$\partial_t \phi + \partial_\beta \left(\phi u_\beta\right) = \Gamma_\phi \Delta\mu, \tag{3.3}$$

$$\left(\partial_t + u_\kappa \partial_\kappa\right) Q_{\alpha\beta} = -\xi \Sigma_{\alpha\beta\kappa\lambda} E_{\kappa\lambda} - T_{\alpha\beta\kappa\lambda}\Omega_{\kappa\lambda} + \Gamma_Q H_{\alpha\beta}, \tag{3.4}$$

with

$$\mu = \frac{\partial f}{\partial \phi} - \partial_\gamma \frac{\partial f}{\partial \left(\partial_\gamma \phi\right)}, \tag{3.5}$$

$$H_{\alpha\beta} = \left(\delta_{\alpha\beta}\delta_{\kappa\lambda} - \delta_{\alpha\kappa}\delta_{\beta\lambda} - \delta_{\alpha\lambda}\delta_{\beta\kappa}\right) \left\{\frac{\partial f}{\partial Q_{\kappa\lambda}} - \partial_\gamma\left(\frac{\partial f}{\partial \left(\partial_\gamma Q_{\kappa\lambda}\right)}\right)\right\}, \tag{3.6}$$

$$E_{\alpha\beta} = \frac{1}{2}\left(\partial_\beta u_\alpha + \partial_\alpha u_\beta\right), \quad \Omega_{\alpha\beta} = \frac{1}{2}\left(\partial_\beta u_\alpha - \partial_\alpha u_\beta\right), \tag{3.7}$$

$$\Sigma_{\alpha\beta\kappa\lambda} = Q_{\alpha\beta}Q_{\kappa\lambda} - \delta_{\alpha\kappa}\left(Q_{\lambda\beta} + \delta_{\lambda\beta}\right) - \left(Q_{\alpha\lambda} + \delta_{\alpha\lambda}\right)\delta_{\kappa\beta} + \delta_{\alpha\beta}\left(Q_{\kappa\lambda} + \delta_{\kappa\lambda}\right), \tag{3.8}$$

$$T_{\alpha\beta\kappa\lambda} = Q_{\alpha\kappa}\delta_{\beta\lambda} - \delta_{\alpha\kappa}Q_{\beta\lambda}. \tag{3.9}$$

The l.h.s. of Eqs. (3.3) and (3.4) are convective derivatives with the underlying velocity field $u_\alpha$. Advection and diffusion drive the dynamics in $\phi$; $\Gamma_\phi$ is the corresponding diffusion constant. $\Gamma_Q$ is a rotational diffusion constant which, together with the molecular field $H_{\alpha\beta}$, controls diffusive relaxation in $Q_{\alpha\beta}$. In addition, the interplay of flow $u_\alpha$ and order $Q_{\alpha\beta}$ is less trivial. The first and second terms on the r.h.s. of the Eq. (3.4) form the co-rotational derivative which accounts for the response of the orientation field to the extensional ($E_{\alpha\beta}$) and rotational ($\Omega_{\alpha\beta}$) components of the velocity gradients respectively. $\xi$ is the tumbling parameter which determines the relative influence of the rate of strain on the director orientation. It depends on the geometry of the active particles, for prolate ellipsoids $\xi > 0$, while for oblate ellipsoids $\xi < 0$, and for spherical particles $\xi = 0$[169].

The velocity field $u_\alpha$ obeys the Navier-Stokes equations:

$$\partial_t \rho + \partial_\beta\left(\rho u_\beta\right) = 0, \tag{3.10}$$

$$\rho\left(\partial_t + u_\beta\partial_\beta\right)u_\alpha = \partial_\beta \Pi_{\alpha\beta}, \tag{3.11}$$

where $\rho$ is the density of the fluid and $\Pi_{\alpha\beta}$ is the stress tensor comprising viscous stress, pressure contribution, elastic stresses, and the active stress:

$$\Pi^{\text{visc}}_{\alpha\beta} = 2\rho\eta E_{\alpha\beta}, \tag{3.12}$$

$$\Pi^{p}_{\alpha\beta} = -\frac{\rho}{3}\delta_{\alpha\beta}, \tag{3.13}$$

$$\Pi^{\text{el},1}_{\alpha\beta} = (f - \mu\phi)\,\delta_{\alpha\beta} - \frac{\partial f}{\partial\left(\partial_\beta\phi\right)}\partial_\alpha\phi - \frac{\partial f}{\partial\left(\partial_\beta Q_{\kappa\lambda}\right)}\partial_\alpha Q_{\kappa\lambda}, \tag{3.14}$$

$$\Pi^{\text{el},2}_{\alpha\beta} = \left(\xi\Sigma_{\alpha\beta\kappa\lambda} + T_{\alpha\beta\kappa\lambda}\right) H_{\kappa\lambda}, \tag{3.15}$$

$$\Pi^{\text{act}}_{\alpha\beta} = -\zeta\phi Q_{\alpha\beta}. \tag{3.16}$$

Here, $\eta$ is the viscosity, and the elastic stresses $\Pi^{\text{el},i}_{\alpha\beta}$ describe feedback from variations in the order parameters on the fluid flow[112]. The definition of the active stress $\Pi^{\text{act}}_{\alpha\beta}$ is such that any gradient in $Q_{\alpha\beta}$ generates a flow field and drives the system at small length-scales, with strength determined by the magnitude of the activity $\zeta$. A positive (negative) $\zeta$ corresponds to an extensile (contractile) material. The dipole flow-fields generated with this ansatz correspond to those of microswimmers - "pushers" generate extensile stresses, "pullers" contractile stresses[170]. The active stress continuously drives the system out of thermodynamic equilibrium. It will be of major importance in the following discussions.

### 3.2.2 Simulation setup

In Fig. 3.1, we show the geometry for which we will solve the equations. This simulation setup corresponds to the experimental configurations for cell monolayers in references [67–71]. It consists of a wider reservoir that feeds a narrower capillary. At $t = 0$, the active phase is restricted to the large reservoir.

In order to generate new active material in the reservoir, we locally increase $\phi$ to values higher than 1.0 at random positions. For every point in the active phase in the reservoir, a *growth event* takes place with probability $r\phi(1 - \phi/\phi_c)$. This means that for a given time $\tau_g$, a source term $\alpha\phi$ is added to the r.h.s. of Eq. (3.3) in a circle of radius $r_g$ around this site. Diffusion and convection then lead to a spreading of the active phase, causing it to rise into the thinner capillary. This local implementation leads to additional flow in the reservoir as growth events generate dipole-like flow fields and a growth pressure through the isotropic part of $\Pi^{\text{el},1}$. The logistic-growth-like saturation in the probability $r\phi(1 - \phi/\phi_c)$ prevents unbounded growth of $\phi$. We find that the details of this implementation or even the geometry

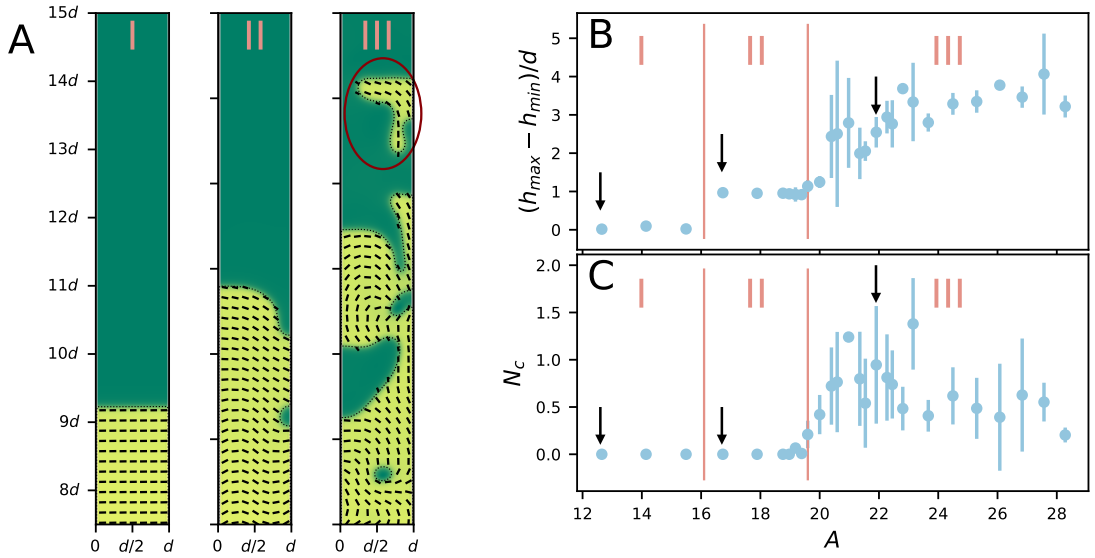


**Figure 3.2** *Phenomenological regimes for varying activity number.* (A) Snapshots from simulations showing typical configurations of the different regimes. From left to right: Regime I with flat interface, regime II with a deformed interface, and regime III where clusters (red circle) start to detach from the main active phase. Corresponding Movies are flows0020.mp4, flows0035.mp4, and flows0060.mp4, respectively, see section 1.1 in the appendix. (B) Quantitatively, the crossover from regime I to II is characterised by a sudden increase in $(h_{\max} - h_{\min})/d$ from 0 to 1 (see Fig. 1 for the definition of $h_{\max}$ and $h_{\min}$). By contrast, within regimes I and II, this quantity is nearly constant. In regime III it increases with activity. (C) While there is only one single coherent patch of active material in regimes I and II, the defining property of the crossover from II to III is the appearance of additional clusters. $N_c$ denotes the number of clusters in addition to the bulk active phase. Black arrows in B and C mark values for which snapshots in A were taken. Errorbars depict 1.96 SEM (standard error of the mean). To estimate the SEM, simulations with different initial noise were performed for identical parameter configurations.

of a reservoir are not important for the qualitative dynamics in the capillary (see section 3.3.3).

In this study, we use the following parameters: $D = 0.08$, $C_{LQ} = 0.15$, $K_Q = 0.02$, $K_\phi = 0.08$, $\Gamma_\phi = 0.2$, $\Gamma_Q = 0.4$, $\xi = 0.7$, $\eta = 1/6$, $r = 0.001$, $\tau_g = 10000$, $r_g = 5$, $\alpha = 0.01$, $\phi_c = 1.2$, unless otherwise noted. We vary $\zeta$ from 0.0020 to 0.0100 to investigate how invasion depends on the strength of the active driving. The free energy coefficients are chosen such that there is a well-defined interface between the active and the passive phase. $\xi = 0.7$ leads to alignment of the director to an external flow in a passive nematic. Parameter fitting of the continuum equations to physical active systems remains a topic of research; therefore, we consider a generic parameter set that has been shown to reproduce the flow vortex-lattice generated

by a dense assembly of endothelial cells[171, 172], and the flow fields of dividing Madin-Darby Canine Kidney cells[162]. Independent samples for parameter sets are obtained by varying the initial condition randomly. Boundaries are no-slip with respect to the fluid and von-Neumann for $\phi$ and $Q_{\alpha\beta}$, meaning that there is no preferred anchoring of the director in the absence of activity. Variation of the boundary conditions can potentially lead to the emergence of additional exotic phases of invasion, but their systematic study lies beyond the scope of this work. For the reservoir, we have periodic boundary conditions in the direction perpendicular to the capillary axis.

In the following, we characterise the strength of the activity by the dimensionless activity number $A = d/(\sqrt{K_Q/\zeta}) = d/\Lambda_\zeta$. The activity-induced length-scale $\Lambda_\zeta = \sqrt{K_Q/\zeta}$ emerges from the competition between the activity driving the dynamics and the elastic resistance against deformations in the director field[120, 173, 174], while the capillary width $d$ imposes an upper limit for hydrodynamic interactions across the capillary. The activity number $A$ relates these two length-scales[123, 126].

## 3.3 Results

### 3.3.1 Distinct invasion regimes

For a first characterisation of the invasion behaviour of active matter into a capillary, we will focus on how the phenomenological changes in the structure and the dynamics of the interface between the active phase and the isotropic fluid depend on the dimensionless activity $A$. Surprisingly, we observe that this can be categorised into three different regimes separated by two well-defined crossovers under variations of this single quantity alone.

Figure 3.2A shows characteristic snapshots for the three different regimes. For small activities, below a certain threshold ($A \sim 16$), the system is characterised by a flat interface between the isotropic and active phase that advances steadily from the reservoir. We denote this as regime I. Due to the extensile activity of the particles (i.e. $\zeta > 0$), the active stresses generate a preferential orientation of the director parallel to the interface, an effect called 'active anchoring'[112]. For low $A$, the director field remains homogeneous throughout the nematic phase and the hydrodynamic instabilities are suppressed.

When approaching the crossover from regime I to regime II by increasing the activity, bend deformations of the director field arise in the bulk without influencing the shape of the interface (see Movies flows0020.mp4 and flows0030.mp4). The defining property of regime II is the crossover to a state where the interface is deformed to an S-shape while keeping a 90° contact angles at both walls. As

discussed in more detail in the next section, within this regime the deformed interface initially advances with the leading point on one side of the capillary wall (see Movie flows0035.mp4). With a further increase in activity, we observe a periodic switching of the S-shape of the interface from one side of the capillary to the other side as the system approaches the third invasion regime.

In both regimes, I and II, the active phase remains as one single coherent phase which is connected to the reservoir. This changes with the crossover to regime III at $A \sim 20$, where a higher activity leads to the dispatching of small clusters of active material from the main body of the active phase, that protrude deeper into the capillary. In addition, the active interface and the director field are strongly deformed and highly dynamic. Defects are regularly created at the boundary and move throughout the bulk of the active phase (see Movie flows0060.mp4).

### 3.3.2 Detailed characterisation of invasion regimes and crossovers

To understand the connection between the different interface dynamics and the overall invasion process, we further characterise the defining features of the three different regimes. Quantitatively, the crossovers between the regimes can be read off from two observables: (i) $(h_{\max} - h_{\min})/d$, which characterises deformations of the isotropic-active interface in the capillary (see Fig. 3.1A for definition of $h_{\max}$ and $h_{\min}$), and (ii) $N_c$ which is the number of clusters of the active phase that are in the system in addition to the main body of the active phase connected to the reservoir. As the activity number is increased, the crossover from regime I to regime II is reflected by a jump in the mean value of $h_{\max} - h_{\min}$ from 0 to the width $d$ of the capillary, or equivalently a jump of $(h_{\max} - h_{\min})/d$ from 0 to 1 (Fig. 3.2B), which mirrors the S-shape of the interface in regime II. Within the parameter range studied here, we did not observe any variation in the positioning of the crossover from regime I to regime II under variation of $D$. The second crossover, from regime II to regime III, is also marked by a further jump in $(h_{\max} - h_{\min})/d$, but is even more evident in $N_c$ which becomes finite (Fig. 3.2C), reflecting the emergence of additional smaller clusters that detach from the main active phase. It is noteworthy that a similar quantitative behaviour is observed when varying the width of the channel (see Fig. 3.7 in section 3.3.4), indicating that the activity number is the relevant dimensionless parameter in this setup.

#### 3.3.2.1 Properties of regime II

The crossover from regime I to II is also accompanied by sharp changes in the flow and director fields in the capillary. This not only sheds light on the underlying mechanism, but also has consequences for the overall speed of invasion as we will

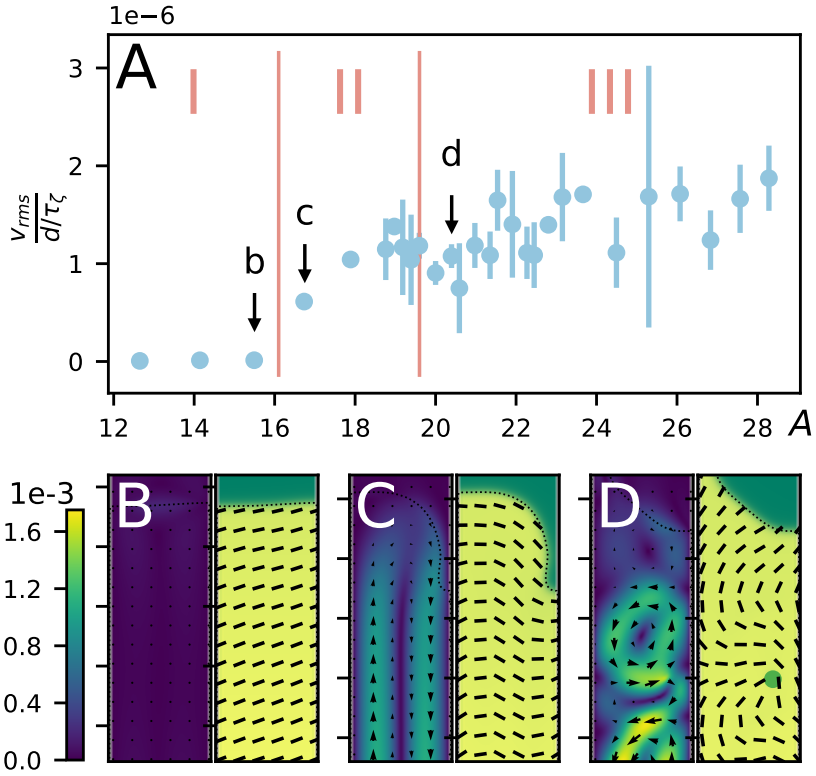


**Figure 3.3** *Comparison of flows across regimes.* (A) Root mean-squared velocity in units of $d$ over the active time scale $\tau_\zeta = \eta/\zeta$[168] plotted against $A$ . Crossover from regime I to II coincides with the appearance of finite flows. Strength of flows increases inside regimes II and III with a small plateau at the crossover from regime II to regime III. Lower case letters indicate the values at which examples in (B-D) were taken. (B-D) Characteristic velocity and orientation fields near the interface. (B) For $A = 15.5$, the system is in regime I, the interface is flat with no flows near it. (C) At $A = 16.7$, in regime II, the interface is bent and the characteristic flow that turns at the interface is visible. (D) In regime III ($A = 20.4$), the interface can take various forms, +1/2-defects (green dot) appear in the bulk and the flow becomes highly dynamical and complex. Movies corresponding to panels B-D are flows0030.mp4, flows0035.mp4, and flows0052.mp4, respectively, see appendix section 1.1.

see later (section 3.3.5). Figures 3.3A,B show that below the first crossover, there are no flows in the capillary ($v_{\mathrm{rms}} = 0$). For higher activities, with a non-zero $(h_{\max} - h_{\min})/d$, finite flows are generated (Figs. 3.3A,C). This is reminiscent of the well-established spontaneous flow transitions in confined active matter[156, 164], which arise due to the formation of hydrodynamic instabilities in active nematics above a certain threshold of activity. While in those cases the active force alone is

responsible for the transition, in the present situation the growth dynamics in the reservoir induces long-range effects which influence the position of the crossover (for a system without reservoir, see section 3.3.3). The advection of active material along with these flows causes the characteristic S-shape of the interface in this regime. Interestingly, $v_{\mathrm{rms}}$ is increasing with higher activity numbers within regime II while $(h_{\max} - h_{\min})/d \sim 1$ throughout.

Moreover, because of the impact of the extensile activity that keeps the director aligned with the interface, the increasing bend deformation looks similar to a backwards pointing +1/2-topological defect at the less advanced side of the interface (Fig. 3.3C; right panel). Corresponding to the characteristic self-motility of +1/2-topological defects[35, 123, 175], the interface on this side continues to move backwards relative to the mean interface-position stretching out the interface until the defect detaches from the interface and moves into the active phase. Concomitantly with this defect absorption into the nematic, the interface re-attaches to the wall at a higher position. Repeatedly, this leads to a periodic shape-change in the interface (see Fig. 3.4A and the Movie flows0035.mp4).

As the activity is increased further, the initial spontaneous transition to flows is followed by the generation of counter-rotating vortices along the capillary. As the active phase grows and advances through the capillary, a lattice of vortices is formed behind the interface, reminiscent of vortex-lattices in a non-growing confined active matter[126, 176], which appear when the activity-induced vorticity length scale becomes comparable to the capillary width. Interestingly, however, in this growing active matter, the orientation of the vortex closest to the interface also determines the parity of the interface. As a consequence, a change in the orientation of the most forward vortex leads to a switching at the interface, with the S-shape of the progressive front flipping from one side of the channel to the other with respect to the capillary axis (see Fig. 3.4B and the Movie flows0046.mp4).

Within regime II, the rms-velocity $v_{\mathrm{rms}}$ grows approximately linearly with the activity number $A$ and the flow field remains structured until transitioning to active turbulence in regime III (Fig. 3.3D).

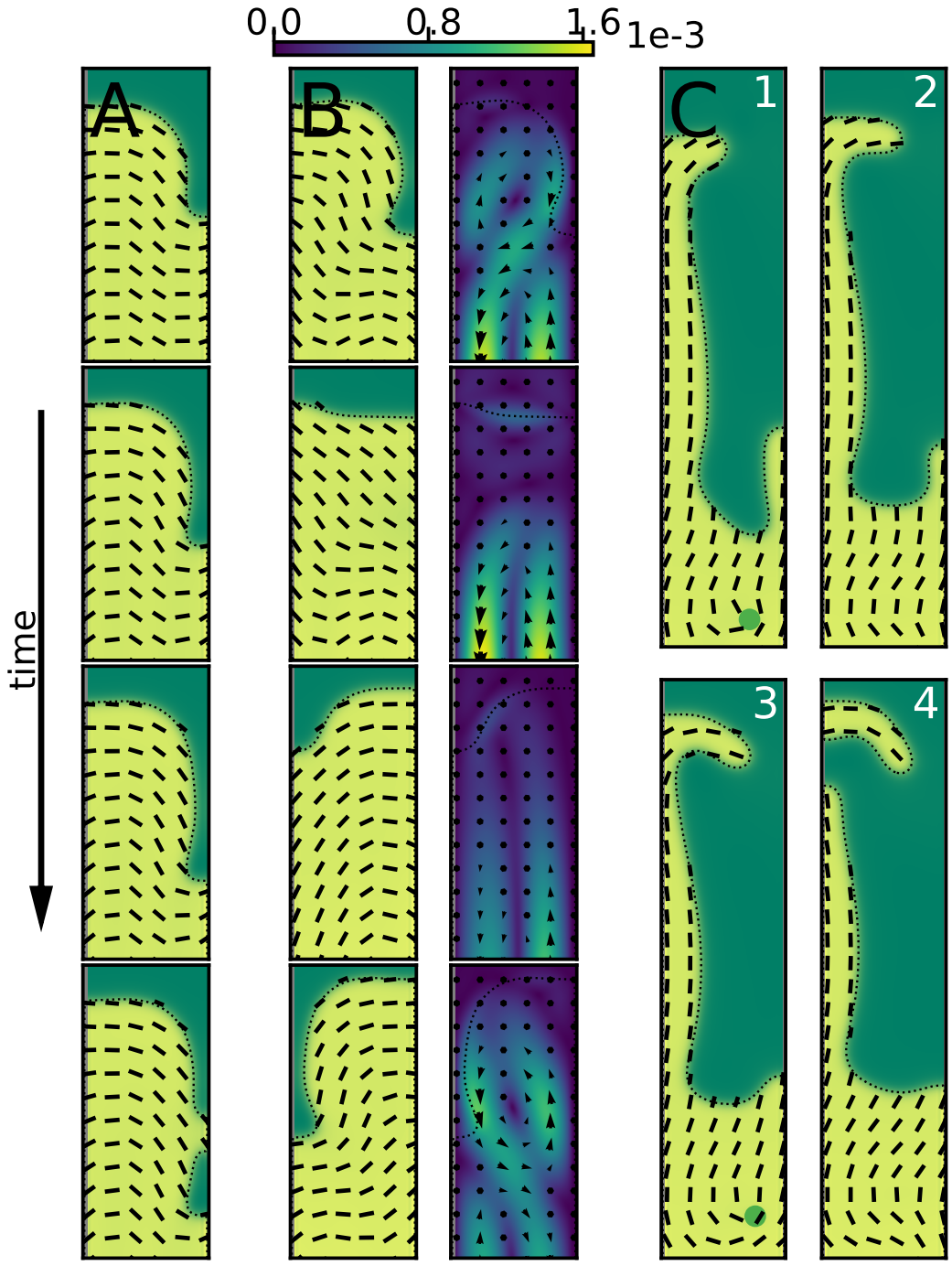


**Figure 3.4** *Interface dynamics in regimes II and III.*

**Figure 3.4** ***(ctd. from previous page)*** (A) Characteristic periodic motion in regime II ($A$ = 17.9). The +1/2-defect like bend-deformation on the right wall moves backwards relative to the interface until it is pinched off and dissolved in the nematic bulk. Simultaneously the interface relaxes back to a less stretched state and the cycle begins anew. (B) Switching in the S-shape for higher activities in regime II ($A$ = 19.2). When approaching the second crossover, vortices emerge in the capillary (panels on the right). When the most forward vortex changes its rotation direction, the director follows and bend deformations as well as interface shape adapt accordingly. (C) Time series of a cluster-formation event in regime III ($A$ = 20.4). The nematic layer at the wall becomes unstable until finally a cluster detaches from the main active phase. In each of (A-C) the simulation time between all sequential snapshots is equal and is measured in units of the active time scale $\tau_\zeta = \eta/\zeta$[113], A: $\delta t = 480\tau_\zeta$, B: $\delta t = 2760\tau_\zeta$, C: $\delta t = 1248\tau_\zeta$. Movies corresponding to panels B and C are flows0046.mp4 and flows0052.mp4, respectively, see section 1.1 of the appendix.

#### 3.3.2.2 Properties of regime III

While the crossover to regime II was solely controlled by the hydrodynamic instability to spontaneous flow formation within the bulk of the active matter in the capillary, the crossover from regime II to III, where active clusters appear, is strongly influenced by the competition between activity and surface tension at the interface. This interfacial effect can be clearly seen in a close-up view of the interface at the onset of cluster detachment (Fig. 3.4C): At a sufficiently high activity number relatively long and thin layers of active matter with an approximately uniform director field are formed at the sides of the capillary wall. As the simulation time goes by, a small deformation at the tip of the layer develops and grows until it breaks away from the active layer, forming a detached cluster (see Movie flows0052.mp4). The formation of clusters means an increase in total interface length which is increasingly unfavourable for higher surface tension and thus requires higher active stresses to be generated. Therefore, the breakup of the thin layer can be understood as the destabilising effect of the activity that leads to the interface deformation dominating over the stabilising effect of the surface tension, working to keep the interface straight. However, especially in this complex setup, it is not possible to decide to what degree this effect is purely interfacial and whether dynamics in the bulk are important.

Yet, varying the surface tension $\sigma \propto \sqrt{D}$ (see section 4.2.1 for derivation) by varying the binary bulk coefficient $D$ in the free energy density (3.1) influences the second crossover. As expected, we find that the value of $A$ where clusters appear for the first time, i.e. where $N_c$ changes to finite values, is pushed to higher activity numbers $A$ with increasing $\sigma$ (see Fig. 3.5A).

The simultaneous appearance of +1/2 topological defects in the nematic phase (see Fig. 3.5 B) hints that changes in the bulk dynamics are also involved in the

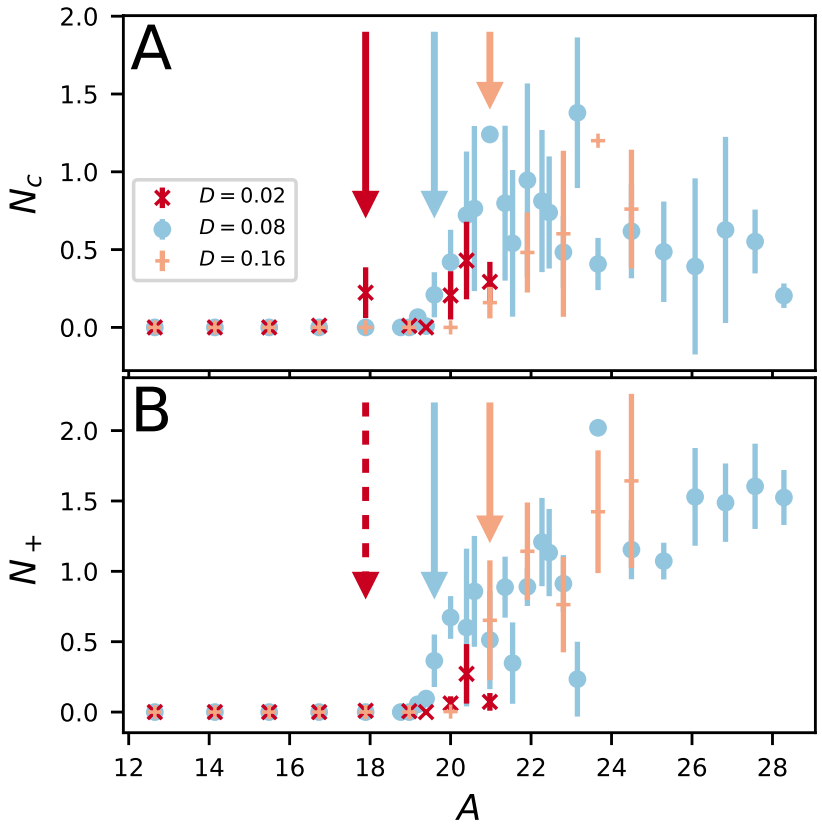


**Figure 3.5** *Transition between regimes II and III for different values of D, corresponding to varying surface tensions* $\sigma \propto \sqrt{D}$. (A) Number of clusters $N_c$. For higher $\sigma$, the first appearance of clusters moves to higher activity numbers $A$ (marked by the coloured arrows). (B) Number of $+1/2$ topological defects in the system. Apart from $D = 0.02$, appearance of clusters and defects coincide.

crossover as flow dynamics become more reminiscent of turbulent dynamics and higher active stresses are generated. Interestingly, directly after the crossover the number of additional clusters peaks. With a further increase in $A$ the clusters are still present, however the number of clusters goes down. A close look at the interface reveals that at very high activities the active material forms extremely long and thin layers on the capillary walls and the detached clusters quickly reattach to the main body of the active nematic, leading to a smaller number of clusters on average.

### 3.3.3 Role of reservoir and growth

In this section we examine the importance of the cell division and the presence of a reservoir on the dynamics. Figure 3.6 shows simulation results for two systems that

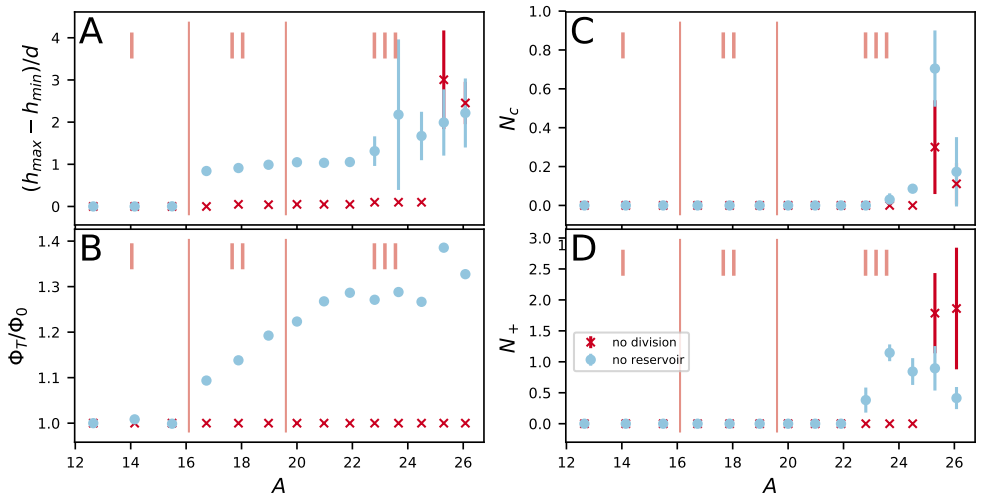


**Figure 3.6** *Comparison of different modifications of the setup.* (A) $(h_{\max} - h_{\min})/d$ as a function of $A$. The crossover from regime I to regime II takes place at the same values as in the unmodified setup for a system without reservoir but with growth (blue circles), but is absent for a system lacking growth (red crosses). Vertical lines mark the crossover points in the unmodified setup. (B) Total amount of active material in the system at the end of the simulation relative to the starting value. In the non-growing system, the amount of active material is trivially constant over time. The system without reservoir shows the same qualitative dynamics as the unmodified setup. Data in this figure has been taken from one sample per value for $A$ only. (C) The number of clusters $N_c$ as a function of $A$. The crossover from regime II to regime III takes place at higher values as in the unmodified setup for a system with reservoir but without growth, which also explains the longer linear range in subfigure B. Clusters are also present for a system lacking growth, but it takes longer for them to appear. (D) The number of $+1/2$ defects $N_+$ as a function of $A$. The appearance of topological defects, for both setups, coincides with the appearance of additional clusters (compare subfigure C).

differ from the one considered before, by the absence of a wider reservoir, and by the absence of cell division, respectively. We see that growth is an essential factor to create the phenomena reported before as in the absence of growth the behaviour is qualitatively different. If the reservoir is absent, meaning that there is only a capillary of uniform width where growth takes place in the lower region, we in contrast observe the first crossover at the same values for the activity $A$ (Fig. 3.6A), together with the same change in the invasion speed (Fig. 3.6B). The second crossover is however significantly shifted to higher values of $A$ (see Fig. 3.6C,D), indicating that the reservoir has long-range effects on the dynamics in the capillary. These, however, do not change the qualitative picture.

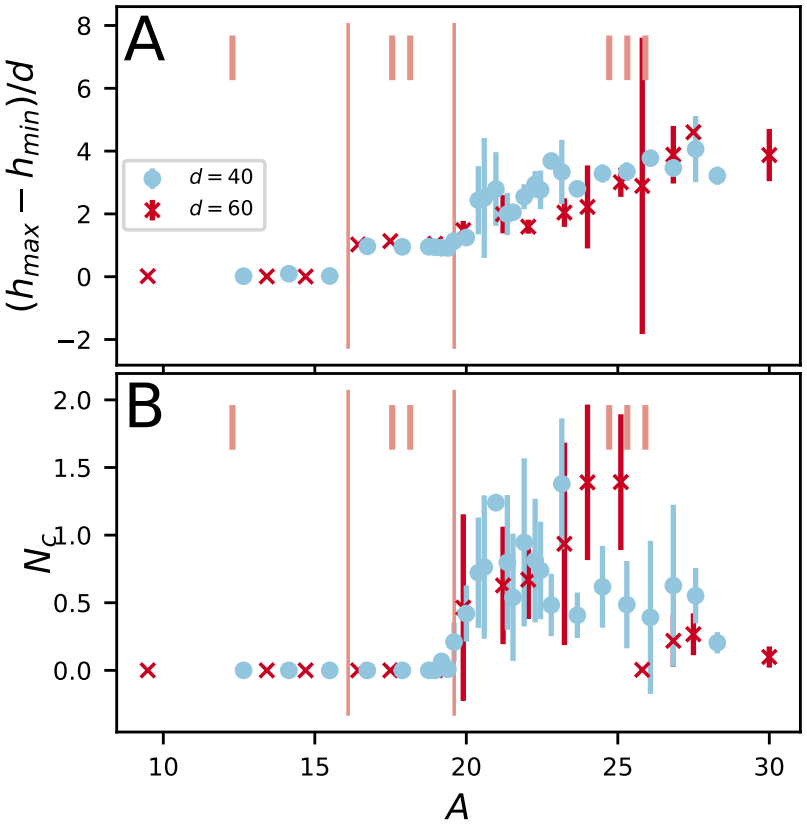


**Figure 3.7** *Universality for different channel widths.* $(h_{\max} - h_{\min})/d$ (panel A) and $N_c$ (panel B) against $A$. Both crossovers happen at the same values for both channel widths.

### 3.3.4 Universality for different channel widths

The activity number $A$ characterises the ratio of the channel width $d$ to the intrinsic length scale of the active phase. In Figure 3.7 the observables $(h_{\max} - h_{\min})/d$ and $N_c$ are plotted against $A$ for varying channel width $d$. Both crossovers happen at the same values for $A$, independent of $d$. In addition, both observables are of the same order of magnitude and within regime II $(h_{\max} - h_{\min})/d \sim 1$. These results indicate that the activity number is the relevant dimensionless parameter in this setup and that $(h_{\max} - h_{\min})/d$ is a meaningful observable.

### 3.3.5 Invasion capability

In the context of our original research question we now investigate the influence of the different regimes on the capability of the active system to claim new territories. To this end, we show in Fig. 3.8A the total amount of active material in the capillary at the end of the simulation (9.5 $10^6$ simulation steps) $\Phi_T := \int \phi(\mathbf{r}, T)\ \mathrm{d}^2\mathbf{r}/d^2$,

which we denote as the invasion index. In the absence of flows (regime I, when the process is purely diffusive), the invasion index $\Phi_T$ is almost independent of $A$ and it is significantly lower than in regimes II and III, where activity-induced flows enhance the advective transport of active material from the reservoir to the capillary. After the crossover from regime I to II, $\Phi_T$ follows a linear dependence on $A$ similar to the linear increase of $v_{rms}$ in this region. The crossover from regime II to III does not alter this quantity in a qualitative way, i.e. the additional clusters have no influence on the total amount of active material that invades the capillary. However, they can be shown to invade about 0.5 to 1.0 capillary widths deeper into the capillary than the tip of the coherent active phase connected to the reservoir. This is best illustrated by plotting the relative difference of the maximum invasion height $h_{\text{inv}}$ (see Fig. 3.1A) and the maximum height of the interface $h_{\text{max}}$: $(h_{\text{inv}} - h_{\text{max}})/d$ (Fig. 3.8B). Together, these results indicate that the flows in the capillary and the interfacial dynamics control the rate at which active material enters the capillary and thus determine the invasion speed.

## 3.4 Conclusions

In this work, we have presented a two-phase computational framework for studying the growth of active matter within an isotropic fluid medium. Our approach accounts for hydrodynamic effects and the orientational dynamics of active particles, and is able to reproduce emergent active phenomena including spontaneous flow generation and active turbulence. Motivated by the prevalence of active matter growing within confined spaces and constrictions, we investigated the dynamics in capillaries of different sizes, focusing on the combined effects of growth and the active stresses that are continuously exerted by active particles on their surroundings.

We find three distinct invasion patterns as the activity is varied: (i) at small activities invasion is completely controlled by the growth dynamics and the interface between the active phase and the surroundings remains stable with no, or slight, deformations. (ii) Increasing activity beyond a given threshold results in spontaneous flow generation which significantly enhances the invasion within the capillary and is accompanied by deformations of the interface. (iii) At yet higher strengths of activity, a second crossover appears, where active clusters begin to detach from the main body of the invading active phase, further enhancing the invasion of the surrounding space.

Our analysis shows that the crossovers between the various invasion regimes are controlled by different mechanisms. The crossover between regimes I and II is governed by the well-established spontaneous flow formation in confined active matter[164, 165], which is due to a hydrodynamic instability of the active nematic. We show that the onset of flow within the bulk is accompanied by the deformation

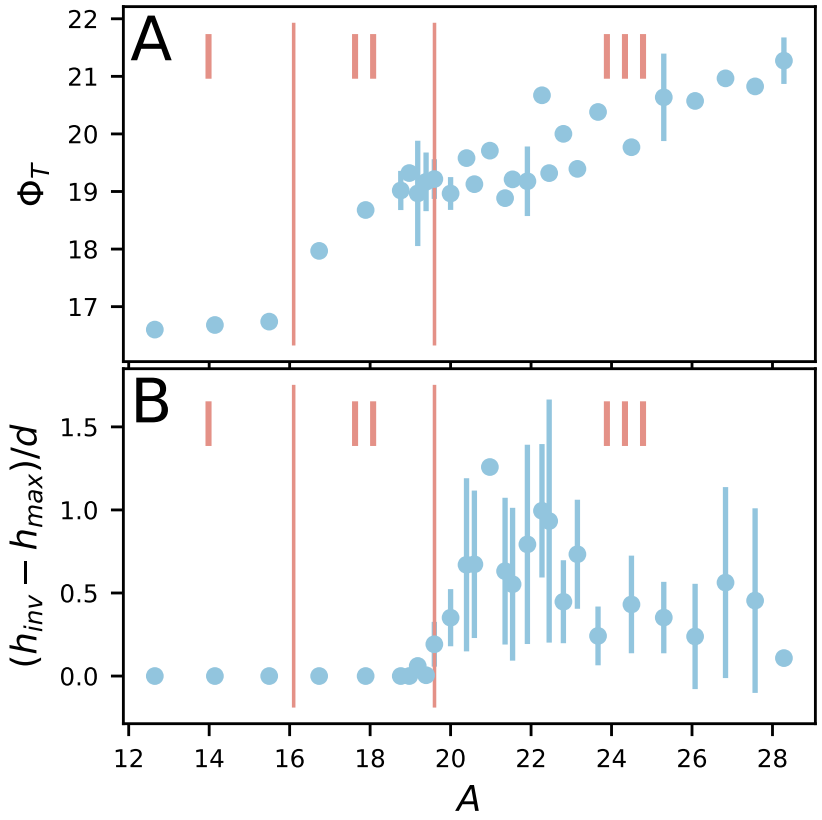


**Figure 3.8** *Propensity of the system to invade the capillary.* (A) Invasion index $\Phi_T := \int \phi(\mathbf{r}, T)\ \mathrm{d}^2\mathbf{r}/d^2$ defined as the amount of active material inside the capillary after 9.5 $10^6$ simulation steps plotted versus activity number $A$. In regime I, the invasion shows little dependence on $A$ until the appearance of flows at the crossover from regime I to II leads to a sharp increase. (B) Relative difference of the maximum invasion height and the maximum height of the interface $(h_{\mathrm{inv}} - h_{\mathrm{max}})/d$ against $A$. In regimes I and II, this difference is trivially zero. In regime III it shows an increase of up to one capillary-width meaning the clusters protrude significantly deeper into the capillary than the main body of the growing active matter.

of the interface and can even result in a periodic switching of the active protrusions from one side of the capillary to the other, as flow vortices start to form behind the advancing front. When activity becomes stronger, turbulent flows and defects are observed in the bulk of the active material and, dependent on its surface tension, the system also becomes able to rip apart the active-to-passive interface marking the third invasion regime.

Our results thus highlight the significant differences in invasion patterns when the activity of growing matter is accounted for. From a biological perspective, this could be linked to the invasive behaviour of biological matter such as growing

colonies of cells or bacteria. It suggests that qualitative changes in the spread of these organisms into confined spaces can be caused by changes in the availability and conversion rate of chemical energy into mechanical stresses. One could conjecture that more invasive cell lines or bacterial strands could regulate their invasion of pores or cavities by tuning their strength of motion. For example, inducing the formation of additional clusters might be beneficial for cell-lines that aim at aggressive invasion of surrounding tissue while, for bacteria, it might be beneficial to remain coherent in order to profit from the benefits of cooperative behaviour.

Considering possible experimental realisations, our model predictions apply to active growing systems, where hydrodynamic interactions and nematic orientational order play an important role. Such nematic ordering has been reported in various biological systems including bacterial colonies[163, 177], cultures of amoeboid cells[178], fibroblast cells[72, 161], human bronchial cells[179], neural progenitor stem cells[180], and Madin-Darby Kanine Kidney (MDCK) epithelial monolayers[35, 181]. Investigating the degree to which experiment and theory can be matched by the adaptation of parameters and boundary conditions in the model or the reasons for deviations is a powerful way of unraveling the role of mechanics in determining the behaviour of such active biological matter. It would also be interesting to compare to models that resolve individual particles such as models of self-propelled particles[155], phase field approaches[93, 182, 183], or cellular Potts models[184]. In contrast to these, our model by construction cannot resolve phenomena or implement mechanisms that act on the single particle-level, for example dynamics of cell size or shape, but due to its generality could contribute to a deeper understanding of the generic fundamental mechanisms that underlie the invasion of microscopic biological systems.

Finally, several improvements can be envisaged for the current model. In the context of growing tissues, studies have highlighted the importance of leader cells at the progression front[185, 186]. Within particle-based models such an effect is shown to be captured by introducing a curvature-dependent motility for the cells at the interface[155, 187]. Within our proposed framework, a similar effect could be modelled by introducing a curvature dependence to the activity coefficient. In addition, the natural environment of active material is often more complicated than the isotropic fluid considered here and active invasion happens through viscoelastic media. For example, cells invade the interconnected networks of collagen matrices and bacteria secrete their own extracellular matrices. The continuum framework presented here could be extended to include viscoelasticity by introducing additional order parameters representing polymer conformation.

# 4 Films and droplets: active matter on a wall

## 4.1 Introduction

To gain a better understanding of the interplay of active matter and geometry, it can be helpful to look at simpler configurations. A well-studied setup in the context of two-phase systems is the wetting problem: a small amount of liquid rests on a flat solid surface and is otherwise immersed into the second phase. A typical example is a drop of water or mercury on a table exposed to air. As this is in thermal equilibrium, all properties of a system are determined by the free energy. In the case of the droplet the relevant quantities are the surface tensions of the three different interfaces - the interface between the two phases and the two interfaces between each of the phases and the solid wall. The classical observable is the *contact angle*, the angle the interface between the two phases forms with the solid surface. This angle is totally determined by the surface tensions (*Young's law*)[188]. For certain conditions, called *perfect wetting*, the droplet tends to deform into a film that spreads over the whole surface eliminating completely the interface between the solid and the second phase.

For an equilibrium system, the electrostatic forces between molecules of one phase are the origin of the surface tension. Molecules at the interface between two phases only experience attractive forces from other molecules of the same kind from one side. To enlarge the surface, one has to bring additional molecules to the surface and perform work against these forces (see Figure 4.1A). This work per area is the *specific surface energy* $\epsilon$. The total force that is needed to expand the surface per unit length is the surface tension $\sigma$ (see Figure 4.1B). In passive systems where intermolecular forces are the only forces, both quantities are equal $\sigma = \epsilon$[188]. This also holds for nematic-isotropic mixtures[189]. A third equivalent definition in equilibrium is via thermodynamic potentials. In active systems, however, additional active forces can appear at the boundary that add to the surface tension and lead to different results for the different definitions[190, 191].

Stresses in general and in particular pressure in active systems have been studied intensely, but mostly for active Brownian particles, in particle as well as related continuum models[47, 49, 52, 98, 132, 133, 190–195]. Active Brownian particles show *motility-induced phase-separation (MIPS)*. This means that two phases form spontaneously, a high-density and a low-density phase. The interface between these two phases shows interesting properties. In certain regimes, near the onset of MIPS,

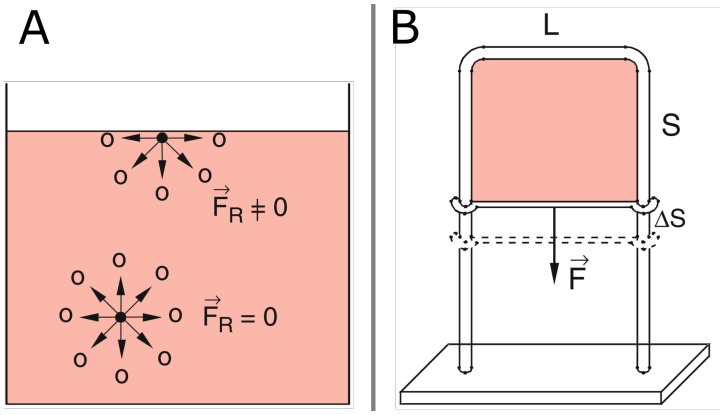


**Figure 4.1** *Illustrative sketches for the phenomenon of surface tension.* (A) Molecules in the bulk experience no net force ($\vec{F}_R = 0$) as intermollecular forces are the same from all sides. A molecule on the surface in contrast is pulled into the corresponding phase as forces only act from one side. (B) Example setup to measure the surface tension. A soap film spans between the wires of a wire frame. To pull down the lower bar of the frame, and hence enlarge the surface by the amount $L\Delta S$, one has to exert a certain force $\vec{F}$. The surface tension $\sigma$ is defined as this force per unit length: $2\sigma = |\vec{F}|/L$ (the factor 2 is because there are two interfaces, each on one side of the film). Both panels reprinted by permission from Springer Nature: "Reale feste und flüssige Körper" by Wolfgang Demtröder © 2015.

the phase separation dynamics can be described with an effective free energy like in equilibrium systems[196, 197]. Also when this is not possible, pseudoquantities like a pseudodensity or a pseudotension can be defined that are mathematically analogous to the corresponding equilibrium quantities[47, 52, 98, 194]. The problem is however, that there is no physical interpretation for these pseudoquantities. As a consequence, these cannot be measured, for example pseudotensions could not be measured in a setup as depicted in Fig. 4.1B as these methods miss the contributions caused by the activity[47, 52]. This can even lead to negative interfacial tensions[52, 132, 133, 192], a condition under which phase separation could not be sustained in equilibrium. In active systems however, active contributions can compensate for that. In the process, also novel phenomena could be observed, for example inverse Ostwald ripening[194].

Other active systems for which interfacial effects have been investigated are active Lennard-Jones particles[190] and, especially in the context of self-assembly of cell organelles, active emulsions that are driven away from thermodynamic equilibrium by sustained chemical reactions[198, 199]. However, to my knowledge, the problem is largely unexplored for active nematic systems.

In section 4.2 we will first look at a flat film of active nematic matter on a flat surface. In analogy to an equilibrium setup, we will calculate the surface tension $\sigma$ in section 4.2.1 from numerical simulations and analytically only taking into

account free energy contributions. We will then briefly test the stability of such a film depending on the film height and the strength of the active forces (section 4.2.2). In the main section of this chapter (section 4.3), we will give a qualitative overview over the properties of a droplet of nematic material on a flat surface and try to identify candidates for mechanisms that determine the steady-state shape of such a droplet. At the end of the chapter, we will try to summarise the findings from the three studies, especially in terms of what can be deduced about interface effects (section 4.4).

The hydrodynamic model used in this section is exactly the same model for a two-phase system consisting of an active nematic and an isotropic phase in two dimensions as in the previous chapter 3, except that the growth mechanism is switched off and hence the total mass of active nematic material is conserved. Parameter values used, unless otherwise noted, are also the same: $D = 0.08$, $C_{LQ} = 0.15$, $K_Q = 0.02$, $K_\phi = 0.08$ as coefficients for the free energy, $\Gamma_\phi = 0.2$, $\Gamma_Q = 0.4$ as diffusion constants, a tumbling parameter $\xi = 0.7$, viscosity $\eta = 1/6$, and the mean density is fixed to $\langle\rho\rangle = 40$. In the examples for the droplet, we work with activity $\zeta = 0.0050$.

To conclude these introductory remarks I want to present a short recap of active forces at interfaces and specifically the *active anchoring* effect.

**Active anchoring effect.** As already mentioned in the previous chapter, for finite activity the active force at an isotropic-to-nematic interface will favour a certain orientation of the director relative to the interface. This was first reported by Blow *et al.* [112]. I want to briefly retrace his derivation of the phenomenon here, because it will be important in the following discussion as it plays a major role for the shape and stability of films and droplets.

The active force $F_\alpha^{\text{act}}$ is the gradient of the active stress $\Pi_{\alpha\beta}^{\text{act}}$ (Eq. (3.16)):

$$F_\alpha^{\text{act}} = \partial_\beta \Pi_{\alpha\beta}^{\text{act}} = -\zeta \partial_\beta \left(Q_{\alpha\beta}\phi\right), \tag{4.1}$$

with phase field $\phi$, nematic tensor $Q_{\alpha\beta}$, and activity $\zeta$. This can be expressed in terms of the nematic order parameter $S$ and the director $n_\alpha$:

$$F_\alpha^{\text{act}} = -\zeta \partial_\beta \left(\phi Q_{\alpha\beta}\right) = -\zeta \left(\partial_\beta \phi S\right)\left(2n_\alpha n_\beta - \delta_{\alpha\beta}\right) - 2\,\zeta\phi S\left(n_\alpha\left(\partial_\beta n_\beta\right) + \left(\partial_\beta n_\alpha\right) n_\beta\right), \tag{4.2}$$

where we have used $Q_{\alpha\beta} = S\left(2n_\alpha n_\beta - \delta_{\alpha\beta}\right)$. As the interface is defined by the line where the phase $\phi$ and the nematic order parameter $S$ change from 0 to 1, the normal vector can be defined in terms of the gradient of these quantities. We thus define $\vec{m} \equiv -\nabla(\phi S)/|\nabla(\phi S)|$ as the outward surface normal vector and $\vec{t}$ as the surface tangent vector. With that, we can decompose the force density into the component parallel to the surface $F_\parallel^{\text{act}}$ and the component perpendicular to it

$F_{\perp}^{\text{act}}$. Assuming that gradients in the director $n_\alpha$ are negligible, an assertion that is justified when looking at perturbations around a uniform state, we get:

$$F_{\perp}^{\text{act}} = m_\alpha f_\alpha = \zeta \left|\nabla (\phi S)\right| \left(2 (m_\alpha n_\alpha)^2 - 1\right), \tag{4.3}$$

$$F_{\parallel}^{\text{act}} = t_\alpha f_\alpha = 2\, \zeta \left|\nabla (\phi S)\right| (t_\alpha n_\alpha) \left(m_\beta n_\beta\right). \tag{4.4}$$

Depending on the sign of the activity $\zeta$, the normal force on the interface $F_{\perp}^{\text{act}}$, points outwards ($\zeta < 0$) or inwards ($\zeta > 0$) for $\vec{n} \perp \vec{m}$ and hence induces active forces pushing the interface outwards or inwards, respectively. For $\zeta > 0$, the case we consider, the inwards-pointing force is balanced by the pressure-drop across the interface and no net forces act on the interface, hence this configuration is stable. A more detailed analysis reveals that in this situation also the corresponding $F_{\parallel}^{\text{act}}$ is stabilizing the system as oblique angles induce flows that rotate the director into the parallel direction[112].

## 4.2 Films

### 4.2.1 Estimation of the elastic surface tension

To estimate the equilibrium surface tension we consider a flat isotropic-nematic interface. Analytically, we will calculate the surface tension for a one-dimensional model using the expression for the free energy as given in Equation (3.1). In simulations, we analyse a section through a stripe of active material at a no-slip wall perpendicular to the interface, which results in a quasi one-dimensional setup (see Fig. 4.2A).

For the analytical treatment, we need to get a simplified expression for the free energy density $f$ from Equation (3.1). For that, we will rewrite $f$ as

$$f = f_{\text{binary}} + f_{\text{coupling}} + f_{\nabla\phi} + f_{\nabla Q}, \tag{4.5}$$

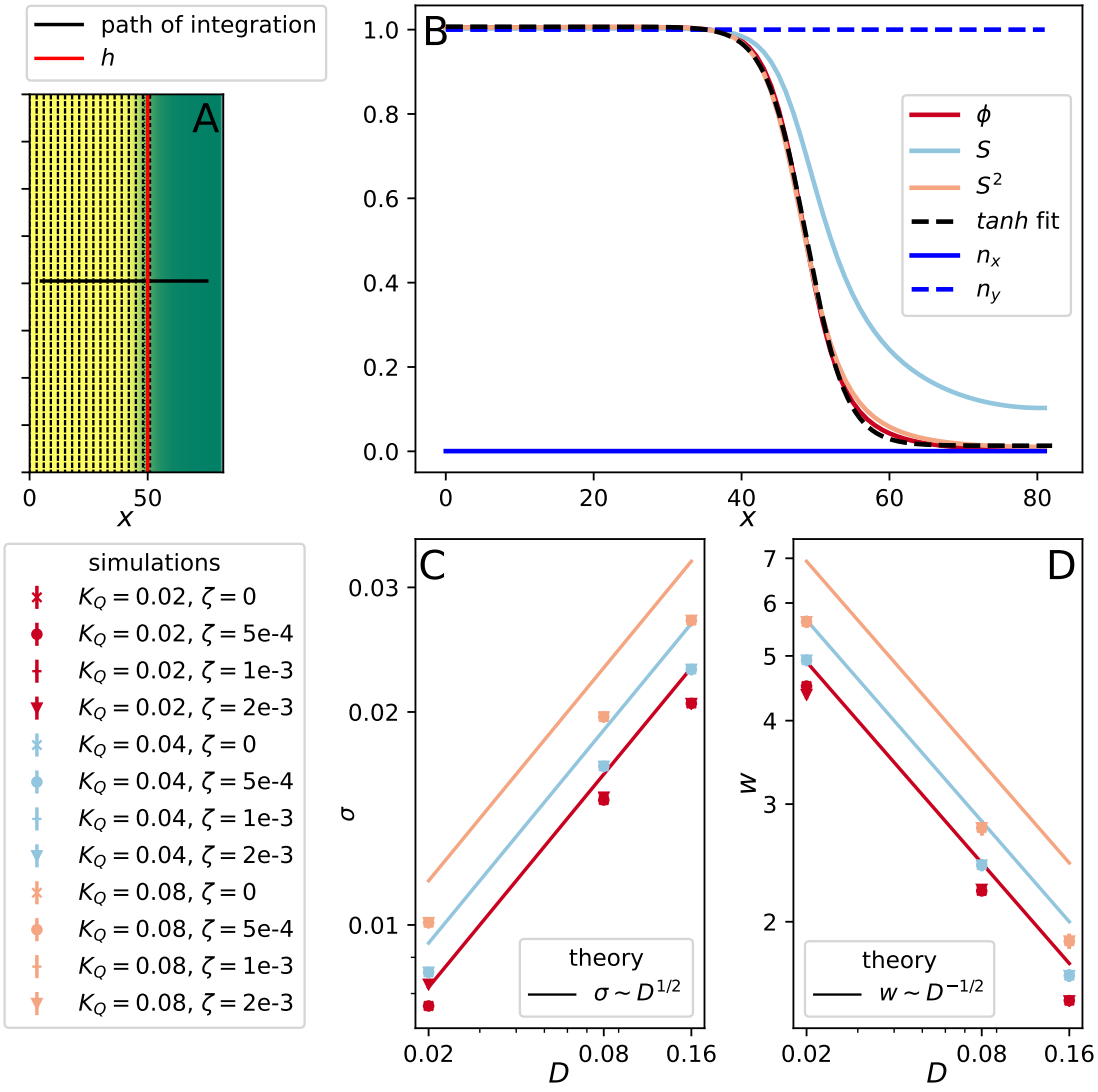


**Figure 4.2** *Analysis of interfacial profile for the phase field $\phi$.* (A) Quasi one-dimensional setup for analysis of interface shape and surface tension. The nematic phase is shown in yellow, the isotropic phase in green. Black lines indicate the orientation of the director. On the left side, the system is confined by a no-slip boundary. (B) Phase field $\phi$, nematic order parameter $S$ and its square $S^2$, components of the director $n_\alpha$, and fit of a hyperbolic tangent to $\phi$ along the section indicated by the black line in A. (C,D) Comparison of surface tension $\sigma$ as well as interface width $w$ measured in simulations to the corresponding theoretical predictions. Activity has no impact on the results and theory correctly predicts the scaling with the binary bulk coefficient from the free energy $D$.

using the following definitions for the individual parts:

$$f_{\text{binary}} = \frac{1}{2} D\phi^2 (1-\phi)^2 , \tag{4.6}$$

$$f_{\text{coupling}} = \frac{1}{2} C_{LQ} \left(\phi - \frac{1}{2} Q_{\alpha\beta} Q_{\alpha\beta}\right)^2 , \tag{4.7}$$

$$f_{\nabla\phi} = \frac{1}{2} K_\phi \partial_\gamma \phi \partial_\gamma \phi, \tag{4.8}$$

$$f_{\nabla Q} = \frac{1}{2} K_Q \partial_\gamma Q_{\alpha\beta} \partial_\gamma Q_{\alpha\beta}. \tag{4.9}$$

As in chapter 3, $D$, $C_{LQ}$, $K_\phi$, and $K_Q$ are positive material constants, $Q_{\alpha\beta}$ is the nematic tensor, $S$ the nematic order parameter, and $\phi$ the phase field. $f_{\nabla\phi}$ and $f_{\nabla Q}$ are interface terms that punish gradients in $\phi$ and $Q_{\alpha\beta}$, respectively. $f_{\text{coupling}}$ ensures a tight coupling between the magnitude of the nematic order parameter $S = \sqrt{\frac{1}{2} Q_{\alpha\beta} Q_{\alpha\beta}}$ and the phase field $\phi$. $f_{\text{binary}}$ is a mixing energy with the binary bulk coefficient $D$ that corresponds to the mixing parameter in Flory-Huggins theory. Together, these terms facilitate phase separation into an active nematic ($S = 1, \phi = 1$) and a passive isotropic ($S = 0, \phi = 0$) phase, comparable to a Cahn-Hilliard model[38, 168].

Following [200], we first note that in simulations the square of the nematic order parameter $S^2$ closely follows the phase field $\phi$ and hence the coupling term vanishes $\frac{1}{2} C_{LQ} \left(\phi - \frac{1}{2} Q_{\alpha\beta} Q_{\alpha\beta}\right)^2 \approx 0$ as intended (see Fig. 4.2B). This is also the case in the more complex invasion setup presented in chapter 3. Due to the active anchoring effect explained in section 4.1, the director is parallel to the interface ($n_x = 0, n_y = 1$) and the nematic tensor can be written as $Q_{\alpha\beta} = S\left(2 n_\alpha n\beta - \delta_{\alpha\beta}\right) = S\left(2\delta_{\alpha y}\delta_{\beta y} - \delta_{\alpha\beta}\right)$ Hence, gradients in $Q_{\alpha\beta}$ reduce to gradients in $S$. The nematic elastic term then reduces to:

$$f_{\nabla Q} = K_Q \partial_\gamma S \partial_\gamma S. \tag{4.10}$$

To further simplify the equation, we now make the the additional approximation $S \approx \phi$ which is not too far off (see Fig. 4.2B). Altogether, we then can write Equation (4.5) as a function of the phase field $\phi$ only. Equation (4.5) thus reduces to:

$$f = f_{\text{binary}} + \frac{K_\phi + 2K_Q}{2} \partial_x \phi \partial_x \phi. \tag{4.11}$$

The boundary conditions in our setup are $\phi(x = 0) = 1$ and $\phi(x \to \infty) = 0$.

Equation (4.11) has the form of a conventional Cahn-Hilliard free energy. Under the assumption that the width of the interface is small compared to the film height

$h$, it is minimised by $\phi(x) = \frac{1}{2} - \frac{1}{2}\tanh\left(\frac{x-h}{w}\right)$ with $w = 2\sqrt{\frac{K_\phi+2K_Q}{D}}$ the interface width[201].

Inserting this approximate solution into the simplified expression for the free energy density (4.11) and integrating $f$ from $x = 0$ to $x = \infty$ (again assuming $h \gg w$) yields for the surface tension $\sigma$:

$$\sigma = \int_0^\infty \mathrm{d}x\, f \approx \frac{1}{6}\sqrt{D\left(K_\phi + 2K_Q\right)}, \tag{4.12}$$

which is the same result as in [200]. In Figure 4.2C,D, we compare analytical results for interface width $w$ and tension $\sigma$, respectively, to what we obtain in simulations for different values of the energy coefficients $D$, $K_Q$, and the activity $\zeta$. This is only possible for low activities $\zeta$ since the film will become unstable above a certain activity, as we will show in the next section 4.2.2. We do that by initialising a stripe of active material at a no-slip wall, waiting for it to reach a steady state, and then looking at a section perpendicular to the interface which results in a quasi one-dimensional setup (see Fig. 4.2A). We fit a hyperbolic tangent to the resulting profile of the phase field $\phi$ (see Fig. 4.2B) from which we can extract the interface width. The surface tension is obtained by direct numerical integration over the free energy density $f$ across the interface along the same section.

Despite the approximations made in calculating the free energy, the scaling of width $w$ and surface tension $\sigma$ with the binary bulk free energy coefficient $D$ in the simulation data agrees with the analytical prediction. We also note that the activity $\zeta$ has no influence on the results which justifies our assumption to neglect active forces and base the deduction on purely energetic arguments.

We conclude, therefore, that observations reported in this section show that the surface tension $\sigma$ (i) scales with the binary bulk coefficient $D$ as $\sigma \propto D^{1/2}$ and (ii) is independent of the activity $\zeta$ as long as it is not strong enough to distort the film's straight interface. However, it should be mentioned that the orientation of the director $n$ at the surface can alter the surface tension. First, because gradients in $n$ contribute to the free energy. Second, because if the director is not parallel or perpendicular to the surface, additional tangential active forces appear, as predicted by Equation (4.2). Furthermore, the influence of active forces in this case changes the nature of the surface tension fundamentally as it is not necessarily equal to the specific surface energy anymore: $\sigma \neq \epsilon$.

### 4.2.2 Stability of a layer of active matter on a wall

We again consider an active nematic layer on a flat wall as depicted in Fig. 4.2A. For low activity $\zeta$, velocities relax to zero everywhere and the interface remains straight. Beyond a certain value for the activity, velocity field in the system increases to finite

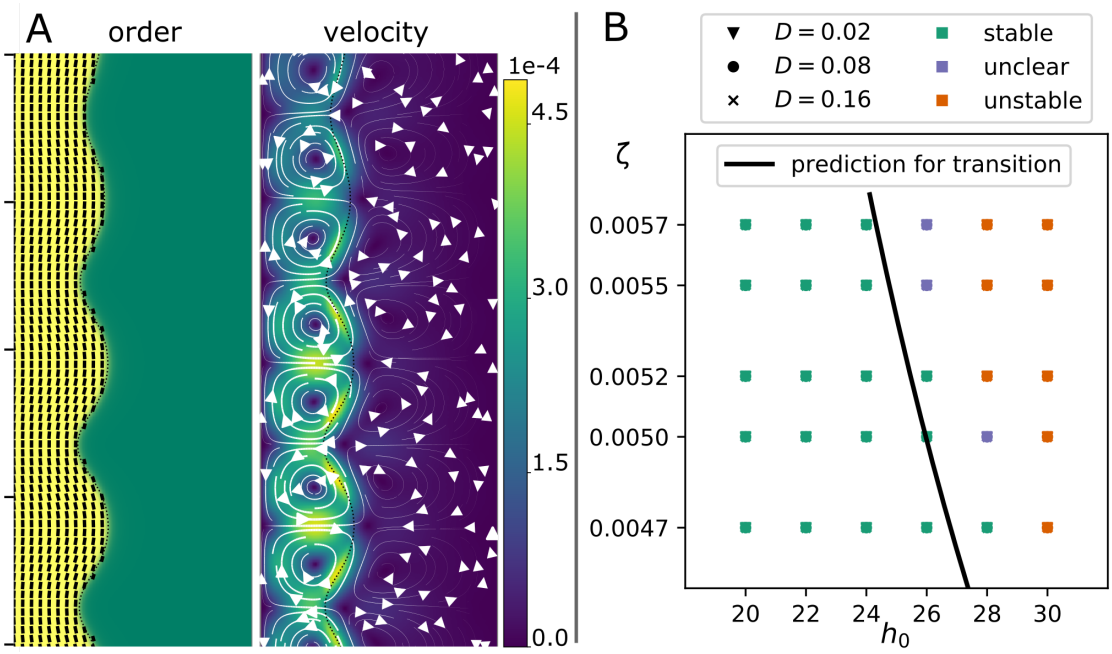


**Figure 4.3** *Analysis of stability of a film of active matter on a wall.* (A) Onset of instability, left side: nematic order field, right side: velocity field with colour code (B) "Phase diagram" of the system. The criterion for a sample to be classified as "stable" is that velocity decays to zero everywhere. The results are the same for all values of the binary energy coefficient $D$ (markers fall on top of each other). Thicker films (larger initial thickness $h_0$) are less stable for constant activity $\zeta$. The cases qualified "unclear" could be lifted by longer observation times. Theoretical prediction after [200].

values expressing characteristic vortices. This leads to growing deformations in the layer (see Fig. 4.3A). At the onset of the instability, the deformations of the nematic-to-isotropic interface are sinusoidal. The director follows the interface, at least partially, due to the effect of active anchoring (more detailed explanation in section 4.1). This deformation in the director extends into the bulk indicating that the transition is not a pure surface phenomenon. At a later state state, the dynamics get increasingly complex, which can also include the rupture of the film.

In Figure 4.2B, we analyse the stability of the film under variations in its initial height $h_0$, the binary bulk coefficient $D$, and the activity $\zeta$. Interestingly, there is no dependence on $D$, and hence the surface tension $\sigma$, at least not for the parameter samples considered. In general, thicker films are less stable than thinner ones as are systems with higher activity. This is in accordance with the results of similar previous studies by Blow *et al.*[200]. There, an almost identical model for an active nematic was used, but the anchoring condition for the director at the no-slip wall was chosen to be orthogonal to the surface and hence together with the active anchoring

effect induced a non-homogeneous director field in the film. Quantitatively, in our simulations the transition takes place for slightly lower values of activity $\zeta$ and initial film height $h_0$. In that work, also theoretical values for the transition were predicted using linear stability analysis based on simplified hydrodynamic equations taking into account viscous, elastic and active stresses, but excluding interface effects (black line in Fig. 4.2B). However, it must be noted that a heuristic correction was applied to the calculated transition value. Without that correction, the line would be shifted to the left by about 7 units of $h_0$ in Fig. 4.2B, but still show the correct trend. The critical wavelength was calculated to be at 44 for our parameters. In our simulations, we observe roughly 57 (7 full wavelengths in a box of length 400) which is reasonably close. However, one must note that Blow *et al.* in their computational analysis also found the transition to slightly depend on surface tension. Resolving this effect would maybe require a more fine graded sampling of parameter space.

To summarise, these findings suggest the following conclusions: at least for the values probed, the instability is independent of the surface tension $\sigma \propto D^{1/2}$, but depends on the initial height $h_0$ of the film. This shows that the instability is not a pure surface phenomenon. The instability is sinusoidal with a finite wavelength. It can be predicted approximately with a linear stability analysis of simplified hydrodynamic equations that takes into account the competition viscous, elastic and active stresses, but does not consider surface tension.

## 4.3 Droplets

In this section, we want to look at a droplet of active nematic material on a flat solid wall. Previous studies used a parametrisation of the interface as a $d-1$-dimensional surface coupled to an active nematic[202] or active polar[203] field instead of using a phase-field description to model two different phases as we do here.

The two-dimensional study of Joanny and Ramaswamy in [202] assumed alignment of the director with the interface as it is caused by the active anchoring effect as well as with the solid surface. As these two conditions have to be fulfilled simultaneously close to the contact points where the nematic-isotropic interface meets the solid wall, this results in very small contact angles. This is different to our study where contact angles and director alignment emerge from the dynamics and are not prescribed. Under these assumptions however, quantitative predictions for the scaling of the droplet height with the strength of the active force and a spreading law could be obtained.

As a minimal model for the motion of cells, also the ability of droplets to move on surfaces driven by active forces has been investigated. Asymmetric motion of droplets can be achieved in several ways: by implementing polar fields[204–206],

by velocity fields generated by prescribed winding of the nematic director field across the drop heigh[206, 207], or by capillary forces resulting from differing contact angles[206].

In the following, we will describe in detail the results of numerical simulations for the dynamics of a droplet of active nematic in the hope to gain an intuition about the mechanisms that determine its steady-state shape.

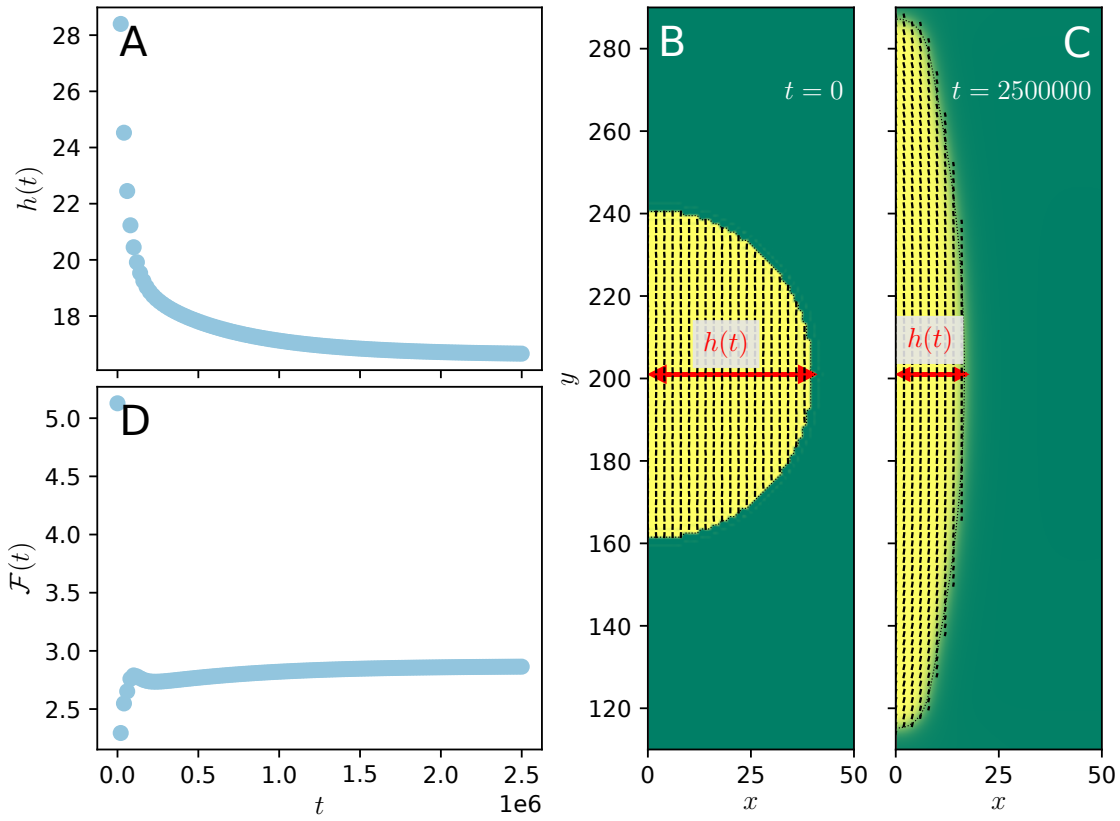


**Figure 4.4** *Simulation setup and example for time evolution.* (A) Time evolution of the maximum height of the droplet $h(t)$ for activity $\zeta = 0.0050$ as a measure for the "flatness" of the droplet. In (B,C), the droplet is shown at the start of the simulation and when the steady state is reached, respectively. The active nematic phase ($\phi = 1$) is displayed in yellow, the isotropic passive phase ($\phi = 0$) in green. The black lines depict the director orientation in the nematic phase. As can be seen, the maximum height is attained at the centre of the droplet because of its symmetric shape. (D) Total free energy $\mathcal{F}$ of the system. The rapid drop at the beginning shows the fast relaxation of the artificially imposed initial conditions (director parallel to wall with small perturbations). From (A) and (D) we can infer that the droplet has obtained a steady state at the end of the simulation period.

### 4.3.1 Setup and overview

In Figure 4.4B, we see the initial configuration of the setup we use for our numerical simulations, a semicircle of active nematic phase on a flat solid wall with contact angles of 90°. We employ the parameters as specified in section 4.1. To the fluid, the wall imposes a no-slip boundary, the phase field $\phi$ and the nematic tensor $Q_{\alpha\beta}$ are subject to Dirichlet boundary conditions there. As we have not introduced terms causing surface tension for the solid-nematic and the solid-isotropic interface in the free energy density $f$ (4.5), this corresponds to the minimal-surface configuration the system would attain in equilibrium (which we can verify in simulations with activity $\zeta = 0$). For the example shown in Fig. 4.4 with $\zeta = 0.0050$, the blob deforms into a more flat shape due to the active forces until a steady state is reached (Fig. 4.4C). For this, also the initial condition on the orientation of the director field is important. In our example, as we work with an extensile nematic ($\zeta > 0$), this is the configuration where the director is oriented parallel to the wall ($n_x = 0, n_y = 1$), only disturbed by small initial noise. If the director were oriented perpendicular to the wall, the droplet would contract in $y$-direction and grow in $x$-direction and eventually deform further due to lateral instabilities (results not shown). In our case, the active force is directed towards the droplet (see Equation (4.2)) and counteracted by the wall. Due to the symmetry relative to the centre of the droplet in $y$-direction, a stable steady state is reached. The main observable to measure droplet deformation is the height of the blob at its center $h$, i.e. the perpendicular distance from the wall to the nematic-isotropic interface at $y = 200$, as also indicated in Figure 4.4B,C.

In Fig. 4.4A and D the time evolution of the droplet height $h$ as well as the total free energy $\mathcal{F} = \int \mathrm{d}^2\mathbf{r}\, f$ are plotted. We see that the decrease of $h$ becomes slower over time. In parallel, the free energy $\mathcal{F}$ rises in the beginning, and after going through a small dip, eventually attains a maximal value, which is a strong indicator for non-equilibrium dynamics. Dynamics in both observables significantly slow down towards the end of the simulations. This justifies the assumption that the systems attains a steady state.

In the following section, we will look at the qualitative properties of the steady-state example shown in Figure 4.4D in more depth.

### 4.3.2 Order and velocity field

In Figure 4.5, a set of observables are plotted that help to characterise the steady state.

Next to the order and director fields, this includes the fluid density $\rho$ which is higher in the ordered phase. This corresponds to a higher pressure there (see Equation (3.14)). Particularly interesting is the area next to the three-phase contact-

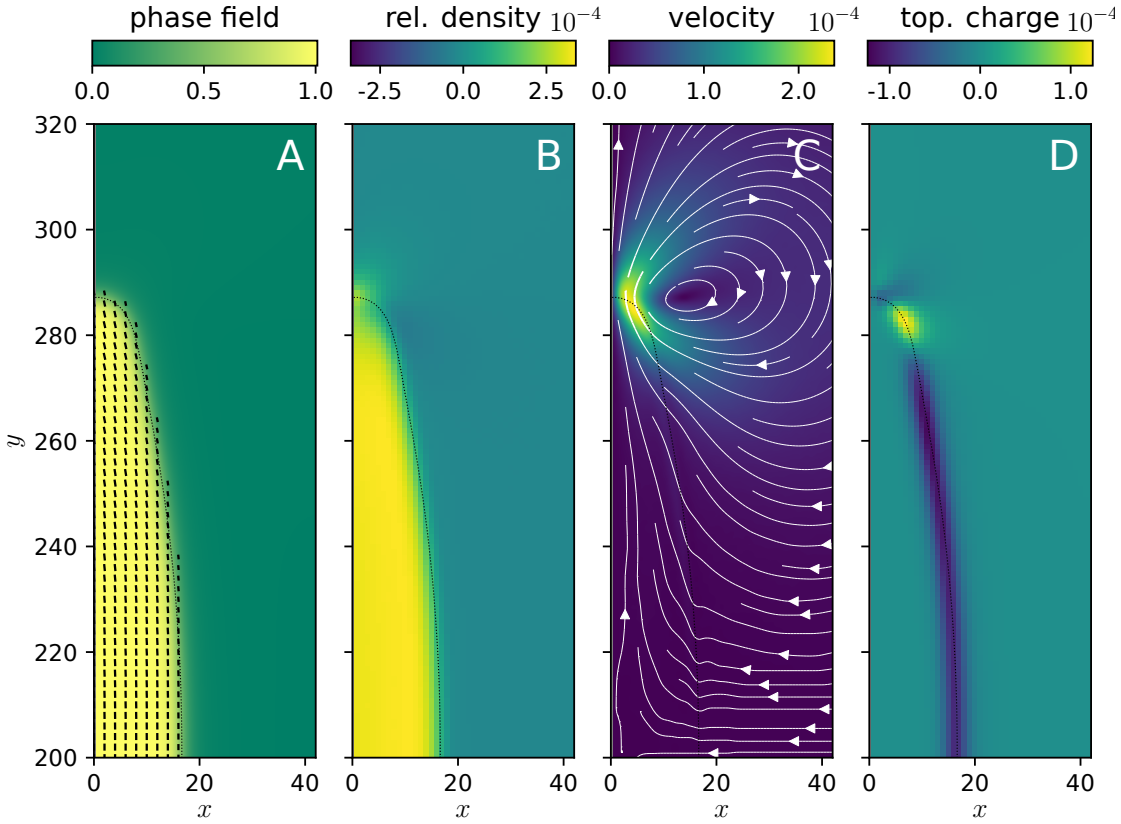


**Figure 4.5** *Observables in steady state.* Only one half of the droplet is shown as the droplet is symmetric to the axis where the height is the largest. (A) Phase and order field as in Fig. 4.4. (B) Relative deviation from mean fluid density $(\rho - \langle\rho\rangle)/\langle\rho\rangle$ across system. Inside the droplet, the density is higher. The gradient is realtively steep where the interface is flatter. Close to the contact point of the three interfaces, where the interface curves more strongly, the gradient in $\rho$ is smoother. At the same point, the velocity field $\vec{u}$ peaks and forms a vortex while it is nearly zero otherwise (C). (D) Topological charge density $q$. Spatial denpendency is similar as for the velocity field and fluid density: $q$ is negative (blue) along the flat part of the interface while close to the contact point, there is a small region of positive $q$ (yellow).

point where the nematic-isotropic interface hits the solid wall. Here, the interface has the largest curvature. In this region, the density gradient across the interface is less steep than at other positions. Concomitantly, the velocity field $\vec{u}$ attains higher values here. While it is (close to) zero everywhere else in the system, at this point we observe a vortex with the velocity pointing outwards at the interface. Away from the vortex, the velocity field decays rapidly.

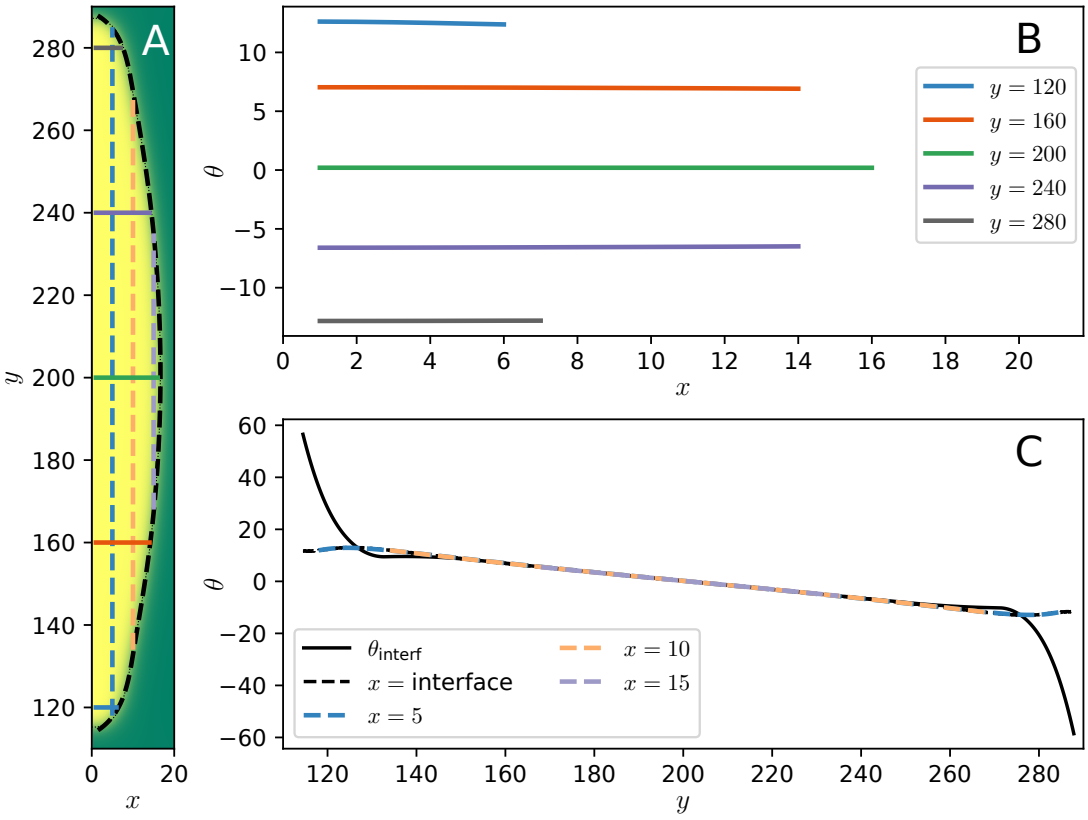


**Figure 4.6** *Director field along sections through the droplet.* (A) Illustration of sections along which director inclination is shown in (B,C): solid lines in (B) show director inclination along solid lines of same colour through the droplet in A, analogously dashed lines in (C). (B,C) show the angle of the director relative to the $y$-axis. In (B), sections are along lines of constant $y$. Two features are apparent: the angle is constant along the sections and its absolute value symmetrically increases with increasing distance from the droplet centre. In (C), the reason becomes clear. The black solid line shows the inclination of the interface, the black dashed line the director angle along the same line. For $y$-values where the interface is relatively flat, the director follows it closely for all $x$. Where the interface inclination varies more strongly, the director ceases to follow.

Another observable related to nematic order is the topological charge density $q$ defined as[112]:

$$q = \frac{1}{4\pi}\left(\partial_x Q_{x\alpha}\partial_y Q_{y\alpha} - \partial_x Q_{y\alpha}\partial_y Q_{x\alpha}\right). \tag{4.13}$$

This form is an extension of the classical definition for bulk nematic liquid crystals for two-phase systems. The integral over $q$ over an area that contains a topological defect gives topological charge $\pm 1/2$ in bulk nematic liquid crystals[208]. As [112]

notes, “curved interfaces in general have a [nonzero topological] charge density. Assuming the director takes a constant orientation with respect to the interface, the charge density is positive for concave and negative for convex interfaces.” As the droplet interface is convex everywhere in our simulation, $q$ indicates the orientation of the director relative to the interface. While $q$ is negative over most of the interface indicating a constant relative orientation of the director $n_\alpha$, just at the position where we observe the peak in velocity, the charge density switches to a positive sign indicating a change in relative orientation of $n_\alpha$ to the boundary.

In Fig. 4.6 the director orientation inside the nematic phase is shown along sections through the droplet to allow a closer look at the variations of the director along the interface. The first observation is that the director is essentially constant along lines of constant $y$ while it follows the inclination of the interface over most parts of its length, namely the parts where the inclination of the interface varies only slowly with $y$. This can be understood qualitatively by the competition of active anchoring at the interface and energetic penalties for deformations in the director field: as long as variations in the surface inclination are minor, active anchoring is stronger than the elastic forces. At the position where the interface inclination crosses over from slow variation to faster variation with $y$, the director stops to follow and is constant for larger $y$, because elastic restoration forces are stronger than active anchoring. Due to the flat shape of the blob, this point is quite close to the position where the interface touches the solid wall. This change in relative orientation of director and interface leads to the small section of the interface with positive topological charge density $q$ that can be observed in Figure 4.5D. Beyond this short section, $q$ becomes negative again.

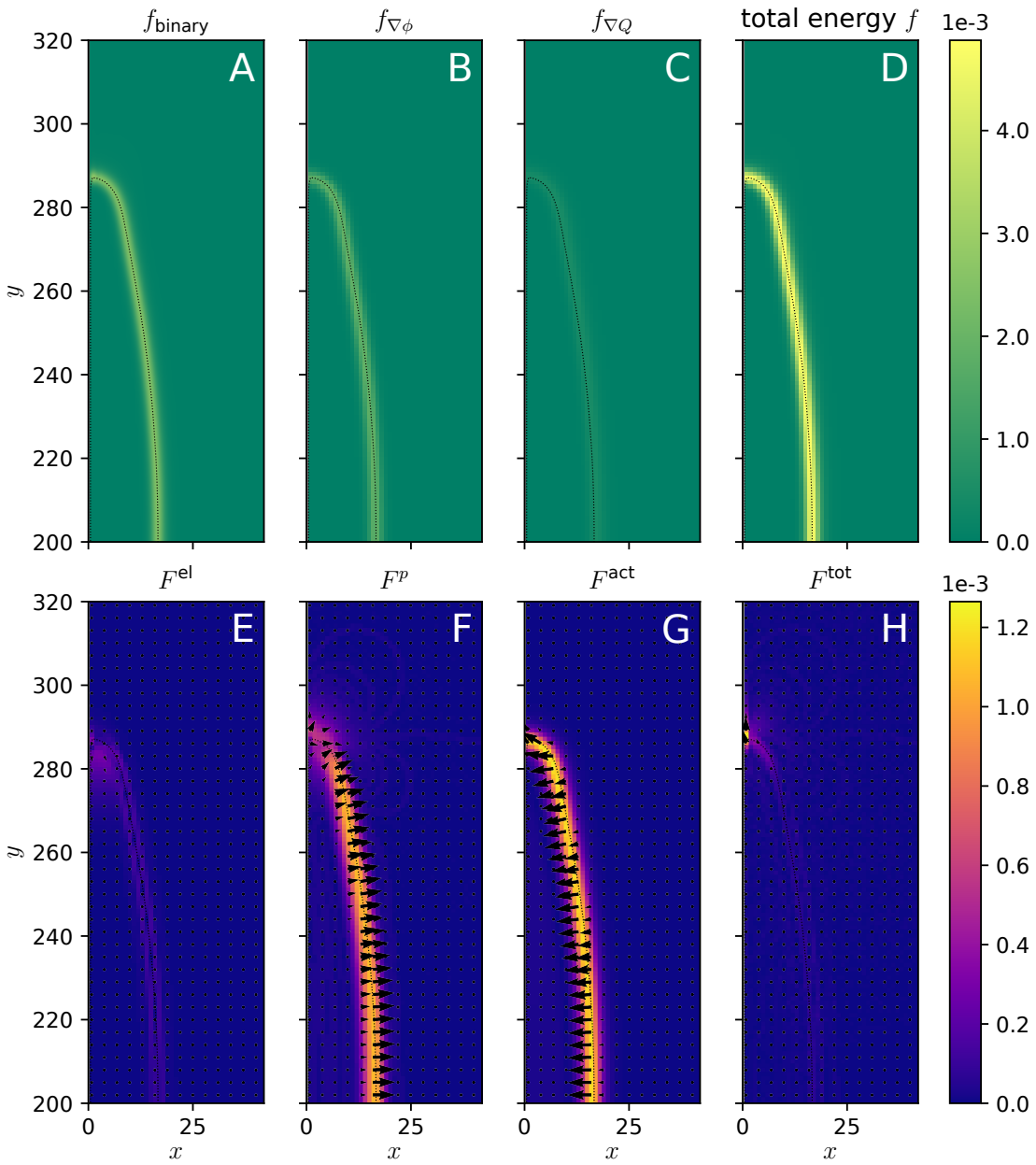


**Figure 4.7** *Free energy density and forces.* (A-C) Contributions to the free energy density (except coupling term), (D) total free energy density $f$. We see that interface contributions are dominant. (E-H) Selected forces and total force. Clearly, $F^p_\alpha = -\partial_\alpha p_0$ as well as $F^{\text{act}}$ are dominant and cancel over most of the interface. Only close to the contact point, elastic and viscous force (latter not shown) contribute significantly and the total force $F^{\text{tot}}$ is finite, pointing outwards from the droplet. A detailed view on forces along the interface is given in Figure 4.8.

Next to the director, the velocity field $\vec{u}$ deserves closer investigation as via the advection term $\partial_\beta(\phi u_\beta)$ it affects the phase field (see Equation (3.3)) and hence the shape of the droplet. The velocity field is determined by the forces that are its sources on the right-hand side of Eq. (3.11). The central question in this context is which forces, and hence which physical effects, are dominating the flow dynamics. To this end, we define the following forces derived from the stresses (3.12)-(3.16):

$$F_\alpha^{\mathrm{el}} = \partial_\beta \Pi_{\alpha\beta}^{\mathrm{el},1}, \tag{4.14}$$

$$F_\alpha^{\mathrm{mol}} = \partial_\beta \Pi_{\alpha\beta}^{\mathrm{el},2}, \tag{4.15}$$

$$F_\alpha^{\mathrm{visc}} = \partial_\beta \Pi_{\alpha\beta}^{visc}, \tag{4.16}$$

$$F_\alpha^{\mathrm{act}} = \partial_\beta \Pi_{\alpha\beta}^{\mathrm{act}}, \tag{4.17}$$

$$F_\alpha^{p} = -\partial_\alpha p_0. \tag{4.18}$$

$F_\alpha^{\mathrm{el}}$ and $F_\alpha^{\mathrm{mol}}$ sum up the effects of elastic stresses. The force $F_\alpha^{\mathrm{mol}}$ specifically represents the contributions that are due to the interplay of the nematic order parameter and the fluid flow. $F_\alpha^{\mathrm{visc}}$ is the viscous force, $F_\alpha^{\mathrm{act}}$ the active force already analysed in section 4.1, and $F_\alpha^{p}$ the force resulting from pressure gradients.

It turns out that not all forces are on the same order of magnitude. Although the total free energy $\mathcal{F}$ peaks along the interface (see Fig. 4.7A-D), $F^{\mathrm{el}}$ is significantly smaller than the pressures forces $F^{\mathrm{p}}$ and active forces $F^{\mathrm{act}}$(Fig. 4.7E-G) which are the dominant forces in the system. Over most of the interface, $F^{\mathrm{p}}$ points outwards in direction normal to the interface and $F^{\mathrm{act}}$ points inwards opposing to it. As a consequence, the resulting total force $F^{\mathrm{tot}}$ vanishes (see Fig. 4.7H). Only close to the position where the interface touches wall, the picture is different. Here, $F^{\mathrm{act}}$ and $F^{\mathrm{p}}$ develop a finite component tangential to the interface and $F^{\mathrm{visc}}$ (not shown) and $F^{\mathrm{el}}$ (Fig. 4.7E) are of comparable order. Also, the resulting total force is finite and points outwards causing the flows observed in Fig. 4.5C.

For better visibility, we have plotted the tangential and normal components of the active force $F^{\mathrm{act}}$, pressure force $F^{\mathrm{p}}$, and the total force $F^{\mathrm{tot}}$ along the interface in Figure 4.8. Here the finite total force close to the contact points is clearly visible. On the one hand, there is an outwards-pointing normal component, but also the tangential component that constitutes a non-energetic contribution to the surface tension becomes finite. In this context, it also must be noted that the overerall value of the free energy, and in particular the specific surface energy, does not have a considerable influence on the dynamics if all other parameters are kept equal (see Fig. 3 in the appendix).

This leads us back to the ideas outlined in section 4.1: next to elastic forces that derive from the free energy density $f$, other forces, mainly the active force $F^{\mathrm{act}}$, play an important role at the interface, at least at certain locations. The active

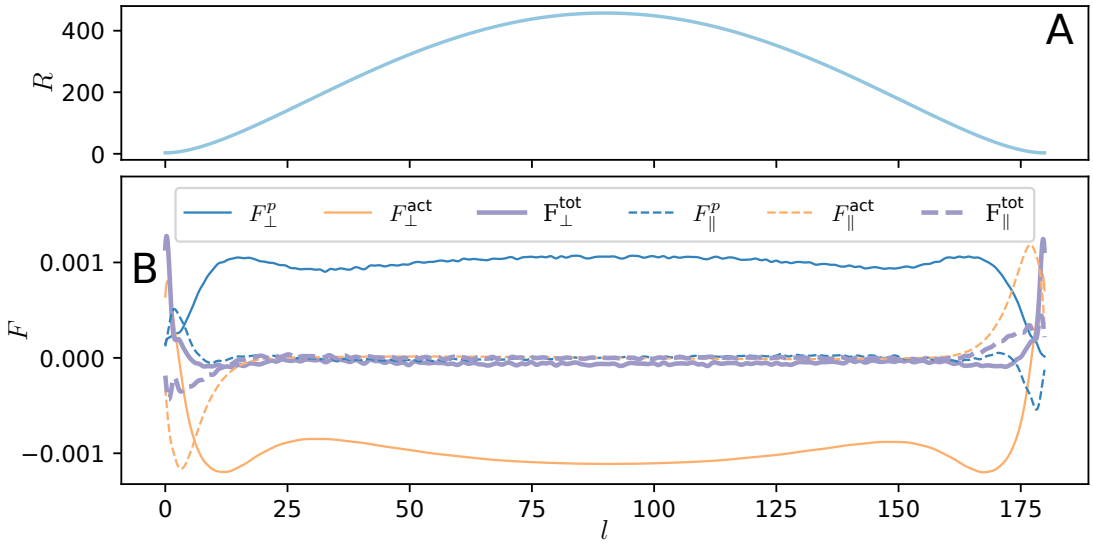


**Figure 4.8** *Analysis of nematic-isotropic interface.* (A) Radius along interface obtained from an elliptical approximation of the interface. $l$ parametrises the length of the interface from the lower contact position with the wall to the upper one. (B) Projection of forces perpendicular (solid lines) and parallel (dashed lines) to the interface. Tangential forces are zero over most of the interface. Perpendicular forces are not, but cancel, except close to the wall contact points. The approximation of the interface as an ellipse is discussed in more detail in section 1.3 of the appendix.

force is asymmetrically pointing inwards the drop and largely balanced by another asymmetric force, an induced density gradient that causes a pressure force $F^{\mathrm{p}}$. At the points of high curvature of the interface however, this balance is imperfect and hence flows emerge.

Ultimately the final droplet shape is determined by the equation for $\phi$, Equation (3.3). In Figure 4.9, we show how the advective and diffusive term cancel in this equation in the steady state. While advection is caused by active stresses, diffusion is due to energetic effects. Thus, effectively, it is the interplay between active and elastic forces that determines the final shape of the droplet.

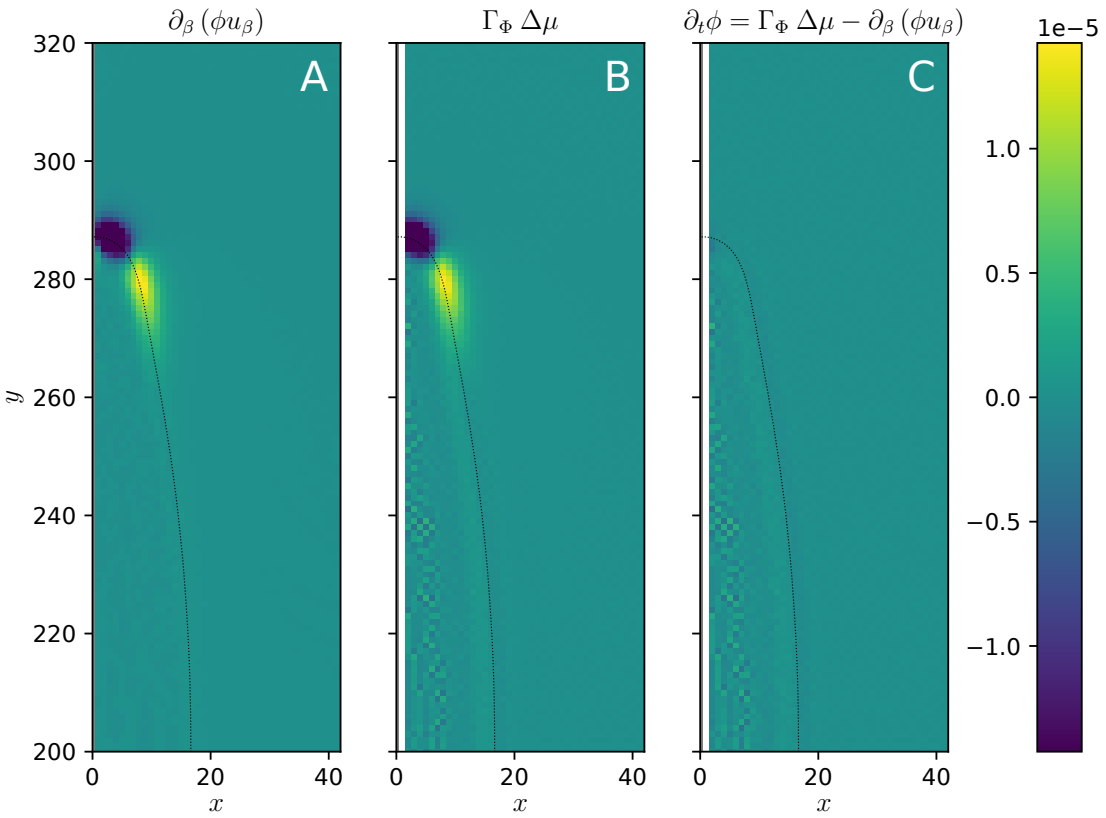


**Figure 4.9** *Terms governing the phase-field dynamics.* (A) Advective term $\partial_\beta\left(\phi u_\beta\right)$, (B) diffusive term $\Gamma_\phi\Delta\mu$. Both terms are finite only close to the contact point, but still cancel out everywhere. Thus, $\partial_t\phi$ is zero everywhere and a steady state is maintained (C).

### 4.3.3 Dependence of droplet dynamics and steady-state shape on activity

In Figs. 4.10 and 4.11, we compare the dynamics and steady-state values of several observables for variations in the activity $\zeta$. The timescales on which the steady state is reached do not depend on $\zeta$ significantly, however, the final values of the observables do as expected. In general, stronger active forces lead to flatter and more elongated droplets. For droplet height $h$, interface length $L$, and total free energy $\mathcal{F}$, the dependence is strongest for $\zeta \lessapprox 0.0025$, for activities higher than that variations are minute. The height $h$ varies from $h \approx 40$ for $\zeta = 0$ to around $h \approx 15$ for the highest values of $\zeta$ (Fig. 4.11A-C). The droplet height $h$ for high activities is thus reduced to around one third of the equilibrium value. The increase in $\mathcal{F}$ and $L$ looks qualitatively similar. Nevertheless, the quotient $\mathcal{F}/L$ (Fig. 4.11D) grows linearly with activity indicating that non-interfacial contributions increase as we have shown that the elastic surface tension $\sigma$ does not depend on $\zeta$ in section 4.2.1.

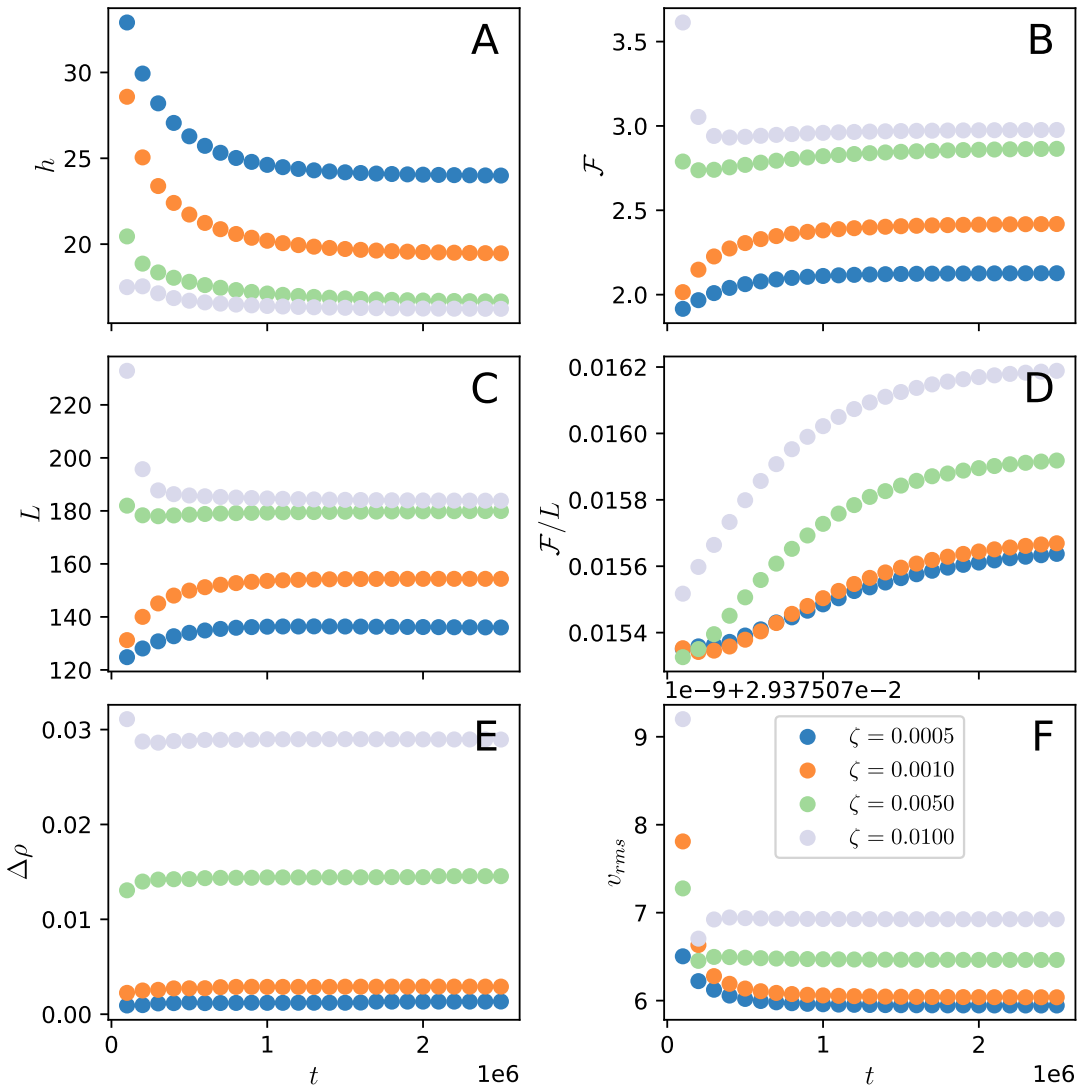


**Figure 4.10** *Time evolution of selected observables for different activities* $\zeta$. (A) Height of blob $h$, (B) free energy $\mathcal{F}$, (C) length of interface $L$, (D) quotient $\mathcal{F}/L$, (E) difference of fluid density between nematic and isotropic phase $\Delta\rho$, (F) mean squared velocity $v_{rms}$. All observables assume their steady state value after about half the simulation time except the surface tension. After $t$ = 2e6, in the last fifth of the interval, all observables are nearly constant.

A similar linear dependence is observed for the pressure difference $\Delta\rho$ (Fig. 4.11E). This is because a higher pressure gradient across the interface is necessary to balance the higher active forces. Higher active forces also cause higher root mean-squared velocities $v_{rms}$ (Fig. 4.11F).

In summary, this suggests the following interpretation of our results: higher active stresses are balanced by a steeper gradient in density $\rho$ over most of the perimeter. Only close to the contact points of the isotropic-nematic interface with the wall, where the curvature of the interface is high and the director does not follow the interface closely anymore, the total resulting force is finite and causes steady-state flows. These lead to advective contributions in the equation for the phase-field $\phi$ which are balanced by diffusive contributions, that eventually are of energetic origin.

The change of the director orientation along the interface motivates the following conjecture for the mechanism that determines the steady-state shape of the droplet: active anchoring, which becomes stronger with higher activities $\zeta$, makes the director align with the interface. However, if the director follows a curved interface, this leads to deformations in the bulk of the nematic. Both effects together lead to the formation of a flatter and more elongated droplet against the surface tension at the cost of a longer interface. This is in the spirit of what has been reported in [203]: the competition between active stresses and the conservation law for the nematic phase variable $\phi$ determine the final shape of the droplet. Admittedly, we still lack an explicative theory for the connection between shape and activity that in particular could explain the saturation in droplet height $h$ and interface length $L$ for higher activities. Still, our observations suggest that a deeper understanding of interfacial effects might be crucial to solve this problem although interface and bulk effects seem to be closely connected.

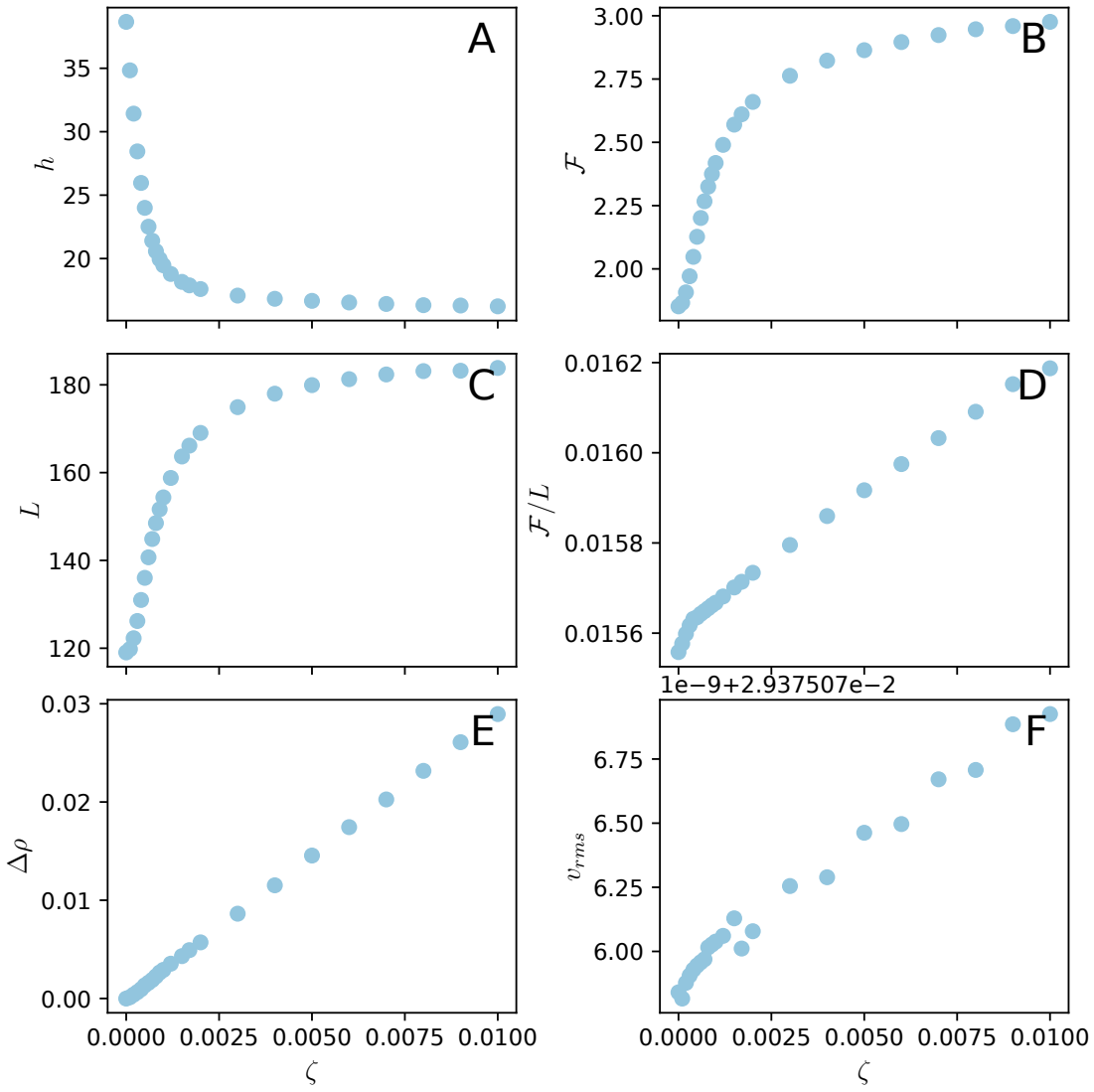


**Figure 4.11** *Steady-state values of selected observables for different $\zeta$.* (A) Height of blob $h$, (B) free energy $\mathcal{F}$, (C) length of interface $L$, (D) quotient $\mathcal{F}/L$, (E) difference of fluid density between nematic and isotropic phase $\Delta\rho$, (F) mean squared velocity $v_{rms}$. For increasing activity $\zeta$, the droplet becomes flatter and broader, but the dependence becomes less strong beyond $\zeta \approx 0.0025$. Interestingly, $\mathcal{F}/L$, $\Delta\rho$, $v_{rms}$ increase quasi linearly with $\zeta$ over the full range.

## 4.4 Summary and outlook

In this section we have looked into an active nematic in situations that are well studied for equilibrium fluids: a wetting layer and a droplet on a flat surface. Using numerical simulations, we have seen that activity can make films unstable. To a certain extent, we could use existing analytical theory to predict the stability under the influence of active stresses[200]. The results matched the simulations fairly well and gave the correct qualitative dependence on the system's parameters. For a stable flat film on a surface, the free-energy contribution to the surface tension can be measured from simulations, but interestingly, the surface tension does not affect the outcome of the simulations and seems to be negligible in the analytical calculations to a good approximation.

Simulation outcomes for the droplet setup are more complex. Droplets are stable for all activities considered and the steady-state shape of a droplet is significantly altered under the influence active stresses. The overall force balance in the steady state is retained by pressure gradients counteracting the active forces over large parts of the interface. Only close to the contact point, where the interface meets the no-slip surface, this force-balance is imperfect and fluid velocities do not vanish. Here, it is a balance between advection and diffusion in the equation for the dynamics of the phase field $\phi$ that keeps up the droplet's steady-state shape. A mechanism deemed important for the droplet shape is the active anchoring effect that becomes stronger with increasing active forces and causes deformations in the interface competing with energetic effects.

However, for the droplet an analytical theory is still lacking. In particular it is unclear, how active forces determine the final shape of the droplet. Comparison to previous analytic works is difficult as different assumptions are used. If different active materials with fundamentally different properites, namely polar active fluids, are modeled[203–206], also different dynamics are observed. In other studies, assumptions on director alignment and contact angles are made[202] which do not match our results. This can be important, because we have seen that the orientation of the director relative to the interface varies along the interface. This occurs especially next to the contact points, where this effect distorts the force balance and leads to steady state flows. Altogether, these studies are not directly applicable to our setup, but of course could serve as inspiration in further investigations.

We would conjecture that interfacial effects in this setup play a key role for the final shape of the droplet. As the relative orientation between director and interface varies along the interface, it is expected that also the energetic component of the surface tension varies. It is already know for equilibrium systems, that this has the interesting consequence of flows from regions with lower to regions with higher surface tension, so-called *Marangony flows*. In addition, active forces tangential to the interface would represent an active contribution to the surface

tension that breaks equilibrium conditions. Surface tension in active systems has been investigated in systems of active Brownian particles and related continuum models[52, 133, 190, 191]. Computational as well as analytical results reveal interesting features of surfaces in this kind of systems. However, these are models for scalar active matter. To my knowledge, no thorough analysis of interfacial effects in nematic active matter has been performed. The active anchoring effect can qualitatively explain the interplay of active forces and the nematic director and help understand why certain configurations are stable or not[112], and could serve as a good starting point for the investigation of surface tension effects. Next to that and the aforementioned works concerned with surface tension in scalar active systems, also recent works on surface tension[209] or wetting[189, 210] in equilibrium systems might be helpful for research in this direction.

However, the film as well as the droplet example in sum reveal another important point: in both cases interface and bulk effects cannot be separated. Distortions from the director at the interface are not strongly damped inside the bulk, but continue into it and cause active stresses and flows that are important for the dynamics of the system. It is, among other factors, the entanglement of interface and bulk dynamics together with the presence of flows caused by active stresses in the steady state which makes biphasic active nematic systems so difficult to describe and understand.

From the computational side, further insight in the droplet problem could be gained by probing the system's reactions to parameters variations, for example the influence of different anchoring conditions on the free energy, the change in the contact angles under explicit implementation of surface energies at the solid wall, the dynamics in contractile systems (i.e. $\zeta < 0$), or the impact of variations of free energy constants. A few preliminary results for varying free energy constants and tumbling parameter $\xi$ are shown in the appendix in section 1.2. To obtain a better resolution in the interesting regions close to the contact points and investigate the role of mass conservation, increasing the amount of active material in the system to obtain a larger droplet might be particularly useful. To get closer to actual physical systems, the setup could also be generalised to three dimensions which would lift topological constraints on the director and flow fields and add the shape of the contact area between nematic phase and solid wall as a new characteristic of the droplet. For three-dimensional systems also more comparable studies are available[202–206].

Despite the fact that we do not have theoretical explanations for all the observations made in this chapter, we still could gain some meaningful insight in the properties of the two-phase active nematic model. As was already known[112], active forces play an important role for the orientation of the director at the interface. We suppose that the interplay between director and interface, potentially together with other interfacial effects, is a key factor also for the steady-state shape of a droplet of active nematic material on a wall. This could motivate more detailed

studies on surface tension in active nematics in the future. Nevertheless, also bulk dynamics and the interplay between both, bulk and interface, probably must be taken into account.

# 5 Intermezzo: cellular systems as active matter

In most situations, cells in multicellular organisms behave quite statically: Once a desired state, called *homeostasis*[211], is reached, e.g. an organ is formed, the constituting cells mostly try to keep up this state. Of course, cell assemblies are not totally static as fluctuations and perpetual cell death and division are always present, but the major goal is to maintain the present configuration and thus cells are often basically immotile.

However, in many situations cells are also actively moving to change their position. This is for example the case in morphogenesis, i.e. in times when the desired final state is not yet reached[212, 213], regeneration after leasion[214], or, as a special but medically important case, cancer development[85]. For this purpose, cells are endowed with various powerful mechanisms that allow them to move in coordination with other cells and their environment.

The basic structure that allows cell motion is the *cytoskeleton*, a network of biopolymers, namely actin filaments and microtubules, that forms the cells' internal structure. Via remodelling of the network and with molecular motors that can create mechanical forces and thereby induce relative motion of filaments, the cytoskeleton can actively change its shape under the consumption of ATP[215–217]. As cells can also couple mechanically to neighbouring cells and surrounding tissue[218, 219], these internal deformations can lead to motion relative to the environment. A key mechanism in this context is internal polarisation that causes the cells to move persistently[220, 221]. This is due to positive feedback mechanisms in the cytoskeletal network: once the network has started to expand into a certain direction, biochemical regulatory mechanisms lead to further expansion in this direction. In physical terms, this is a process of spontaneous symmetry breaking. Changes in orientation happen due to fluctuations or because external factors influence the chemical reactions in the cytoskeleton. Such external factors can be mechanical interactions, but cells can also emit and sense chemical signals which provides another way of communication with the environment and other cells. A special feature is also that cells divide to proliferate and die under certain conditions adding further complexity to the system. The cytoskeleton and extracts from it are themselves important example systems in the context of active matter physics[8, 22, 24, 30, 32, 36, 37, 94]. In the following however, we want to focus on the collective behaviour of actively moving and mutually interacting cells.

Dynamics of cellular systems can be studied *in vivo* as well as *in vitro*. To simplify quantitative measurements, various *in-vitro* assays have been developed where cells can be observed under well-controlled conditions[222]. Due to limitations in microscopic imaging it is often not possible to resolve individual cells and thus ensemble observables are widely used to characterise cellular motion, for example quantities describing the shape of growing cell colonies[223]. Another possibility is to extract flow-fields from time-lapse recordings of microscopy images. This approach is particularly useful for the investigation of two-dimensional systems where cells are grown in a monolayer on a flat substrate. Such systems can be realised using *epithelial cells*, a cell type that forms layers in the body to cover the surfaces of organs, vessels, or inner cavities, but can also be cultivated on artificial surfaces. The technique used to extract velocity fields is called particle image velocimetry (PIV) and was originally developed to analyse flows in hydrodynamics experiments. Microscopy images are divided into subregions and then for each subregion a displacement vector can be calculated by cross-correlating subsequent images: The displacement or velocity field is thus calculated from structural information of the images[224].

One classical setup investigated in this way is the so-called *wound-healing assay* where epithelial cells are seeded in a petri dish but hindered from filling up the full space by a barrier[224–226]. When the epithelium has grown to a certain density, the barrier is removed and the cells invade the empty space just as we let the active nematic invade the capillary in chapter 3. Then, the emerging flow fields and front shapes can be analysed[224, 227]. However, also systems without fronts, where the epithelium is equally spread out, show interesting properties. Velocity statistics are fundamentally different compared to equilibrium materials and above a certain density cells significantly reduce motion, then resembling a glassy system[25–29]. This transition is named the *jamming transition* and has attracted a lot of interest[27, 28, 228–230].

Directions of further research are plenty. One important question are the interactions among cells as well as between cells and the substrate they are cultivated on. From the physics perspective, this means investigation of the corresponding forces and stresses (see e.g. review papers: [226, 231], research articles:[232–238]). Forces actually play an important role. Cells are assumed to be influenced in their migration by the stresses they feel (*phliotaxis*)[239] and the stiffness of the substrate (*durotaxis*)[240]. Two other important mechanism of cell-cell interaction are *contact inhibition of locomotion* and *contact enhancement of locomotion*, that describe how cells change their motility when having contact to other cells[241–243]. Contact inhibition of motion means that cells reduce their motility in such situations while contact enhancement of locomotion is the opposite effect: cells move more when meeting a fellow cell. Which of both phenomena is observed depends on cell type but can also differ when cells meet at different orientations[244, 245].

Interactions of cells and internal polarisation thus make up the fundamental paradigm of collective cellular motion: Cells, under the right circumstances, move persistently due to remodelling of their cytoskeleton. This motion is regulated by the mutual mechanical or chemical interaction of cells as well as external cues provided by the environment[246]. In this, also heterogenties in cell populations can play an important role. Either because different sorts of cells are present that behave differently, for example because they prefer a certain mutual arrangement[212, 247] or because during the experiment, certain cells start expressing different behaviour. An important example of the latter is the emergence of so-called *leader cells* that are observed in setups where cells are to invade free space[70, 155, 248–250]. These leader cells are assumed to invade more eagerly and drag the other cells behind them. What actually makes cells leader cells is one of the present research questions in this context.

Further variation can be brought in by confining cells to geometries of different shapes[67, 68, 71, 74, 251–253]. It is experiments like these that have motivated the study in the following chapter 6.

**Modelling cellular systems** In order to better understand the underlying dynamics, various models have been developed. Overviews over the different model classes can be found in[94, 139, 147, 222, 225]. In general, almost all types of models for active matter presented in chapter 2 have been applied, for example self-propelled particles with attractive potentials[254]. Since we have seen that cellular motion in experiments is often characterised by velocity fields, the application of continuum models seems quite natural[116, 117, 255] and has led to interesting insights. For example it could be shown that stresses regulate the remodelling of the epithelium as in locations of high compressive stresses, cell differentiation or extrusion of dead cells occur more frequently.[35, 256].

A class of models not discussed in chapter 2 are models that regard the epithelium as a coherent active network. These are mainly *vertex models*[147, 257] and *Voronoi models*[147]. In vertex models, cells are considered as polygons that tile the epithelium. The model is then formulated in terms of the vertices of the polygons. Similar to Cellular Potts Models (CPMs) presented in section 2.3, the dynamics of the network is determined by an energy function and optionally a polarisation mechanism. These models were especially successful in describing the general shape and internal organisation of cell sheets and the shapes of constituting cells[91, 247, 258–260]. Active Voronoi models in contrast model the cell centres and the polygons are determined by Voronoi tesselation. Vertex and Voronoi models are also used in the context of the jamming/ unjamming transition[28, 29].

In the same way, Cellular Potts Models and phase field models as described in section 2.3 were developed primarily aiming at cellular systems. In the following chapter 6, we will use a CPM to simulate a sheet of epithelium cells invading into a

bottleneck geometry. Our main objective is the analysis of the spatial arrangement of cells inside the sheet and their individual dynamics. For a study like this, the CPM is highly suitable since it simulates individual cells and keeps description on a fairly general level. The hope is that it thus creates qualitative results that are typical for many cell types. As microscopy techniques progress further, imaging single cells will become easier and such predictions will hopefully be testable more easily.

In general it must be said that cellular systems are of enormous variety and complexity. Different types of cells, of which there are a lot, may behave totally differently and also identical types of cells can adapt their behaviour to the situation they encounter. Our discussion in the introductions about the challenges in modelling, in this case of cellular motion, applies also here: any general model must sideline a lot of aspects to fit the diversity of systems and therefore will probably be unable to make very precise predictions for a chosen type of cells in a chosen situation. Nevertheless such models might help to gain an understanding of certain general key mechanisms. The CPMs, phase-field and vertex models primarily aim in this direction. In contrast, a more specialized model could and would need to be designed when the goal is to make quantitative predictions for specific situations. An example for this are the approaches to detailed modelling of cell-cell interactions in[244] and[245]. Also, again motivations for studying collective behaviour of cells are very different: the detailed description of glassy dynamics is probably more in the interest of physics, while other research topics, for example phliotaxis and durotaxis, might be of higher biological relevance.

# 6 Cellular Potts Model in a bottleneck

*This chapter is based on research I conducted together with Andriy Goychuk and Erwin Frey.*

## 6.1 Introduction

In their natural environments, collectively moving cell assemblies often face obstacles or barriers. Such external constraints hinder free movement and force the cells to squeeze through narrow gaps or move along externally predetermined routes. Examples for such situations are cancer development and morphogenesis[84–86, 226, 261], where cells move as cohorts and are surrounded by other cells and extracellular tissue.

To investigate how such extracellular constraints alter cellular behaviour, idealised *in-vitro* experiments have been set up in environments with different geometries[225]. This has been realised for single cells that squeeze through tight capillaries[262, 263], but also in numerous experiments on collective cellular assemblies in diverse settings like straight 2D troughs[67–69, 71, 74, 252] and 3D tubes[264], winding canals[253], and expanding or narrowing channels[70]. The general question is what phenomenological effects are induced by external confinement and guidance, for example regarding flow behaviour, cell shape, spatial arrangement of cells in the cell sheet, or cell division.

Computational models have been employed to help us gain a better understanding of the essential mechanisms that govern cell behaviour in situations like those described above[147, 265]. The behaviour of cells is governed by numerous complex mechanical and regulatory internal processes as well as chemical and mechanical interaction between cells. Computational models that simulate single cells attempt to reproduce the observed behaviour at small scales, or at least certain aspects of it, by reducing the complex real-world machinery to simpler mechanisms with the aim of capturing the important features of cell behaviour like migration or interaction with other cells. The intention is to construct a minimal functional system that retrospectively justifies the initial guess as to what features were deemed important.

Four types of models for collective cellular dynamics that follow this idea are the so-called Cellular Potts Models (CPM)[140–142], models in which cells are represented as self-propelled interacting particles[155, 266, 267], phase-field models[93,

144–146, 150], and so-called vertex models[91, 247, 258–260]. In the context of cellular assemblies moving in tight channels, self-propelled particle models have been used to investigate straight, converging, and diverging channels[155]. Another approach uses continuum models in which single cells are not resolved. These take into account fundamental symmetries and coarse-grained mesoscopic forces, which provide a larger-scale picture of the system, and they have already been shown to be applicable to cellular systems[35, 116, 117, 147, 268]. Continuum models have also been used to simulate the dynamics of active matter confined to elongated channels[73, 123] and to model invasion of active matter into a narrow straight capillary[1].

In this work, we want to extend previous studies that analysed how confinement in a straight channel affects cellular motion. To that end, we investigate how a cellular sheet adapts to a channel of varying diameter. Similar situations can be expected to arise in real-world scenarios where a migrating cellular cluster is forced to squeeze through a narrower capillary of surrounding tissue.

The paper is organised as follows: In Sec. 6.2, we explain our setup and the main features of our model for simulating the epithelial layer, focusing on properties that are central to our specific study. Presenting the numerical results in Sec. 6.3, we first give a qualitative overview and then analyse the cell sheet's internal spatial order and collective dynamics, as well as the dynamics of individual cells. Finally, we discuss consequences of variations in channel geometry and model parameters before we conclude with a summary and discussion in Sec. 6.4.

## 6.2 Setup and model

We investigate the internal spatial organisation and dynamics of an epithelial cell sheet encountering, traversing, and emerging from a bottleneck, whose geometry is shown in Fig. 6.1A. This setup is intended to be an idealised representation of a capillary-like constriction that cells might encounter in their natural environment. We first let a cellular sheet grow in a reservoir to the left of the channel (not shown in figures) and at $t = 0$ open the channel to initiate invasion. From that point on, we monitor the internal spatial organisation and dynamics of the cellular sheet.

In our computational approach, we use a Cellular Potts Model (CPM) that simulates individual, spatially extended cells and their internal dynamics, as well as their mutual interaction on a two-dimensional plane. This computational model adopts an integrative perspective on high-level cell functionality, including the propensity of cells to establish and maintain cytoskeletal polarities, cell-cell and cell-substrate interactions, as well as a basic notion of cell mechanics.

Models of this kind have successfully in reproduced the cellular dynamics of single cells moving in stripe-shaped environments[269] and on substrates of vary-

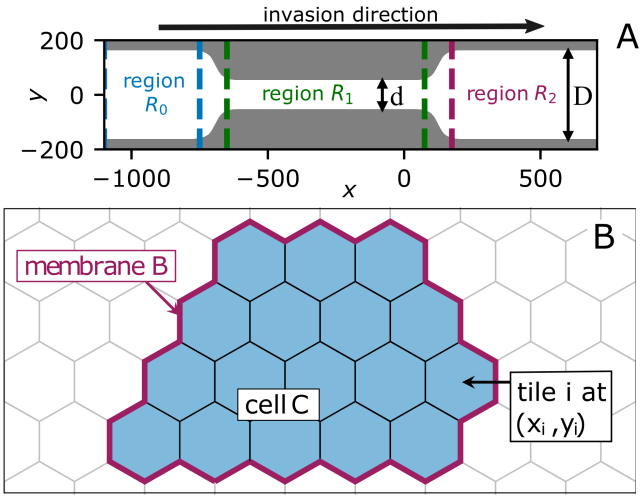


**Figure 6.1** *Simulation setup and model.* (A) Geometry of simulation setup. Cells enter the channel from a reservoir (not shown) on the left. $D$ and $d$ denote the diameters of the wider parts and the narrower part ("bottleneck") of the channel, respectively. Regions $R_0$, $R_1$, and $R_2$ denote the space before, within, and beyond the bottleneck, respectively. In this work, we will analyse these regions separately to investigate the influence of the bottleneck on cell motion. (B) Sketch illustrating the model. On the hexagonal grid, a cell C can occupy several tiles (marked blue). The cell boundary B (violet) is then formed by their outermost edges. Movement of cells is realised by occupying and abandoning tiles, the dynamics of all cells is governed by a kinetic Monte-Carlo algorithm.

ing stiffness,[270] as well as small numbers of cells in circular[79] or channel-shaped[271] environments, and cell sheets of 2000+ cells expanding into free space[142, 272]. We therefore would argue that the CPM, despite its simple structure, captures essential features of the complex mechanisms that govern real-world epithelial cell dynamics, and permit general predictions of the behaviour of cells under *in-vitro* conditions.

Specifically, we use the model and implementation described in Ref. [142] with slight modifications in the cell-division mechanism (for details see section 2.1 of the appendix). Figure 6.1B illustrates how cells are represented in the model. It is a cellular-automaton-type model, where space is discretised into a hexagonal tiling. A cell occupies several tiles in the plane that reflect the contact area of the cell with the surface and every tile can be occupied by only one cell. The membrane of the cell is formed by the perimeter of the tiles that it occupies. By occupying new tiles or leaving previously occupied ones, cells can change shape and size and, via a combination of several events, migrate on the substrate. The dynamics is governed by a kinetic Monte-Carlo scheme which aims to minimise a global effective free energy. This free energy depends on the collective arrangement of cells, as well as the state of their internal variables, and changes over time as a consequence of the

non-equilibrium processes that mimic internal processes of the cells. Among the mechanisms that contribute to the free energy, we will here focus on those that are most relevant for our study:

- A *preferred cell area and membrane length (circumference)*: A term $\mathcal{H}_{\text{cont}} = \kappa_A A^2 + \kappa_P P^2$ for every cell, which restrains membrane and cortex deformations. Here, $\kappa_A$ is the area stiffness, $\kappa_P$ the perimeter stiffness. Together with substrate adhesion, which favours larger cells (as explained below), this leads to a preferred cell size.

- *Cell-cell adhesion* and *cell-cell dissipation*: Two cells occupying neighbouring tiles obtain an energy benefit that reflects the formation of intercellular bonds (cell-cell adhesion), while loss of such mutual contacts and the associated breaking of bonds is energetically penalised (cell-cell dissipation). These effects combined lead to coherent cell structures in the simulation and thus ensure the cohesion of the cell sheet. Dissipation also leads to "viscosity-like" effects.

- *Interaction with the underlying substrate regulated by an internal polarisation field*: The cytoskeleton of the cell, which is regulated by networks of signalling proteins[219, 273], adheres to the substrate via integrins and determines the tendency of a cell to form protrusions or to retract. The contribution to the Hamiltonian that is associated with cell shape, $\mathcal{H}_{\text{cont}}$ is purely contractile, and thus would, by itself, lead to detachment of cells from the substrate thereby favouring cells with zero contact area. To counteract this cell contractility and detachment, we use an effective surface adhesion energy, the scalar polarisation field $\epsilon$. This polarisation field serves as a proxy for the ability of cells to form focal adhesions and to facilitate polymerisation of the actin cytoskeleton. A higher value of the polarisation field can be interpreted as a stronger local adhesion, therefore counteracting retractions and facilitating protrusions. Similarly, a low value of the polarisation field means that it cannot locally balance out cell contractility, so that the cell will retract (i.e. detach from the substrate). In turn, we represent the signalling networks that regulate the formation of focal adhesions and polymerisation of the cytoskeleton via two prototypic feedback loops: in the vicinity of protrusions (retractions) we increase (decrease) the polarisation field. It is this feedback loop that prevents the system from relaxing to a time-independent global minimum-energy state and induces an internal polarisation and persistent motion of cells. The interplay of the polarisation field and cell-cell adhesion results in collectively migrating, coherent patches of cells.

- *Internal cell-cycle*: To achieve invasion of cells into the capillary, proliferation of cells needs to be implemented. After a growth period in which $\kappa_A$ and $\kappa_P$ are

continuously adapted such that the preferred size of the cell doubles over the full period, the cell enters a division phase. The polarisation field uniformly drops to zero and at the end the cell splits into two identical daughter cells. After division, the daughter cells are in a quiescent state, i.e. there is no growth. After a certain time, cells are ready to enter the growth phase again, but do so only if the cell size, via fluctuations, exceeds a certain threshold. The latter effect ensures that growth is halted above a certain cell density. In our simulations, cell division is limited to the reservoir, as we assume that the entire trajectory in our system occurs on timescales in which cell division can be neglected.

For a complete listing of the parameters and their values used see appendix section 2.1.

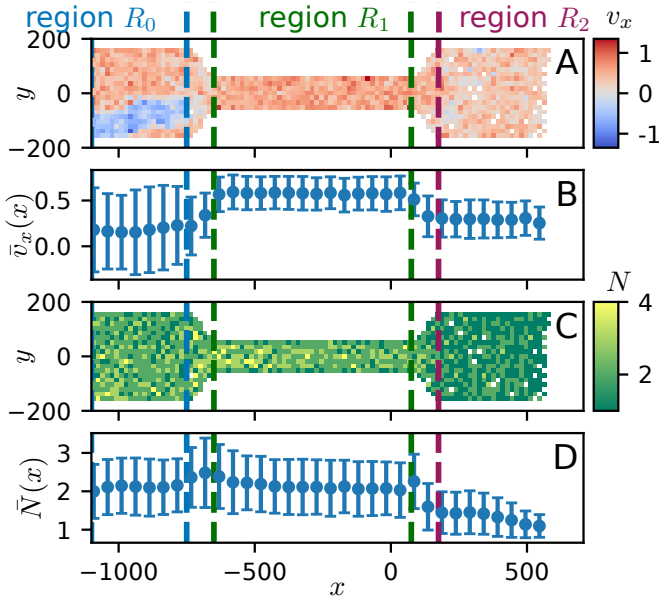


**Figure 6.2** *Example of a simulation in a constricted channel. Bottleneck diameter d corresponds to about 10 cells, diameter of the broad regions is $D = 3d$, length of bottleneck $\approx 5d$.* (A) Heatmap showing cell velocities along the channel axis $v_x(x, y)$ at a late time-point in the simulation. (B) $v_x(x, y)$ averaged over $y$ and time. At the average velocity of $\sim 0.5$ in the narrow region $R_1$, a cell takes $\sim 30$ time steps to cover the distance corresponding to one cell diameter. (C) Heatmap showing the density distribution $N(x, y)$ at a late time-point in the simulation. (D) $N(x, y)$ averaged over $y$ and time. Observables in B and D show higher values in region $R_1$. Error bars in B and D show the standard deviation.

## 6.3 Results

### 6.3.1 Velocity and density profiles

The bottleneck with its smaller diameter $d$ hinders free homogeneous expansion of the cell sheet in the direction of the channel axis. As illustrated in the example in Fig. 6.2, the constriction affects cell velocities as well as the number density. In this example, $D = 3d$, where $d$ corresponds to roughly the width of 10 cells. The length of the bottleneck is $\approx 5d$.

The forward velocity $v_x(x, y)$ (Fig. 6.2A,B) increases in the narrow region and drops again following passage through the constriction to a value larger than the velocity at the entrance. This disparity of velocities is explained by clusters of cells that are forced to retreat owing to the congestion caused by the constriction - a phenomenon we call "backflow" - which leads to a reduction in the average $\bar{v}_x(x)$ and an increase in the standard deviation (Fig. 6.2A) . This is in contrast to what would be observed for laminar flow of an incompressible fluid where the fact that the channel width is the same on both sides of the narrow region would lead to identical values of $\bar{v}_x(x)$[39].

In comparison, the number density $N(x, y)$ of cells (Fig. 6.2C,D) is roughly constant in the regions $R_0$ (ahead of the bottleneck) and $R_1$ (inside the bottleneck), but shows a slight rise right in front of the funnel and drops considerably upon leaving the bottleneck, i.e. when the channel widens again. The rise points to an accumulation and corresponding compression of cells in the funnel. Interestingly, the higher density of cells is not “translated” into the narrow channel section, but causes cells to change direction, thus causing the backflow. In contrast, the widening at the end of the channel allows expansion of the epithelial sheet, leading to a lower density, or larger cell areas, and reduced velocity in the region beyond the bottleneck. Thus, both findings show that cells do not pass the narrow part smoothly, like a laminar fluid would do, but that the rightwards motion of the cells is distorted and the flow behaviour of the cell sheet clearly shows properties of a compressible fluid. In general, it should also be noted that fluctuations in both observables are quite high, as the standard deviation is of the same order of magnitude as the mean values (Fig. 6.2B,D).

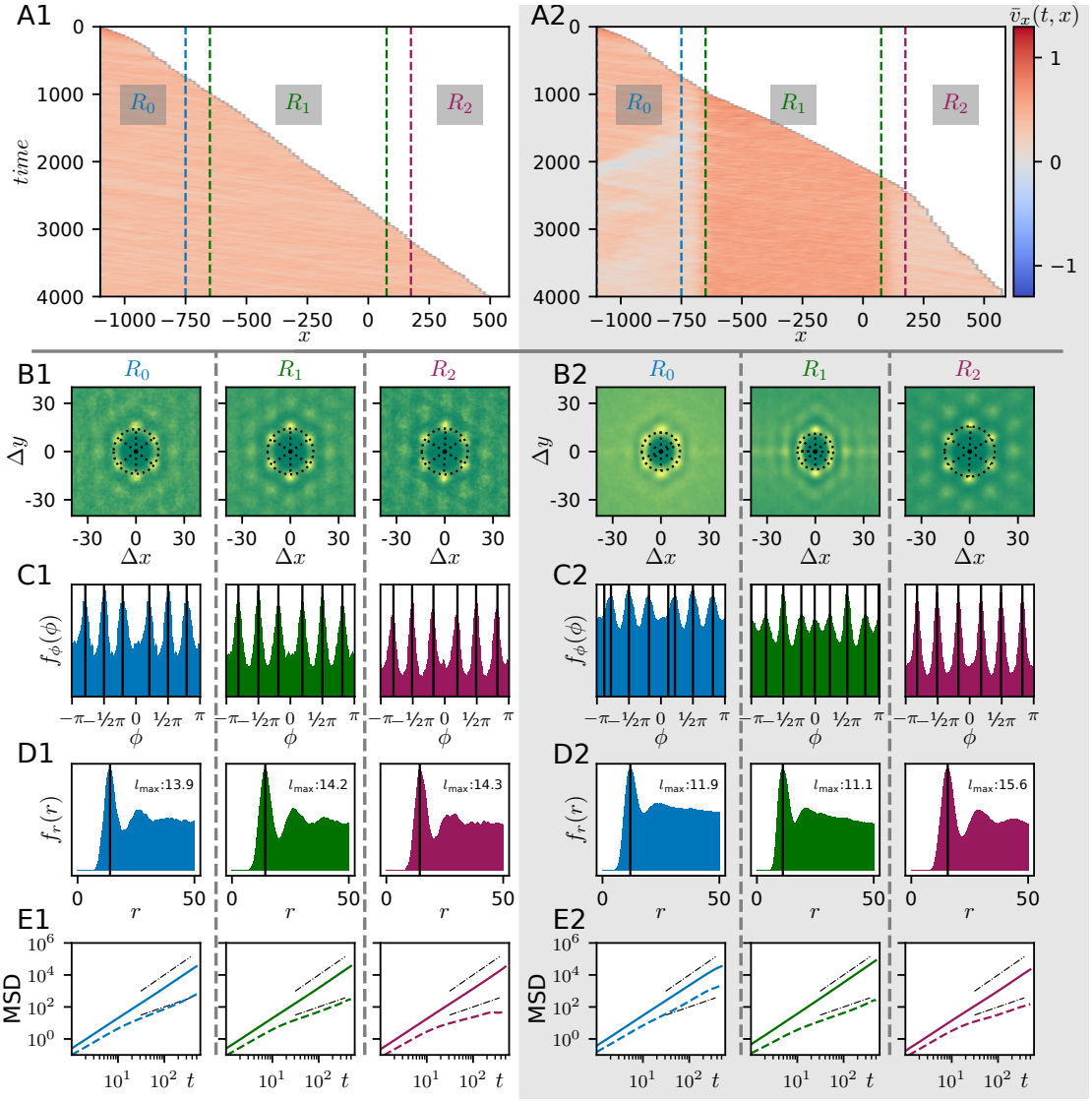


**Figure 6.3** *Comparison of cellular order and dynamics between a homogeneous and a constricted channel, channel parameters as in Fig. 6.2.* Left (panels X1): homogeneous channel, right (panels X2): channel with bottleneck. (A) Kymograph of the velocity in channel direction, $v_x(t,x)$. Dashed lines indicate transition regions in A2, and are indicated for comparison in A1. Two features of cell motion in the bottleneck configuration (on the right) are clearly visible: the higher velocity in region $R_1$ (for definition of regions see panel A and Fig. 6.1) and the backwards motion of cells in front of the bottleneck. Both are already discernible in Fig. 6.2A,B. (B-D) Radial distribution functions (RDF) for the different regions of the channel, as defined in the main text. The six regularly spaced peaks around the centre for the straight channel in B1 reflect the disposition of cells on a hexagonal lattice, while the more washed-out patterns in regions $R_0$ and $R_1$ in B2 show that spatial constraints prevent the cells from adopting that arrangement.

**Figure 6.3** ***(ctd. from previous page)*** For more detailed analysis, the RDF is integrated over the radius (panels C) or the polar angle (panels D). Vertical black lines in C and dashed radial lines in B mark maxima in the marginalised angular distribution function $f_\phi(\phi)$ as detected by our algorithm (for details see 2.2 in the appendix). Largely unperturbed hexagonal order is reflected by six pronounced maxima, while additional peaks appear at $-\pi/\pi$ and 0 in region $R_1$. The vertical black lines in D and the dashed circle in B mark the respective maxima of the marginalised radial distribution functions $f_r(r)$ which give the typical nearest-neighbour distances. (E) Mean-squared displacement (MSD, solid line) of cells and cage-relative mean-squared displacement (CR-MSD, dashed line). Black dashed-dotted lines show linear and quadratic scaling, respectively. In contrast to the ballistic MSD, the CR-MSD clearly scales with a lower, but still finite exponent. This shows that cells, unlike particles in a true solid, are not caged, but behave more like diffusive particles suspended in a liquid. Such a combination of properties that is typical for glasses and viscoelastic materials. As an exception, the CR-MSD is superlinear in region $R_0$ of the bottleneck channel. Here the backflow leads to enhanced relative motion of cells.

### 6.3.2 Spatial organisation

To further assess the effect of the bottleneck (Fig. 6.1A) on the spatial organisation of cellular tissue, we measured the radial distribution function (RDF) in our simulations. The RDF is defined as

$$g(\mathbf{r}) \propto \left\langle \sum_{\alpha \neq \beta} \delta\left(\mathbf{r} - \mathbf{r}_\alpha + \mathbf{r}_\beta\right) \right\rangle_t . \tag{6.1}$$

The double sum in Eq. (6.1) runs over all pairs of cells in the area under observation, with $\mathbf{r}_\alpha, \mathbf{r}_\beta$ being the positions of the cells[38] while the angular brackets indicate a time average which is taken late in the simulation such that there are cells in all channel regions. In essence, this yields a histogram of the distribution of mutual particle-particle distances $\mathbf{r}$ that characterises the close-range order of the cells. To analyse the differences between the three regions of the bottleneck setup, we calculate the RDF separately for each.

Figure 6.3 shows a comparison between a system with a uniform channel width $D$ (X1) and a channel geometry which also contains a bottleneck of diameter $d$ (X2). In the absence of a bottleneck, the RDF exhibits a set of six fairly pronounced peaks regularly spaced on a circle around the centre. Note that even higher order peaks are clearly visible, indicating a finite range of lattice-like order with hexagonal symmetry. This is reminiscent of a similar degree of ordering observed in two-dimensional colloidal systems[274]. The appearance of such sixfold coordination in cellular sheets is consistent with previous studies, as it was observed very early *in vivo*[275],

as well as more recently in Voronoi[276] and vertex[277] models. It can also be motivated from purely topological considerations[278].

In contrast to the fairly regular and homogeneous patterns that we observed in the straight channel, the degree of ordering shows significant spatial variation across the different regions in the presence of a narrower central section. In front of the bottleneck (left panel in B2), the six peaks are blurred in the angular direction and there are no further peaks beyond the closest six. Both observations hint at a distortion of the regular hexagonal order. Inside the bottleneck (centre panel in B2), two additional peaks appear at $\Delta y = 0$ which come from neighbours before and after the cell along the channel axis. We suppose that this longer-ranged ordering is due to the fact that the closer channel boundaries force cells towards the centre, and thus hinder the free development of the hexagonal pattern in lateral direction. To the right of the bottleneck, the ordering is fairly similar to that observed for systems with a uniform channel width. This is because, as in the straight channel, cells can invade the free space beyond the bottleneck without hindrance.

In order to bring out the characteristic features of the RDF more clearly, we look at the marginalised angular distribution $f_\phi(\phi)$ and the marginalised radial distribution $f_r(r)$. These represent the integral over the radius and over the polar angle, respectively (for details see appendix section 2.2). $f_\phi(\phi)$ allows one to compare number and arrangement of the maxima in the RDF, $f_r(r)$ can be used to determine their typical distance from the centre. The results are shown in Fig.6.3C,D.

In the cases where the radial distribution function $g(\mathbf{r})$ shows six distinct peaks, there are also distinct peaks in $f_\phi(\phi)$. In contrast, when the RDF is more blurred, then the peaks in $f_\phi(\phi)$ are also less pronounced. This is especially prominent in the regions $R_0$ and $R_1$ for the channel with a bottleneck. In all cases, however, the radial distribution $f_r(r)$ shows a distinct peak at position $l_{\max}$ indicating the typical nearest-neighbour distance. Additional maxima are due to second and further nearest-neighbours. While this inter-cell distance is more or less constant along a straight channel, under the influence of the bottleneck geometry it is considerably larger in region $R_2$ beyond the bottleneck compared to the other regions $R_0$ and $R_1$. These observations from the marginalised distributions $f_\phi(\phi)$ and $f_r(r)$ support the following conclusions: cells are compressed ahead of the funnel and in the narrow region, which translates into a reduced neighbour-neighbour distance, but also induces asymmetries in the hexagonal arrangement.

### 6.3.3 Collective cell dynamics

In order to assess the dynamics of the cells, we monitored both their collective dynamics (Fig. 6.3A) as well as the dynamics of individual cells (Fig. 6.3E).

For the collective dynamics, we follow the time evolution of the mean velocity-profile in channel direction $\bar{v}_x(t,x)$ as it is shown in the kymographs in Fig. 6.3A.

Here, the velocity profile for one instant in time is plotted along the horizontal axis using a colour code, and time evolution thus proceeds along the vertical axis from top to bottom. Locations where there are no cells appear white, so that the trajectory of the advancing front of the cell sheet appears as the line that separates the white from the red area. Figure 6.3A shows that the velocity field is more homogeneous in the straight channel, as there is no backflow or regional velocity increase, and only slight wave-like modulations appear. These modulations are also present in the case with a bottleneck, but in general appear only as slight variations compared to the other effects, such as backflow and velocity increase in the narrow region. Also, we note that backflow appears with some delay after the first cells have passed through the funnel and begun to invade the narrow region.

To characterise the dynamics beyond the mean velocity profile, we next have a look at the second moment of the cell trajectories. A typical measure for the second moment is the mean squared-displacement (MSD), which tells us about the movements of the cells relative to the laboratory frame, i.e. the surrounding confinement, but does not inform us how particles move relative to each other. To quantify this relative motion, we also consider the so-called cage-relative MSD (CR-MSD). In this quantity, the mean trajectories of all neighbours of a cell are subtracted from the cell's trajectory. Then, the MSD is calculated from this relative trajectory[279, 280] (details in section 2.2 of the appendix). In two-dimensional colloidal systems, the CR-MSD, due to its local nature and hence independence from large-scale (Mermin-Wagner) fluctuations, can be used to discern solid and fluid states with more contrast than the ordinary MSD. In a solid, single particles are "caged", i.e. trapped between their neighbours and thus the CR-MSD is bounded. In contrast, in a fluid, the CR-MSD would be unbounded and would steadily increase with time[280].

In our system, the "ordinary" MSD (solid lines in Fig. 6.3E) scales with $t^2$, reflecting the polarised and coordinated motion of the particles through the channel. The CR-MSD (dashed lines in Fig. 6.3E) in comparison shows a reduced scaling as overall rightwards motion is subtracted, but is not bounded. This indicates that cells are not trapped between neighbours, but that instead there is relative motion between cells inside the sheet and change of neighbours. This dynamic feature, combined with regular hexagonal order, is typical for glass-like systems[280]. Such parallels between glasses and cellular systems have previously been reported in various experimental and theoretical studies.[25–29]

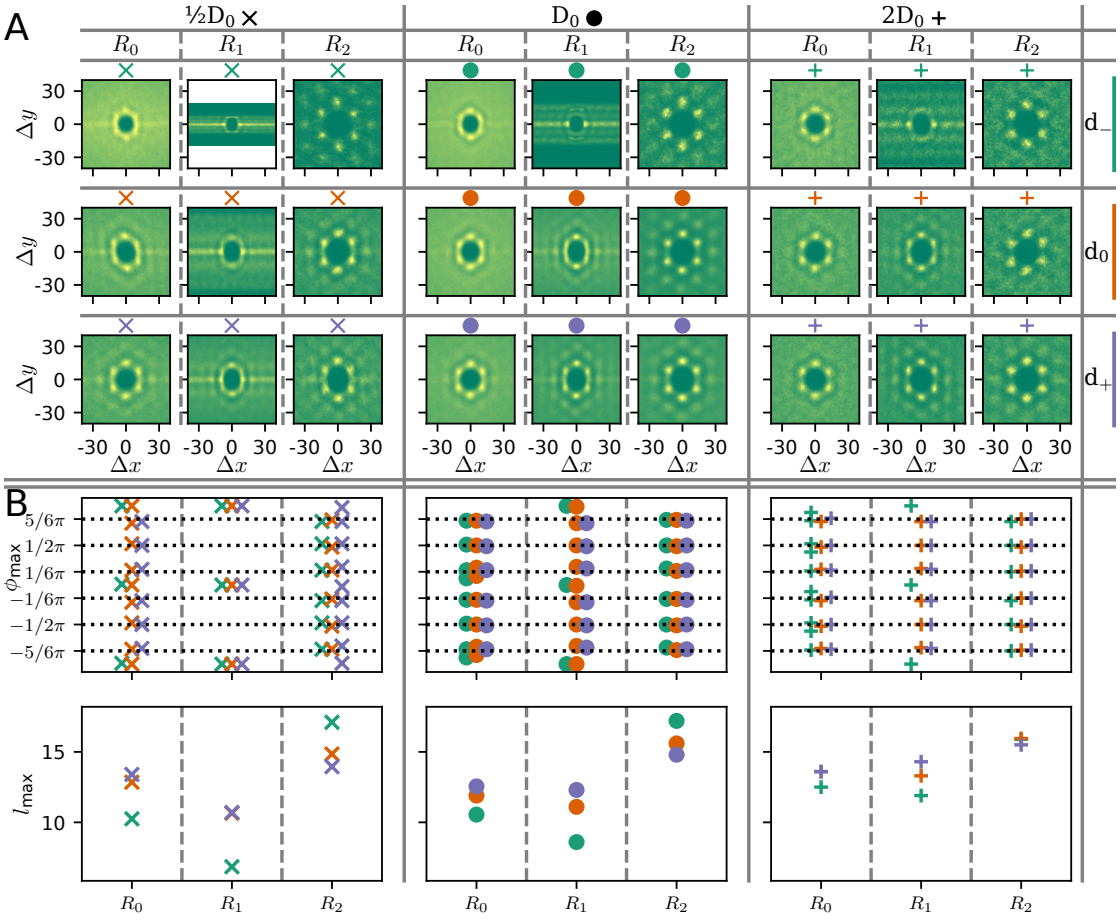


**Figure 6.4** *Comparison of cellular order in constricted channels of varying width.* (A) Radial distribution functions (RDF) for different diameters $D$ of broader channel sections and $d$ of constricted channel section (for definition of regions see Fig. 6.2). From left to right: increase in $D$ ($\frac{1}{2}D_0, D_0, 2D_0$), from top to bottom: increase in $d$ relative to $D$ ($d_- \equiv \frac{1}{12}D, d_0 \equiv \frac{1}{3}D, d_+ \equiv \frac{1}{2}D$). The larger the diameter of the region under consideration, the more the RDF resembles a regular hexagonal configuration and the less order in region $R_0$, upstream of the constriction, is influenced by the bottleneck. For white areas there is no data due to the very narrow channel. (B) Results of quantitative evaluation of the results in panel (A). The positions of the markers along the horizontal axis of the respective plots correspond to the regions indicated. Varying marker forms indicate varying $D$, varying colors indicate variations in $d$ as the small symbols above the plots in part A show. In both panels, plots show results for increasing $D$ from left to right. *Upper panel*: Positions of maxima in the marginalised angular distribution function obtained from radial integration of the RDF (compare part C of Fig. 6.3, and appendix Figure 9). For situations similar to those in region $R_1$ for $(D_0, d_0)$ or $(\frac{1}{2}D_0, d_0)$, the detectability of the additional maxima depends on the parameters chosen for the maxima detection algorithm (see section 2.2 in the appendix), but still reflects the influence of the greater proximity of the walls.

**Figure 6.4** ***(ctd. from previous page)*** *Lower panel*: Positions of the maxima in the marginalised radial distribution function obtained from the angular integral of the RDF. As shown in panel D of Fig. 6.3, angular integration of the RDF leads to a distribution whose first peak shows the typical nearest-neighbour distance. Variation across regions is the same as that across parameter combinations except for largest $(D, d)$. (leftmost plot: violet cross on top of the orange cross for region $R_1$, same for the + in $R_0$ in the rightmost plot. Also there in $R_2$, the orange + is on top of the green one.)

### 6.3.4 Varying channel widths

After learning how the presence of a bottleneck affects spatial organisation and spatio-temporal dynamics of cell sheets, we next ask how the observed effects depend on the exact channel geometry. We start by varying the values for the diameters $D$ and $d$ for broad and narrow channel regions, respectively.

In Fig. 6.4, we compare the spatial organisation of the cellular aggregate under variation of $D \in \{\frac{1}{2}D_0, D_0, 2D_0\}$ and relative to that $d \in \{d_- \equiv \frac{1}{12}D, d_0 \equiv \frac{1}{3}D, d_+ \equiv \frac{1}{2}D\}$, where $(D_0, d_0)$ refers to the parameter combination studied in the previous sections. Comparing the results across all combinations of these parameters, the following general observations can be made. In region $R_2$ (behind the bottleneck), there is pronounced hexagonal order in all cases. In contrast, in the other regions the degree of spatial ordering depends on the absolute and relative magnitude of the width of the broader sections $D$ and the bottleneck $d$.

On the whole, there is a tendency that the larger the diameters $D$ or $d$, the lower the perturbations of the spatial order, i.e. the closer the ordering is to a regular hexagonal configuration. We attribute this to the fact that for smaller $D$ and bottleneck diameter $d$, the bottleneck poses a greater hindrance to free movement of cells. For example, the tight bottleneck $d_-$ corresponds to the width of 2-3 cells for $D = D_0$. Thus, for extreme constrictions $d_-$, cells are forced into a single-file-like configuration, as the angular locations of the RDF's peaks in the upper panel of Fig. 6.4B indicate. Analogously, the lower panel of Fig. 6.4B shows that for smaller $d$, the typical distance between the cells, $l_{\max}$, drops in region $R_1$ indicating a higher cell density. For region $R_0$ maxima in the RDF are smeared out in Fig. 6.4A. That indicates distorted hexagonal order in this region (see also appendix Fig. 9). These observations show that a bottleneck diameter $d$ that permits passage only to a few cells in parallel qualitatively changes spatial organisation inside the bottleneck.

We also analysed how the dynamics of cells is affected by changes in the geometry of the confinement; see the MSD and CR-MSD shown in Figure 10 in the appendix and the corresponding scaling-analysis in Fig. 6.5. Beyond the bottleneck (region $R_2$), where as we have seen cellular organisation is hexagonal and cell density is minimal, the MSD indicates ballistic cell movement, while the CR-MSDs' scaling

exponent is significantly reduced and hints at diffusive motion of cells relative to their neighbours. This is the same result as obtained for a straight channel without a funnel (see Figs. 11-15 in the appendix). In contrast, in the spatial domain ahead of the bottleneck (region $R_0$), backflow and congestion effects lead to a distinct scaling of the MSDs: especially for smaller diameter $D$ of the broader section, ballistic motion is inhibited. At the same time, relative motion as measured by the CR-MSD is superdiffusive and scales comparably to the ordinary MSD. Together, these derivations reflect less directed movement, but enhanced mixing of the cells.

Finally, inside the bottleneck (region $R_1$), the CR-MSD in general scales with a smaller exponent than the ballistic ordinary MSD, but is still super-diffusive. This again indicates perturbation of local cellular order there. The configuration of smallest diameters, with a constant CR-MSD, represents an exception. As the bottleneck's diameter in this case corresponds to only one or two cell diameters, cells are in a locked-in configuration as soon as they enter the narrow part so that movement relative to neighbours is bounded. In the context of thermal colloids, a similar effect is referred to as "single-file diffusion".[281]

In summary, we observe that the narrow funnel forces cells to adopt a different arrangement. This results in different dynamics, not only inside the bottleneck, but also in the region ahead of it.

### 6.3.5 Varying the diameter gradient in the funnel region

Because of the large influence of the funnel, i.e. the transition region between wider and narrower parts, has on the collective order and dynamics of the cells, we also considered channels where this transition is smoother; in other words, the funnel is longer. In Fig. 6.6A, the velocity in channel direction $v_x(\mathbf{r}, t)$ is compared for both cases. Velocities are higher for the more slender geometry in the region $R_0$ in front of the bottleneck, but very similar in the other areas. This indicates that backflow is considerably reduced (see also Figs. 16, 17 in the appendix) and that transport along the channel is enhanced. These findings are in line with the results for the scaling of the MSDs (Fig. 6.6B and appendix Figs. 19,20): While in general the results are similar, in region $R_0$ the ordinary MSD's scaling exponent is closer to two for the slender geometry. In contrast, the exponents for the CR-MSD are smaller in regions $R_0$ and $R_1$, corresponding to reduced mixing of cells and more stable configurations. Not much difference can be observed in the positions of the maxima in the angular distribution of the RDF $f_\phi(\phi)$ (Fig. 6.6C and Figure 18 in the appendix), while the typical nearest-neighbour distance $l_{\max}$ is lower for the slender geometry in regions $R_1$ and $R_2$, i.e. within and beyond the bottleneck. These findings for the MSDs and the spatial organisation of cells are in line with the observation of a reduced backflow ahead of the channel's narrow section, which allows cells to squeeze through the bottleneck more efficiently. All in all, the more

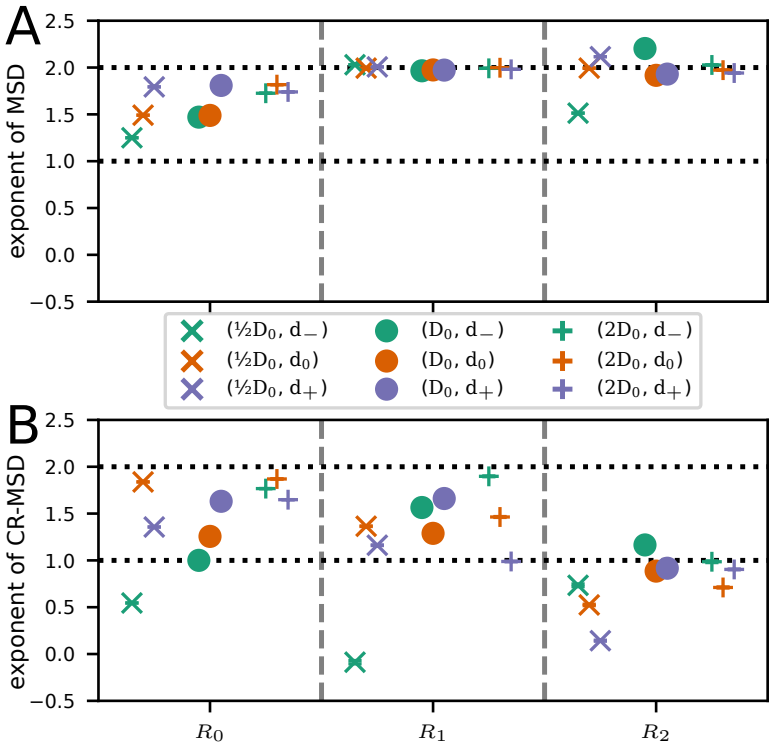


**Figure 6.5** *Comparison of MSDs in constricted channels of varying width.* (A) Exponent from monomial fit to the MSD for same parameter configurations as in Fig. 6.4, depicted separately for different bottleneck diameters $d$ and regions $R_0$, $R_1$, and $R_2$. Except for the very narrow configuration (blue diagonal crosses), the MSD reflects the ballistic motion of the polarised cells in regions $R_1$ and $R_2$. In region $R_0$, congestion at the bottleneck entrance leads to a reduced exponent. (B) Corresponding exponents from monomial fits to the late CR-MSD (for definitions and fitting procedure see appendix section 2.2). Compared to the ordinary MSD in A, the exponents are reduced in regions $R_1$ and $R_2$, indicating reduced relative motion and thus coordinated motion of cells.

slender channel entry allows cells to stack more compactly and stably in the narrow region, and thus facilitates higher transport through the channel, which also leads to less backflow and congestion.

In addition to variations in channel geometry, the system's behaviour can be changed by variation of parameters. In general, the influence of parameters on the dynamics of single cells and collectives in the CPM is examined in detail in Ref. [142]. In the context of our study, cell-cell adhesion has an especially interesting effect. Higher cell-cell adhesion energies cause cells to follow their neighbours more eagerly at the edge of the epithelial sheet. This leads to an increase in mean cell velocities and densities and thus facilitates faster invasion (see section 2.1.4 in the appendix).

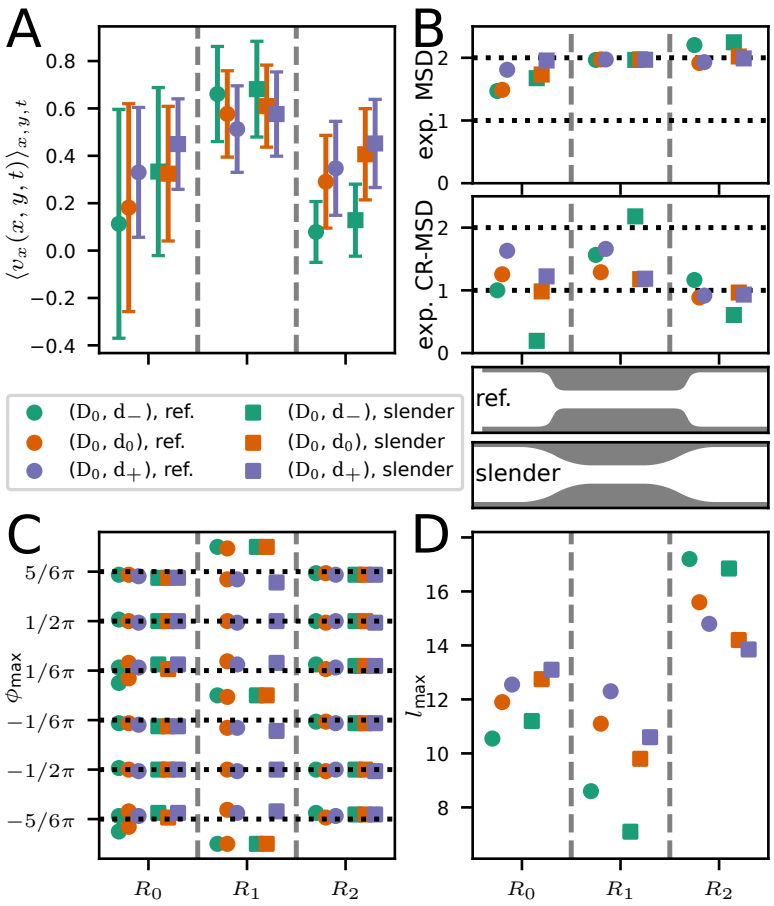


**Figure 6.6** *Comparison of internal organisation and dynamics for different designs of the channel entrance and exit.* The reference design has sharper transitions while these are less abrupt for the "slender" geometry, as the sketches between panels B and D illustrate. (A) Average velocity in channel-axis direction in the three different regions. The higher values in region $R_0$ reflect smoother transitions due to the reduced backflow. (B) Comparison of scaling of MSDs. The ordinary MSD (upper panel) scales very similarly for both, the CR-MSD's exponent is generally lower for the slender geometry, which points to a more regular dynamics reduced relative motion of cells. (C) Angles at which maxima in the RDF appear. Results are very similar: the difference for $(D_0, d_0)$ is attributable to the non-linear character of the maxima detection rather than a real difference in the RDF.

**Figure 6.6** ***(ctd. from previous page)*** (D) Typical distance of maxima in the RDF from the centre. For the same values for $(D, d)$, the slender geometry leads to larger distances, i.e. lower cell densities, in region $R_0$ and higher densities, or smaller distances, in the other regions. This is compatible with the observation that the slender geometry yields less congestion at the entrance and facilitates a denser packing inside the bottleneck.

## 6.4 Conclusions

In this work, we have used computer simulations of a Cellular Potts Model (CPM) which emulates individual cells that exhibit internal polarisation and pairwise, as well as cell-substrate, interactions. We aimed at investigating the influence of a bottleneck channel on an advancing cellular monolayer. To this end, we compared the local spatial organisation of the cellular agglomerate and the collective as well as individual dynamics of cells ahead of, within and beyond the bottleneck across varying geometries. The radial distribution function, the mean velocity of cells in the direction of the channel axis, and the scaling of the cells' mean-squared displacement served us as the corresponding observables.

While cells in an unconstricted channel tend to organise in sixfold-coordinated hexagonal structures and move along the channel with only minor variations in speed and density, the presence of a bottleneck leads to accumulation and reflux of cells near the entrance to the narrow part of the channel, and to distortions of hexagonal order. This effect strongly depends on the relative diameters of the broader and tighter channel sections as well as the design of the transition region in between: The larger the dimensions of the geometry, the less effect on order and dynamics in the cell sheet, while more "streamlined" transitions from broad to narrow facilitate a tighter packing of cells in the bottleneck and hence reduce backflow and pile-up at the bottleneck entrance. These effects, especially on the spatial organisation of cells in the interior of the epithelial sheet, are particularly strong when bottleneck dimensions approach the diameter of only a few cells.

From the physics perspective, the cells show interesting collective properties. On the one hand, we observe features reminiscent of a compressible fluid: increase in density and flow-velocity in the narrow part of the channel while the CR-MSD shows that single particles are not caged completely. On the other hand, there is short-range hexagonal order, which is a typical attribute of solids. The cell sheet thus displays features of both solids and fluids, as it represents a collective composed of ballistically moving agents. In accordance with previous studies, it thus behaves like a glass[25–29, 280] that oozes through down the channel. These collective properties are an emergent phenomenon of the interaction of our model cells via cell-cell adhesion which leads to strong coherence in the monolayer and dictate its properties.

The focus of our work lies on the internal structure and single-cell dynamics inside the sheet and how it is influenced by a bottleneck. Previous works, both experimental[67–71, 74, 252, 253] and numerical[1, 155], have concentrated on velocity and density fields or the shape of the invasion front in channels of constant[1, 67–71, 74, 155, 252, 253] or linearly changing[70, 155] diameter. In many of these studies strong density fluctuations in the channel are reported, a feature that our model did not reproduce. Additional intercellular coupling mechanisms, possibly of the polarisation field, may be required to reproduce this phenomenon.

From the biologist's point of view, under the assumption that our simplistic model captures the system's essential properties, our observations provide information on how an epithelial cell-sheet might react when confronted with physically constricting environments, for example during cancer metastasis or morphogenesis[86, 282]. It would be interesting to see if our results can be reproduced in laboratory experiments. As our analyses heavily rely on positional data of cell centres, potential experiments to test our predictions need to be able to identify and track individual cells or nuclei. Under a more general perspective, the work presented here provides an additional test case on the question of whether the CPM, despite its relatively simple structure, is specific enough to capture variations in the behaviour of cells under varying experimental conditions and can therefore serve as a useful tool for the understanding of cellular dynamics.

In addition, the versatile nature of our model makes it readily adaptable to reflect more closely the conditions of certain experimental systems that for example use a particular type of cells, substrate or channel geometry. This can be achieved not only by variation of parameters, but also by further modifications, such as the use of a viscoelastic substrate[270], additional interaction mechanisms, or different confining geometries. Also more detailed models for the internal dynamics could be introduced. For example, replacing the scalar polarisation field with a polar or nematic field could provide a means of mimicking the symmetry properties of the stress fibres in the cytoskeleton and the resulting anisotropic tensions.

Note also that there is no "genetic" component to the model, as all cells behave identically. This in particular excludes the possibility of investigating the interplay of distinct cell types, for example the consequences of differential adhesion[212, 247] where cell-cell interactions differ according to cell type. Results of a first simulation implementing that are shown in appendix section 2.4. It also does not allow for the emulation of leader cells, which are cells that more aggressively invade empty spaces and drag other cells with them. This effect has been investigated thoroughly in experiments as well as numerical studies[70, 155, 248, 250, 283] and leader cells are assumed to play an important role in cell migration. As such, the implementation of different cell types would increase its versatility even more and allow for the investigation of additional biologically relevant phenomena.

# 7 Conclusions

In this thesis, we have looked into different computational case studies for active matter under confinement with a focus on growing systems which expand into channel-like geometries. For this purpose, we have used two different computational models for active systems.

In chapter 3, we employed a continuum model for studying the growth of an active nematic into a straight channel filled with isotropic fluid. Two different phases are represented using a phase-field model that is coupled to the Navier-Stokes-like dynamics of a background fluid. A Cahn-Hilliard-type free energy ensures phase separation. In addition, a nematic order-field is coupled to this phase-field such that in one phase, the nematic phase, nematic order is maximal while in the other phase there is no nematic order and hence this phase represents an isotropic fluid. Activity is introduced via an active stress term in the momentum equation for the fluid that corresponds to microscopic force dipoles that are aligned with the orientation of nematic order and whose strength is proportional to the degree of nematic order. This effectively caused finite forces on the fluid at the phase boundaries and in regions of the nematic phase where the order is inhomogeneous. We started with a cluster of active material in a large reservoir at the entrance to the channel. Growth was realised by adding source terms for the nematic component of the phase field in the reservoir which causes the nematic to invade the channel. Our main finding was that, depending on the strength of the active forces, there are three different modes of invasion, each with distinct front shapes and flow fields, that also influence the overall invasion speed. Below a certain threshold in activity, there are no flows at all, invasion into the channel is only diffusive. The first mode of non-zero flow that can be sustained above the activity threshold is leading upwards the channel on one side and back downwards on the other. With the appearance of flows, the nematic phase progresses into the channel significantly faster. For even higher activities, more complex, but still circular, flows develop. This is accompanied with smaller clusters of active material detaching from the main phase-component and protruding deeper into the capillary.

In comparison, the main research goal in the investigations presented in chapter 6 was the impact of confinement to a channel of varying diameter on a growing sheet of epithelial cells. Specifically, we have analysed the spatial arrangement and the dynamics of individual cells. To this end, we used a Cellular Potts Model (CPM) that emulates single-cell dynamics within such a geometry. Cells are modelled as extended objects that occupy a certain connected area on a two-dimensional

lattice and dynamics are governed by a kinetic Monte-Carlo algorithm that tries to minimise a pseudo free energy. Inspired by the bonds real cells form with the substrate as well as with other cells, in the CPM occupation of lattice sites by cells and mutual contact of cells lead to energetic benefits while loosing cell-cell contacts is punished. Together with constraints on cell area and circumference, this leads to coherent sheets of finite-size cells. Biochemical processes inside real cells that lead to persistent motion in experiments as well as *in-vivo*, are mimicked with the help of a scalar field for every cell, the polarisation field. Where this field is high, the cell tends to conquer new lattice sites, where it is low, sites are more likely to be abandoned. The field is subject to a positive feedback mechanism: next to regions where cells expand, the field grows and where they retract, the field decays. This leads to an internal polarisation and makes cells move persistently, especially into regions that are not occupied by other cells. As in the setup for the active nematic, cells start in a reservoir at the channel entrance from where they invade the channel. A constant growth of the cellular assembly is ensured by a mechanism of cell division and growth of the individual cells. The fact that the CPM explicitly simulates extended objects allows observables related to position and motion of individual cells that cannot be defined in the nematic continuum model. Due to this, we could show that the radial distribution function of the cell sheet and the MSD of individual cells change with varying channel diameter. It turned out that cells tend to organise in sixfold-coordinated hexagonal structures, but are not caged between their neighbours, similar to particles in glasses. Perturbation by a bottleneck resulted in accumulation and retrograde flow of cells in front of the narrow part of the channel and in distortions of hexagonal order.

Both studies in comparison reveal the differences in phenomenology between the two models in similar situations. In the nematic system, where an ambient fluid is present and the active forces are strictly dipolar, no unidirectional polarised flow in direction of the channel axis can evolve. In contrast, the cells in the CPM with the built-in polarisation mechanism and the intercellular coupling coherently move into the channel. An obstacle, like a bottleneck, can indeed hinder ongoing unidirectional expansion. Depending on the geometric details of the bottleneck, a part of the cells change direction and reverse motion, but due to the strong inherent polarisation the majority of cells still move on and squeeze through the bottleneck where velocity and density increase.

The reason for this difference lies in the assumptions underlying the construction of the nematic continuum model. It describes the dynamics for many particles which are interacting in a perfectly nematic way. That means that on every point in space the macroscopic observables, like the director $n_\alpha$, are an average value of microscopic quantities. This can be seen nicely when such theories are derived from Boltzmann equations[99–101, 104–106]. For example, $n_\alpha$ is the average orientation of individually moving objects. These objects can well move unidirectionally, like

cells on a substrate or bacteria that swim in a fluid. The assumption of perfect nematic symmetry however means that these particles align their body axes along a common axis and are equally likely to move in either direction along this axis. As a consequence, on average, the forces exerted on the fluid by the particles are dipolar and flow of particles is equal in both directions along this axis and cancels perpendicular to it. Then, on the macroscopic level, the polar properties of the microscopic particles vanish and only the average nematic dynamics remain.

The CPM in contrast is tailored to cellular systems. The internal polarisation field, adhesion and dissipation between cells and substrate, as well as growth behaviour are designed to emulate mechanisms of real cells. From that, cell-cell interaction results as an emergent property. An important factor is cell-cell dissipation that causes cells to stick to each other and makes them move into the same direction. In that way it generates a polar interaction. Also, cells in the CPM have the intrinsic tendency to conquer adjacent free space when density inside the cell sheet is high. This is because expansion to free space is a possibility for cells at the sheet boundary to get closer to their preferred cell size. Still it would be interesting whether it could under the right conditions lead to nematic symmetry in the cell-cell interactions, for example in a situation where density is homogeneous and there is no cell-cell dissipation. However, there are other, more fundamental differences between both models that cannot be bypassed. For instance, the technique cells use to crawl on a substrate relies on strong bonds between cells and substrate. In the CPM, this is implemented via the cell-substrate adhesion, a mechanism that is fundamentally incompatible with momentum conservation. In comparison, the hydrodynamic active nematic model does only allow dissipation, but has no implementation of adhesion. As a consequence flow properties are generally expected to be different.

Taken together, we conclude that the active nematic model is more likely to work for systems where particle numbers are high and interaction is primarily nematic such that the statistical description is justified and eventual polar properties of the system are negligible. In addition, cohesion of particles needs to be high. Then the description of a system with a nematic and an isotropic phase with interfacial energies is suitable. This could apply to biofilms, because these consist of a large number of bacteria (up to a million and higher) that stay close to each other and are embedded in extracellular material to establish a protected and beneficial environment. Many bacterial species additionally have elongated bodies and use flagella for self-propulsion, thus pairwise interaction could be approximately nematic and they would qualify as active matter. Indeed, nematic models have been used to describe bacterial systems[163, 177] and the importance of growth to biofilm formation has been pointed out in several studies[87–89]. The CPM by design is suitable for the description of invading epithelial cell sheets. It incorporates key mechanisms of collective cellular behaviour and models of this type have been applied to a number of experiments[79, 269–271].

In the introduction we have discussed three main reasons for researching active matter. In retrospect, how well do these arguments work to justify our studies? We have explored the properties of models for active matter under the influence of confining geometry. Differences in the results between models can be explained by differing assumptions made for the construction of these theories. With this in mind, we can suggest biological systems where the models could potentially be applied: growing bacterial colonies for the active nematic continuum model and invading epithelial cells for the CPM. If corresponding phenomenology was observed in these systems, our models could provide "minimal" explanations based on physical concepts. If, for example, different strands of bacteria showed different invasion modes corresponding to the different regimes found in our simulations, our model would suggest differences in activity as the cause regardless of the detailed rules that govern the collective dynamics of the bacteria.

The CPM predicted remarkable material properties for epithelial cells. The cell sheet shows features typical to "classical" solids and "classical" fluids at the same time, namely an average regular hexagonal order and unbounded relative motion of individual cells, comparable to a glass that is constantly moving in a coordinated fashion. Additionally, cells are able to adapt their configuration to the varying diameter of the channel. These findings constitute an interesting extension of the known features of cellular systems.

We thus in summary hope to have contributed to active matter research in all three directions listed in the introduction: We extended our knowledge about two established models by simulating them under previously untested conditions. In that process, we found interesting physical properties in one case (material properties of cells in the CPM), and could make a prediction for a biological system with potential functional relevance in another (invasion schemes for appropriate biological systems with the active nematics continuum model).

# Appendix

## 1 Additional information on studies with the active nematics continuum model

### 1.1 Description of movies for invasion setup

All movies show the time-evolution of the velocity field on the left hand side and the orientation field on the right hand side, in the same way as panels B-D in Figure 3.3 in chapter 3. We choose different values of the activity $\zeta$ to display the qualitatively different phenomena.

Individual files are available as supplementary material to [1] and can be downloaded from http://dx.doi.org/10.1039/C9SM01210A. There are the following files:

**flows0020.mp4** $\zeta = 0.0020$. System is in regime I, director homogeneous and parallel to the interface. Corresponds to Figure 3.2 A, leftmost panel.

**flows0030.mp4** $\zeta = 0.0030$. System is in regime I, but the director starts to show deviations from the perfectly homogeneous configuration, especially close to the reservoir. Corresponds to Figure 3.3 B.

**flows0035.mp4** $\zeta = 0.0035$. System is in regime 2, showing characteristic flow- and director-fields. At later times the periodic dynamics described in section 3.3.2.1 can be observed. Corresponds to Figures 3.2 A (middle panel) and 3.3 C.

**flows0046.mp4** $\zeta = 0.0046$. System is the higher activity region of regime II. The video shows two examples of the switching behaviour described in section 3.3.2.2 and Figure 3.4 B.

**flows0052.mp4** $\zeta = 0.0052$. System is in regime III. This example shows the typical birth of small active clusters, corresponding to the situations shown in Figures 3.3 D and 3.4 C.

**flows0060.mp4** $\zeta = 0.0060$. System is deep in regime III. The dynamics is more turbulent than in the video for $\zeta = 0.0052$; there are more defects and clusters. Corresponds to the example shown in Figure 3.2 A on the right panel.

## 1.2 Parameter variations for droplet setup

In Figures 1,2, results for $\xi = 0.3$ are shown. The tumbling parameter $\xi$ determines the behaviour of the nematic order parameter under shear flow. As in the systems steady state flows are present, this parameter could be relevant for the director field and thus also the droplet shape. In Figure 1, time evolution for a selection of observables is shown, in Fig. 2 a detailed view on the director field inside the droplet.

The droplet is flatter for $\xi = 0.7$ and pressure difference between phases as well as root mean-squared velocity are higher for same activity $\zeta$. Incontrast, the gradient deformation is weaker: for $\xi = 0.3$ it is $\approx 20°$ at the ends of the droplet while it is $\approx 15°$ for $\xi = 0.7$. As the interface is longer for $\xi = 0.7$, also the total free energy $\mathcal{F}$ is higher as the quotient $\mathcal{F}/L$ is unaffected. Also, dynamics for $\xi = 0.7$ seem to be faster as observables get close to the steady-state values earlier in the simulations.

Thus, for $\xi = 0.3$ the same active forces lead to a stronger distortion in the director field, but the droplet shape deviates less form a semi-sphere and dynamics are slower. Qualitatively, this means that because the director tends to follow the interface more easily, the active anchoring effect leads to less deformations of the interface. This is in line with the conjecture we presented for the mechanism governing interface deformations at the end of section 4.3.3 in the main part.

Second, we vary the energetic coefficients $K_\phi$ and $K_Q$ in Fig. 3. Interestingly, the observables not directly related to the free energy are altered only slightly.

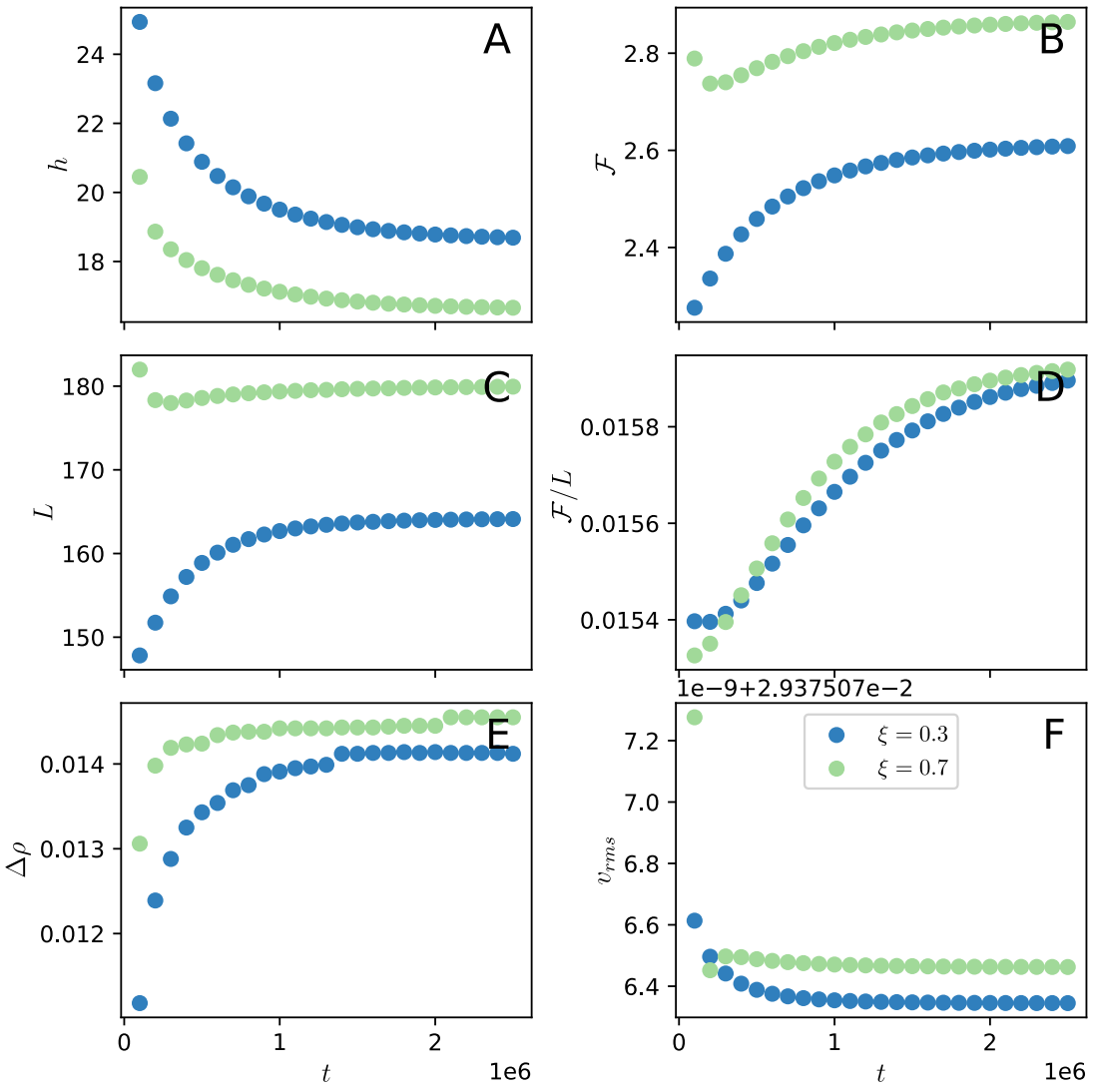


**Figure 1** *Time evolution of selected observables for different tumbling parameter $\xi$ for $\zeta$ =* 0.0050. (blue: $\xi = 0.3$, green: $\xi = 0.7$) (A) Height of droplet $h$, (B) free energy $\mathcal{F}$, (C) length of interface $L$, (D) quotient $\mathcal{F}/L$, (E) difference of fluid density between nematic and isotropic phase $\Delta\rho$, (F) mean squared velocity $v_{rms}$. For flow-aligning nematics ($\xi = 0.7$) form a flatter droplet than flow-tumbling nematics ($\xi = 0.3$), analogously the free energy $\mathcal{F}$ is higher for $\xi = 0.7$.

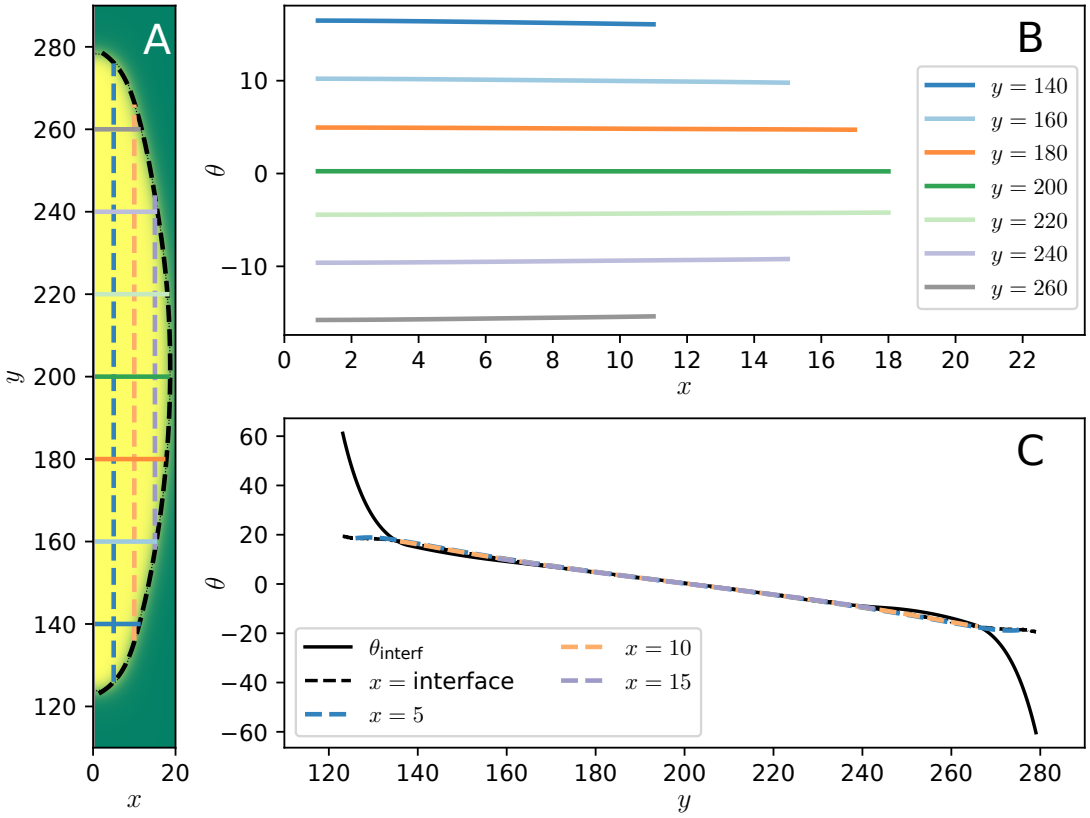


**Figure 2** *Director field along sections through the droplet for* $\xi = 0.3$. (A) Illustration of sections along which director inclination is shown in (B,C): solid lines in (B) show director inclination along solid lines of same colour through droplet in A, analogously dashed lines in (C). (B,C) show the angle of the director relative to the $y$-axis. In (B), sections are along lines of constant $y$. Two features are apparent: the angle is constant along the sections and its absolute value symmetrically increases with increasing distance from the droplet centre. In (C), the reason becomes clear. The black solid line shows the inclination of the interface, the black dashed line the director angle along the same line. For $y$-values where the interface is relatively flat, the director follows it closely for all $x$. Where the interface inclination varies more strongly, the director ceases to follow. The gradient varies stronger with increasing distance from the centre of the droplet and reaches higher final values when compared to the results for $\xi = 0.7$ (see Figure 4.6 in the main part).

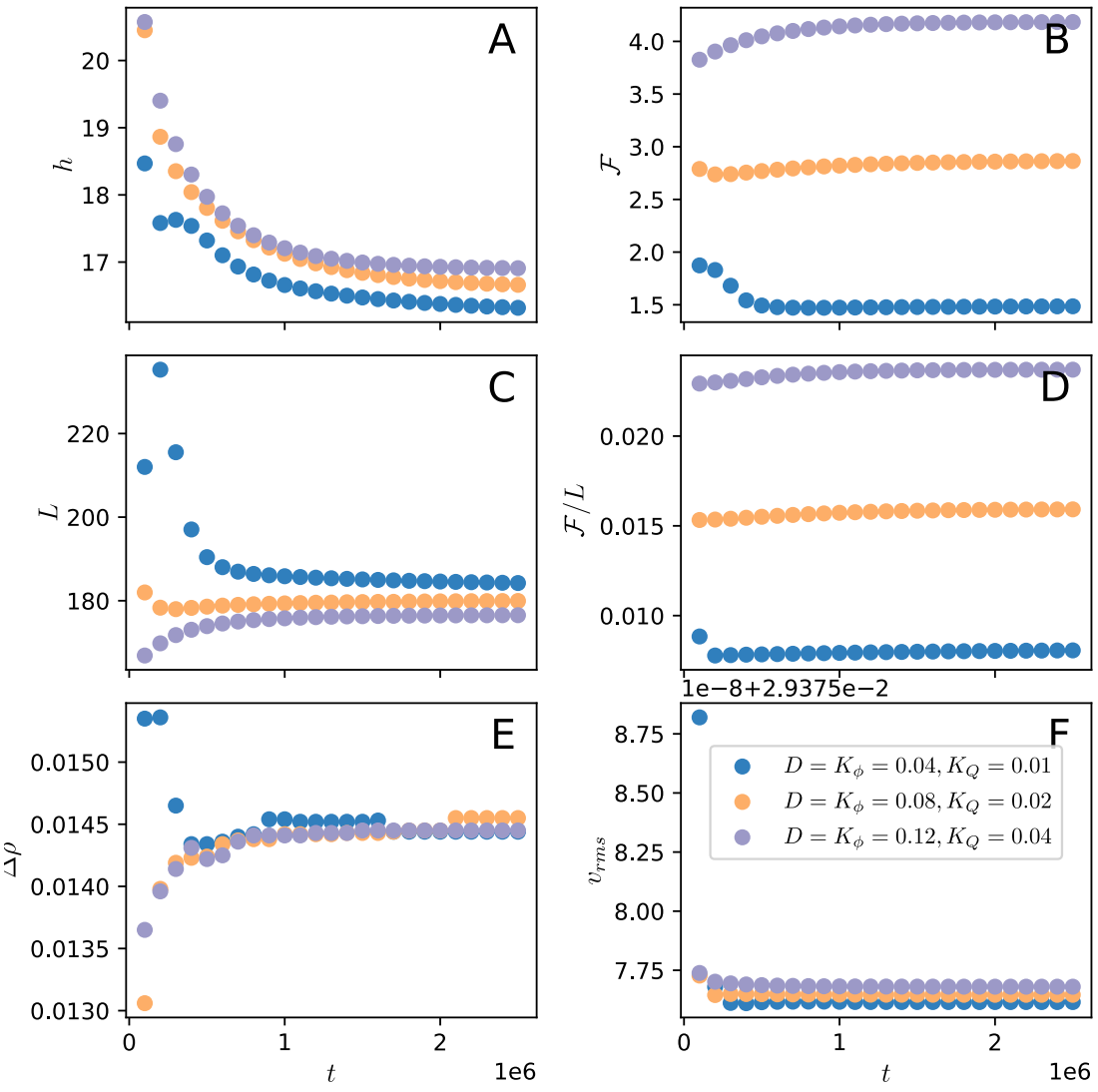


**Figure 3** *Time evolution of selected observables for different elastic constants $K_\phi, K_Q$.* (A) Height of droplet $h$, (B) free energy $\mathcal{F}$, (C) length of interface $L$, (D) quotient $\mathcal{F}/L$, (E) difference of fluid density between nematic and isotropic phase $\Delta\rho$, (F) mean squared velocity $v_{rms}$. The free energy has only minor influence on the shape of the droplet and steady state $v_{\mathrm{rms}}$ and $\Delta\rho$ despite considerable differences in the free energy.

## 1.3 Elliptical approximation of droplet interface

The interface can be approximated quite well as an ellipse. See an example plot in Fig. 4 where also resulting unit vectors in the corresponding elliptical coordinate system with coordinates $\mu, \nu$ are shown. The approximation has the advantage that it gives a simple parametrisation that is well-behaved in contrast to numerical interpolations. This becomes clear when calculating curvature and the local radius (see Fig. 5). The curvature is calculated by taking derivatives. This can lead to divergences in the local radius which is the inverse curvature when the derivatives are calculated from an interpolation. In contrast, the radius is always well-defined for an ellipse.

For the projections of vectorial quantities on the tangent and normal vectors, the method to determine interface and tangent or perpendicular vectors, has not a big influence. As an example, projections of forces as defined in Eq. (4.14) are shown in Fig. 6).

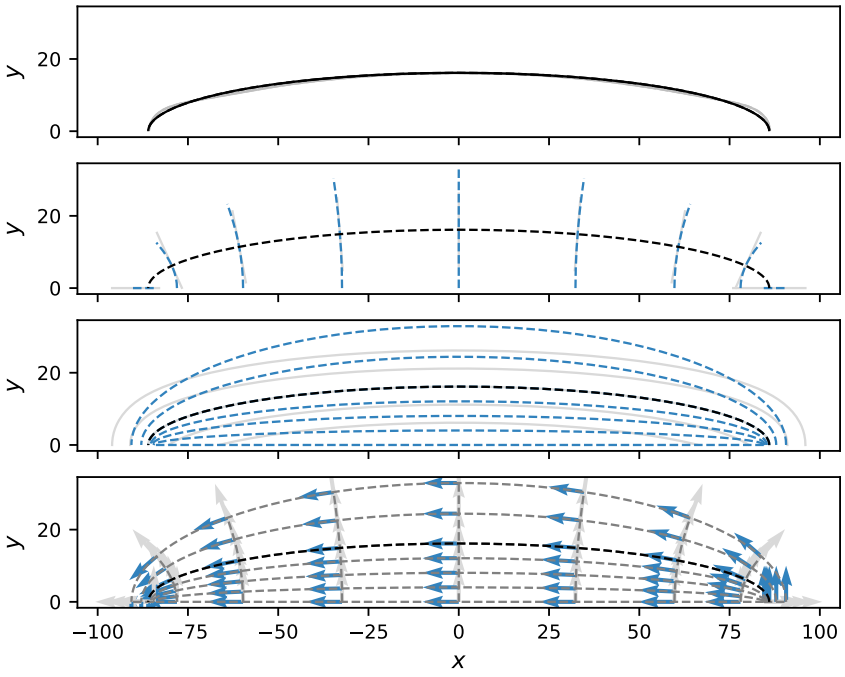


**Figure 4** *Properties of the elliptical approximation.* Top panel: elliptical approximation (black) and interpolated interface (gray line) are largely on top of each other. The next two panels illustrate the elliptical coordinate system $(\mu, \nu)$: The second panel shows lines of constant $\nu$ (blue dashed) and lines perpendicular to the interface (gray lines). The third panel analogously lines of constant $\mu$ (blue dashed) and lines parallel to the interface (gray lines). In the lowest panel, unit vectors in direction of $\mu$ (blue) and $\nu$ (gray) are shown. At the interface, these are tangent and normal to the interface, respectively.

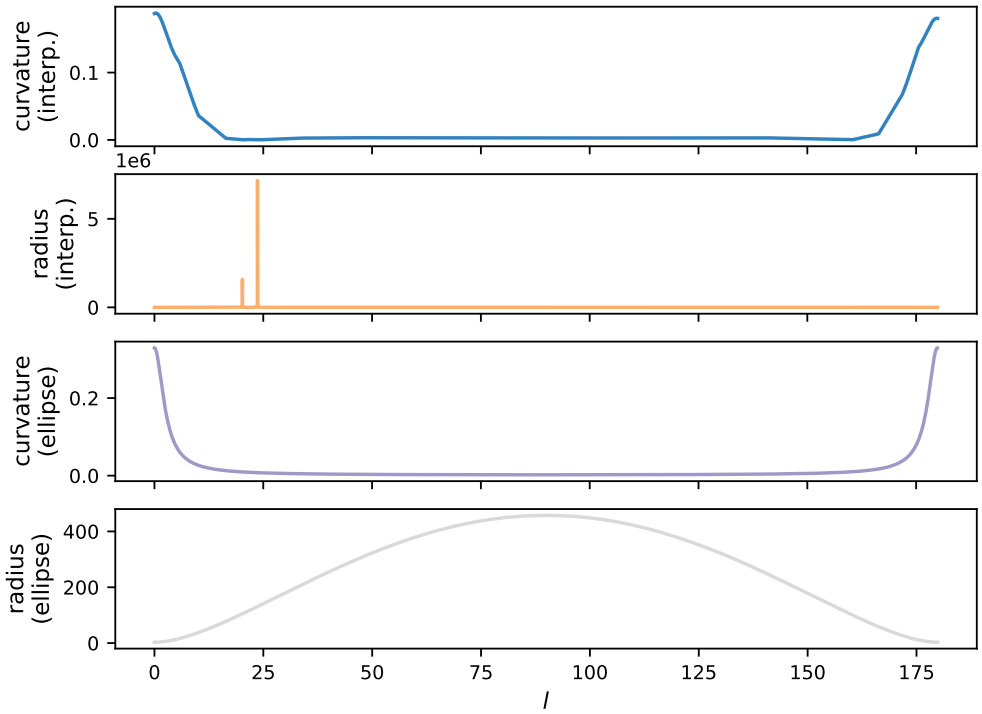


**Figure 5** *Curvature and local radius for interpolation and elliptical approximation.* Curvature is smoother for the elliptical approximation. As a consequence, for the interpolation the radius diverges, while it is well-behaved for the elliptical approximation.

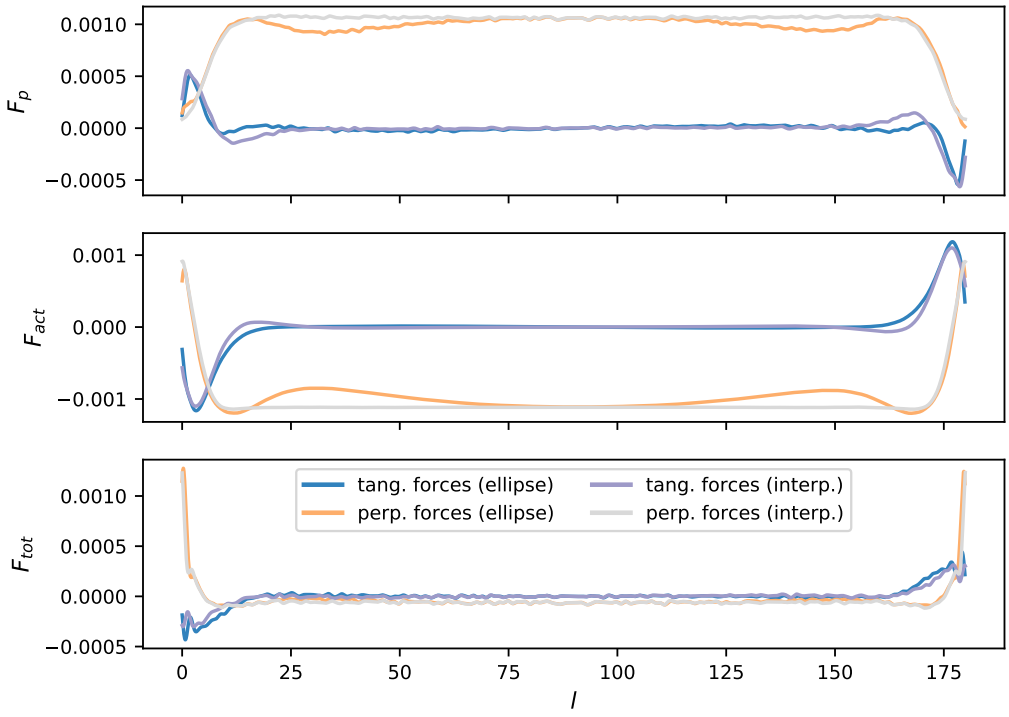


**Figure 6** *Tangential and perpendicular components of active and pressure forces for interface from interpolation and elliptical approximation.* For active forces (upper panel), pressure forces (middle panel), and total forces (lower panel), the results do only very little depend on the method for determining the interface and the tangent vectors. Naturally, the elliptical approximation leads to a smoother result.

# 2 Additional information on studies with the Cellular Potts Model

## 2.1 Model and parameters

We use the model as presented in [142] with a slightly adapted cell cycle and parameters.

### 2.1.1 Simulation procedure

Before the actual simulation, cells are randomly seeded in a reservoir left of the channel entrance. For a certain burn-in time (700 time steps in our case), cells can evolve freely in this reservoir. In this time, the cell density grows to maximum density in the reservoir. After that time, cells are finally allowed to enter the channel and the actual simulation starts. Also then, cell division is limited to the reservoir.

### 2.1.2 Implementation of cell cycle

Compared to [142], we modified the quiescent phase in that we made the transition to growth stochastic in order to achieve a less deterministic cell-cylce and to avoid unwanted synchronisation of cell division. The rest remains unchanged.

A freshly initialised cell, or a daughter cell right after cell division, is in the *quiescent state*. In the original model, the cell would now switch into the *growing state* if its size, via fluctuations, grew larger than a certain threshold size $rA_{\mathrm{ref}}$ (for explanation of parameters see Table 1 in the next section). In the version used for this work in contrast, the cell switches into an intermediate state, the *refractory state*, in which it does not grow. From there, it can switch into the growing state in every simulation step with a probability of $p = 1 - \exp\left(-1/T_q\right)$ with $T_q$ a newly introduced characteristic waiting time. From there, the cell cycle works exactly as described in [142].

### 2.1.3 Parameters used

As we have used the model from [142], we use the notation convention for parameters from there. The values are given in Tables 1 and 2.

| Cell parameters | | | |
|---|---|---|---|
| Parameter | Value | Function | Comment |
| $\epsilon_0$ | 75 | strength of cell-substrate adhesion /average polarisation speed | |
| $\Delta\epsilon$ | 45 | cell polarisability: the cell polarisation $\epsilon$ is in the interval $\epsilon \in [\epsilon_0 - \Delta\epsilon/2, \epsilon_0 + \Delta\epsilon/2]$ | parameter influences the persistence of cells and overall invasion speed |
| $D$ | 0 | strength of cell-substrate dissipation: energy penalty for abandoning a tile, i.e. breaking cell-substrate bonds | finite values slow down dynamics |
| $\mu$ | 0.10 | cytoskeletal update rate | sets overall timescale. |
| $R$ | 2 | signalling radius | when a cell conquers a tile, the polarisation field increases for tiles of this cell within radius $R$ of the new tile |
| $\kappa_A$ | 0.10 | area stiffness | |
| $\kappa_P$ | 0.20 | perimeter stiffness | together with $\kappa_A$ and $\epsilon_0$ sets the preferred size of a single cell $A_{\text{ref}}$: $A_{\text{ref}} = \left(\epsilon_0 - 2\pi\sqrt{3}\kappa_P\right) / \left(\sqrt{3}\kappa_A\right)$ |
| $B$ | 10 | strength of cell-cell adhesion | See section 2.1.4 for results for $B = 5$. |
| $\Delta B$ | 0 | strength of cell-cell dissipation | |

**Table 1** Parameter values used in our study, following the the notation convention from [142].

| Parameters for cell division | | | |
|---|---|---|---|
| $T_g$ | 350 | cell growth duration | in this time, the cell grows exponentially to double its size by increasing the preferred cell-size by adjusting $\kappa_A$ and $\kappa_P$. |
| $T_d$ | 50 | cell division duration | in this time, the cell is immotile and the polarisation relaxes to neutral. After that, the cell splits |
| $T_q$ (new) | 100 | cell quiescence duration | after cell division, the cell does not grow for this time on average |
| $r$ | 0.50 | relative threshold for cell growth | after the quiescent phase, the cell starts growing if its size is larger than $rA_{\text{ref}}$ |
| Numerical parameters | | | |
| $N_0$ | $\approx 1100$ | initial number of cells | |
| | 700 | burn-in time | |
| | $D = D_0/2 : 3000$, $D = D_0 : 4000$, $D = 2D_0 : 5000$. | simulation time | |
| | $2500 \times 1200$ | dimensions of simulation area | |
| $k_BT$ | 5 | effective temperature | reference energy of fluctuations in the Monte-Carlo algorithm |
| | 1 | seed | seed for rng |

**Table 2** Parameter values used in our study, following the the notation convention from [142].

### 2.1.4 Variation of cell-cell adhesion

In this section we examine the effect of variations in the cell-cell-adhesion $B$. The cell-cell-adhesion defines the effective free energy gained from an edge that a cell shares with another cell compared to the situation where the edge borders to a free tile. A higher cell-cell-adhesion parameter thus favours cohesion of cells.

Interestingly, higher cell-cell adhesion also leads to faster dynamics in the invasion of the channel, as can be seen in Figs. 7A and 8A. There we show simulations with cell-cell adhesion parameter $B = 5$ in comparison to the simulations with $B = 10$ in the main part. Lower cell velocities for $B = 5$ are particularly prominent in regions $R_1$ and $R_2$ for medium and large bottleneck diameters $d_0, d_-$. One explanation is that for higher benefits through adhesion, trailing cells are faster to follow leading cells as they are faster to form common edges. In that way, advancements of a single cell are translated more directly into advancements of the collective.

While the peak-distribution in the angular distribution $f_\phi(\phi)$ is not significantly altered (Figs. 7C, 8C), the radial distribution $f_r(r)$ shows slightly smaller cell-cell distances for larger cell-cell adhesion (Figs. 7D, 8D) which additionally promotes cell-flux and thus faster invasion (Fig. 8A). The single-cell dynamics in the cell sheet scale comparably (Figs. 7B, 8E).

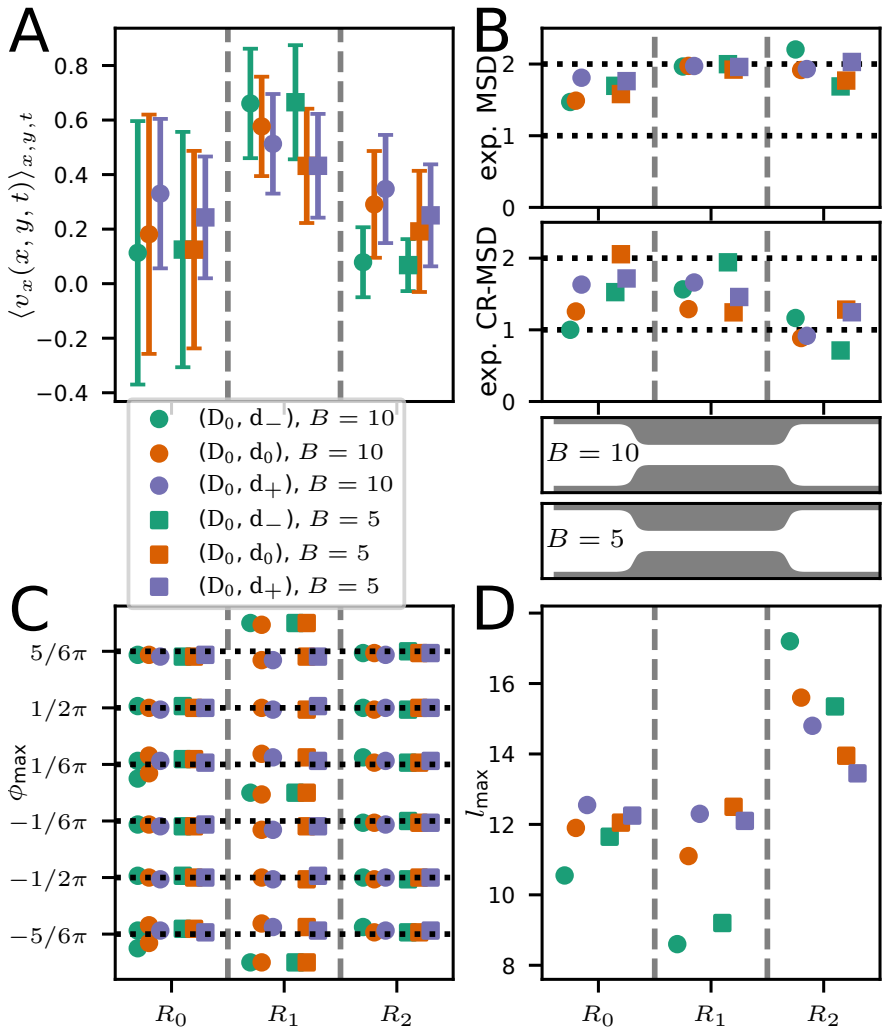


**Figure 7** *Comparison of structure and dynamics for different values of cell-cell adhesion energies.* (A) Average velocity in channel-axis direction in the three different regions. Higher cell-cell adhesion leads to higher values, especially in region $R_1$. (B) Comparison of scaling of MSDs. The ordinary MSD (upper panel) scales very similarly for both, showing ballistic motion in the narrow region and behind as well as reduced scaling as a sign of backflow before the bottleneck. (C) Angles at which maxima in the RDF appear. Results are very similar. (D) Typical distance of maxima from the center in the RDF. As can also be seen in Figure 8, the cell-cell distance is larger for smaller cell-cell adhesion, especially in smaller channels.

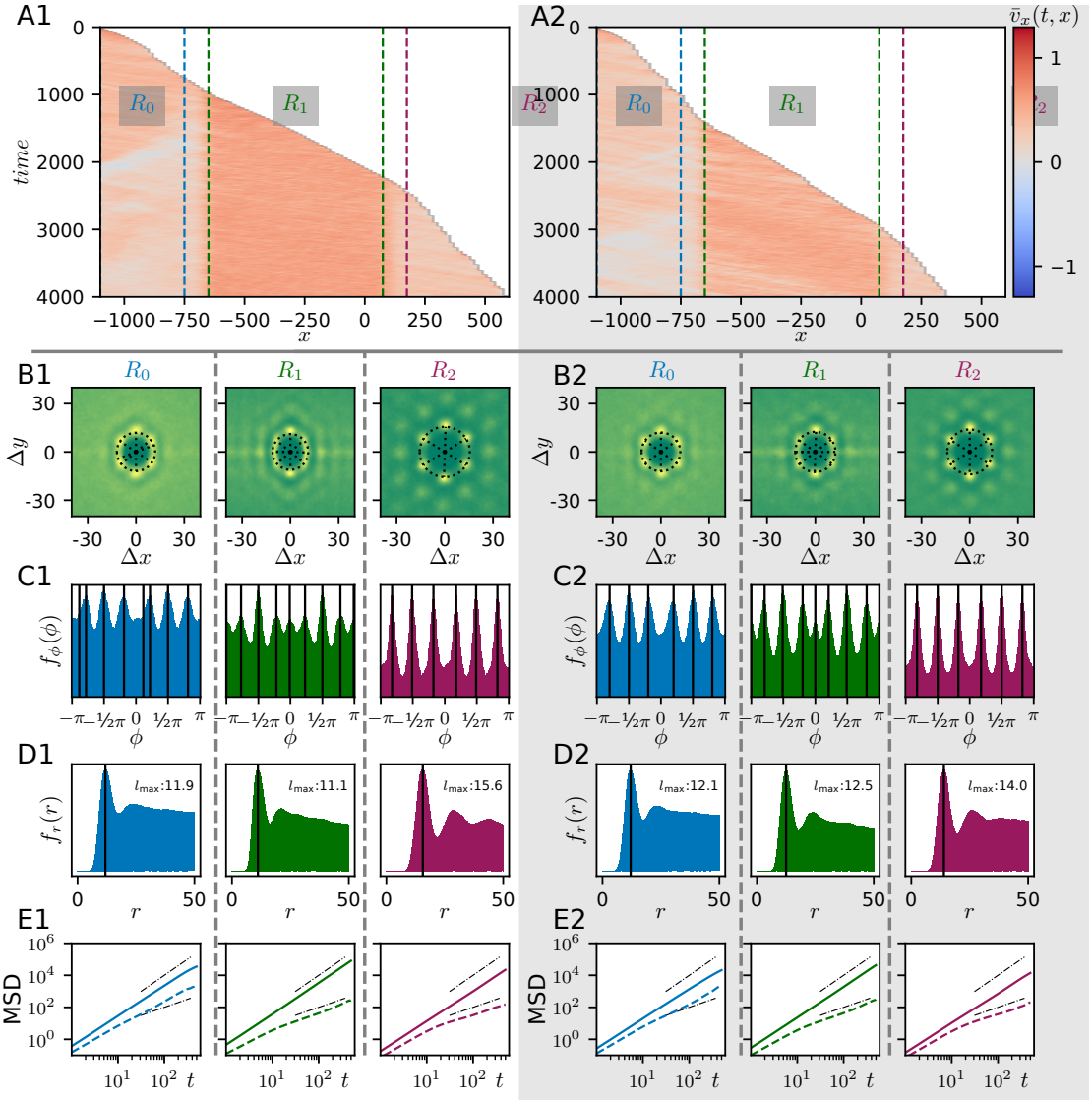


**Figure 8** *Comparison of order and dynamics for different values of cell-cell adhesion energy. Left side (panels Xa): $B = 10$, right side (panels Xb): $B = 5$).* (A) Kymograph of the velocity in channel direction $v_x(t,x)$. (B-D) Radial distribution functions (RDFs) for the different regions of the channel. The angular position of peaks is mostly unaltered (panel C), while the distance between cells in larger for smaller adhesion (panel D). (E) Mean-squared displacement (solid line) of cells as well as cage-relative mean-squared displacement (dashed line). Black dashed-dotted lines show linear and quadratic scaling, respectively.

## 2.2 Methods

### 2.2.1 Analysis of the radial distribution function (RDF)

As explained in the main part, the RDF is defined as (Eq. (6.1) in section 6.3.2 of the main part)

$$g(\mathbf{r}) \propto \left\langle \sum_{\alpha \neq \beta} \delta\left(\mathbf{r} - \mathbf{r}_\alpha + \mathbf{r}_\beta\right) \right\rangle_t \tag{1}$$

with the double sum running over all pairs of cells in the area under observation, $\mathbf{r}_\alpha, \mathbf{r}_\beta$ being the positions of the cells[38], and the angular brackets indicating a time average.

The arrangement of peaks on a circle around the origin (see Fig. 6.4 in section 6.3) suggests to analyse the angular distributions of peaks on this circle as well as its radius. To this end, we define the radial and the angular distribution functions as:

$$f_r(r) = \int_0^{2\pi} r \mathrm{d}\phi \;\; g(\mathbf{r}) \;\text{ and} \tag{2}$$

$$f_\phi(\phi) = \int_0^{r_{\min}} \mathrm{d}r \;\; g(\mathbf{r}), \tag{3}$$

respectively. Here, polar coordinates are defined as $\mathbf{r} = (r\cos(\phi), r\sin(\phi))$. Due to the symmetry $g(\mathbf{r}) = g(-\mathbf{r})$, $f_\phi(\phi) = f_\phi(\phi \pm \pi)$. The upper boundary for the radial integration is $r_{\min}$, the position of the first minimum after the first maximum of $f_r(r)$; this choice ensures that only the nearest neighbours contribute to $f_\phi(\phi)$. From $f_r(r)$, we obtain $l_{\max}$ simply as the maximum closest to the center, and $r_{\min}$ the minimum following it.

For the analysis of $f_\phi(\phi)$, we aim at detecting the number of peaks or, more specifically, judging how well it fits a regular six-fold symmetry or whether the peaks at $0, \pm\pi$ are more prominent.

**maxima detection** For the peaks, we on purpose chose a simple definition. A peak is defined as a maximum $\phi_{\max}$ if $f_\phi(\phi_{\max}) > 0.5 f_\phi(\phi_{\max,0})$ with $\phi_{\max,0}$ the absolute maximum of $f(\phi)$. Also, no maxima are allowed closer than $0.1\pi$ to another maximum to avoid small bumps on the flanks of peaks in $f_\phi(\phi)$ to be counted. Still, sometimes additional peaks are detected, as in Fig. 6.3 Bb in the main part.

Also, as we are looking at an observable with a hard criterion (maximum/ no maximum), gradual changes in the distribution lead to jumps in the results. This is why in the region where the distribution is transitioning form six-fold to two-fold,

it should not be overestimated when maxima are detected at $\phi = 0, \pm\pi$. To show that the method is nevertheless suitable to detect qualitative changes in the system, we will have a detailed view on the angular distributions in the next section.

**Detailed view on angular distributions** In Figure 9, we can look at the distributions for parameters $D = D_0, d \in \{d_-, d_0, d_+\}$, the examples that are also shown in the centre column of Fig. 6.4 in the main part. We also show fits of a distribution with two and six peaks, respectively. For that, we use superpositions of the so-called wrapped Cauchy-distribution[284]:

$$p_{WC}(\phi|\mu,\gamma) = \sum_{n=-\infty}^{\infty} \frac{\gamma}{\pi(\gamma^2 + (\phi - \mu + 2\pi n)^2)} \tag{4}$$

where $\gamma$ is the scale factor and $\mu$ is the peak position of the "unwrapped" distribution. $\gamma$ is the only fitting parameter, positions of the peaks are set to $\pm\pi/6, \pm\pi/2, \pm5\pi/6$ and $0, \pm\pi$, respectively.

Figure 9 shows that the algorithm finds maxima at $\pm\pi/6, \pm\pi/2, \pm5\pi/6$ as well as at $0, \pm\pi$ only for the $D_0, d_-$ configuration in region $R_1$. In the other cases, the algorithm agrees with what is obvious to naked eye.

In addition, the similarity of the distributions can be estimated using the L-2 norm

$$L^2(f_\phi(\phi), p_x) = \sqrt{\int_{-\pi}^{\pi} \mathrm{d}(\phi)\ |f_\phi(\phi) - p_x(\phi)|^2}, \tag{5}$$

where in our case we compare the measured distribution $p(\phi) \equiv f_\phi(\phi)$ to a fitted distribution of six regularly distributed peaks $p_6(\phi)$, a fitted distribution of two peaks $p_2(\phi)$, and a flat distribution $p_{flat}(\phi)$. Results are shown and discussed in the lower panel of Figure 9. From what we observe there, we can conclude that the approximation with a distribution with two or six peaks captures the structure of the distributions sufficiently well and that in particular, one fits the data better than the other in all cases considered.

### 2.2.2 Mean-squared displacement (MSD) and cage-relative mean-squared displacement (CR-MSD)

The ordinary mean squared-displacement (MSD) is defined as follows:

$$MSD(t) = \left\langle \frac{1}{N} \sum_{i=1}^{N} \left[\mathbf{r}_i(t+\tau) - \mathbf{r}_i(\tau)\right]^2 \right\rangle_\tau, \tag{6}$$

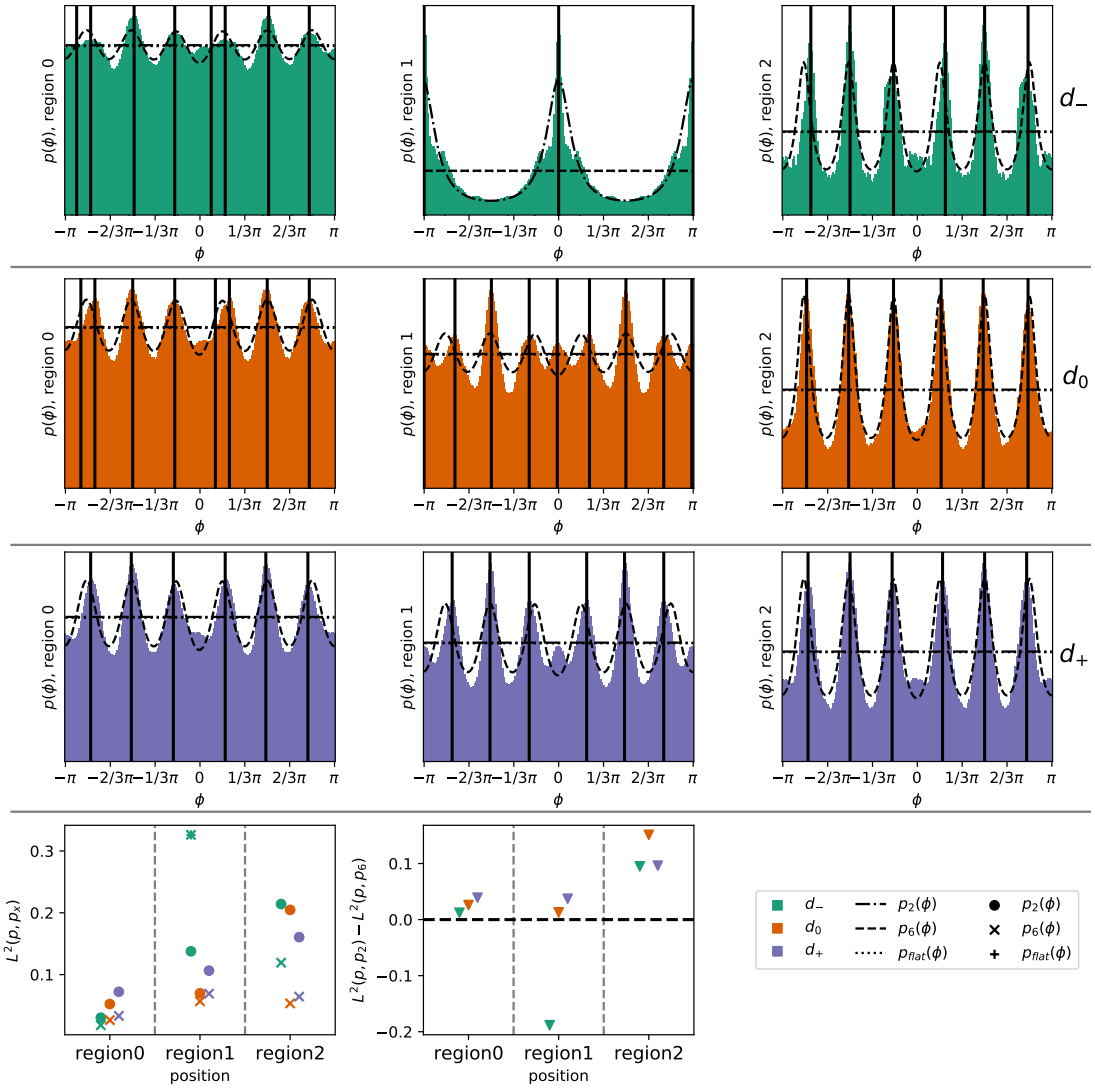


**Figure 9** *Comparison of measured marginalised radial distributions $f_\phi(\phi)$ to theoretical distributions.* Upper three rows show data for parameter sets $(D_0, d_-), (D_0, d_0), (D_0, d_+)$ for the three regions separately. Data is in colours, approximations as different lines according to legend. In region $R_2$, for all parameter combinations, we see six regularly distributed peaks. In region $R_0$ for all three case as well as in region $R_1$ for parameters $d_0$ and $d_+$ peaks are less prominent, but still sixfold and regular. Only for region $R_1$ and the narrowest bottleneck diameter $d_-$, there are only two peaks at $0, \pm\pi$. This is also reflected in the lowest row, where the $L^2$-distances between $p(\phi) = f_\phi(\phi)$ and $p_z, p_6, p_{flat}$ are shown. It becomes clear from the right plot that $p_6$ is the better fit in all cases except for $(D_0, d_-)$ in region $R_1$. Actually, the best fit for the distribution less less close to the data, turns out to be identical to the flat distribution.

with $N$ the number of cells under considerations and $\mathbf{r}_i(t)$ the position of cell $i$. In analogy the cage-relative MSD (CR-MSD) is defined as[279, 280]

$$MSD_{CR}(t) = \left\langle \frac{1}{N} \sum_{i=1}^{N} \left[ (\mathbf{r}_i(t+\tau) - \mathbf{r}_i(\tau)) - \frac{1}{N_i} \sum_{j=1}^{N_i} \left( \mathbf{r}_j(t+\tau) - \mathbf{r}_j(\tau) \right) \right]^2 \right\rangle_\tau . \quad (7)$$

Here, the second sum runs over all neighbours of cell $i$ at time point $\tau$, $N_i$ is then umber of neighbours at of cell $i$ at time $\tau$. Hence, the CR-MSD compares displacement of cells to the displacement of their original neighbours. The neighbours are determined by Voronoi tesselation.

We calculate the MSD for the last 500 time steps of the simulation and determine the scaling exponent $x$ of the MSDs by computing

$$x(t) = \frac{\partial MSD(t)}{\partial \ln(t)} \quad (8)$$

and averaging over $x(t)$ for the last half of these 500 time steps. This approach assumes a structure of the MSD as $MSD(t) \propto t^x$.

The CR-MSD stresses the local, or relative, dynamics. In a solid, the CR-MSD was to saturate reflecting “caging” of the particles, while the ordinary MSD also picks up global movement of the system as we have due to the invasion dynamics. A CR-MSD scaling linearly means that particles move diffusively relative to each other.

## 2.3 Additional figures

### 2.3.1 MSDs and CR-MSDs under variation of $D$ and $d$

Fig. 10 shows complete MSDs and CR-MSDs. The corresponding scaling exponents are plotted in Figure 6.5 in the main part of the thesis.

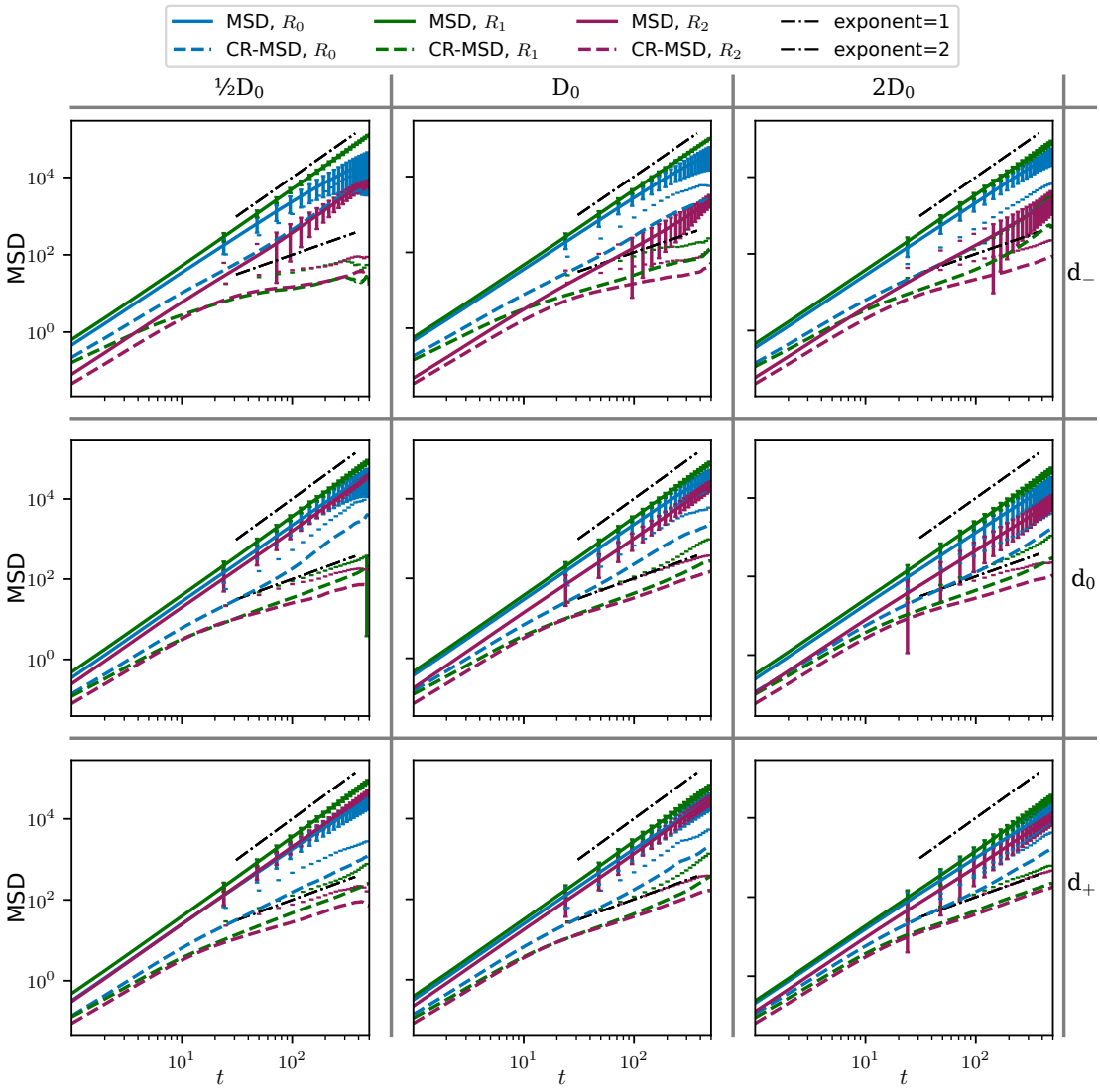


**Figure 10** *Log-log plot of MSD and CR-MSD for varying $D, d$.* The solid lines show the ordinary MSD, the dashed lines the CR-MSD. The ordinary MSD scales with exponent 2 in all regions, while the CR-MSD after an initial period of ballistic scaling grows to slower from $t \approx 10$ on. The CR-MSD in region $R_0$, shown in the blue dashed lines, is an exception to this, for all parameter configurations it grows faster than the other CR-MSDs, which is caused by the backflow in this region.

### 2.3.2 Additional figures for the configuration with a straight channel

Fig. 11 shows snapshots of density and velocity fields for an arbitrary time point. It is the corresponding figure to Fig. 6.2 for a bottleneck channel. In Fig. 12, we compare the structure of the cell sheet for varying diameters $D$. It corresponds to Fig. 6.4 for bottleneck channels.

Results for MSDs and CR-MSDs in straight channels are shown in Fig. 13 (analogous to Fig. 10) and Fig. 14 which is the same as Figure 6.5, but for straight channels of different diameters.

A summary of structural and dynamical differences is given in Fig. 15.

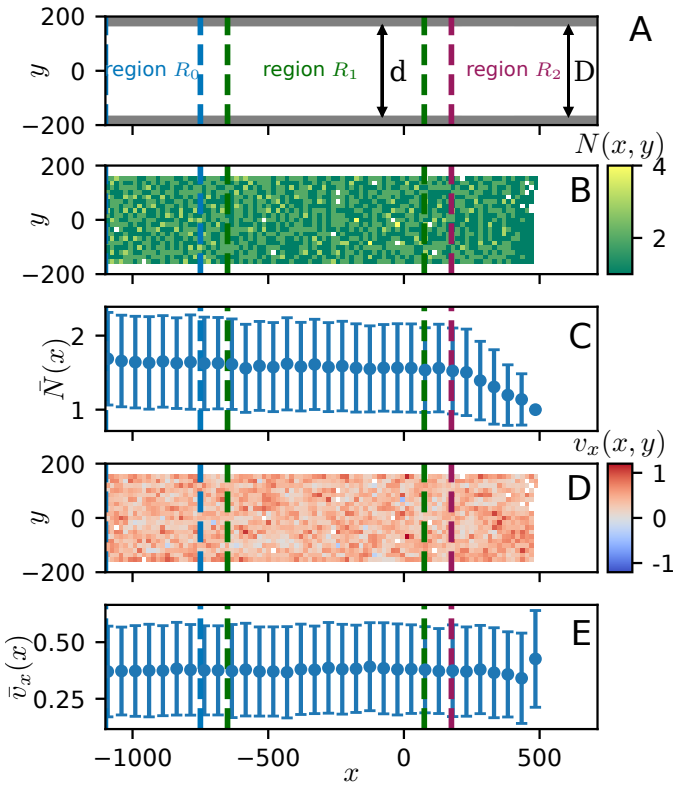


**Figure 11** *Example for simulation in a channel without bottleneck. Widht $D = D_0$ according to the convention in the main part.* Plot analogous to Fig. 6.2. (A) Geometry, (B) heatmap for particle number, (C) mean number of particles per bin. Apart from a slightly less dense region at the invasion front, the density is constant. (D) heatmap for velocity in channel direction, (E) mean velocity in channel direction, the value is constant throughout the cell-sheet.

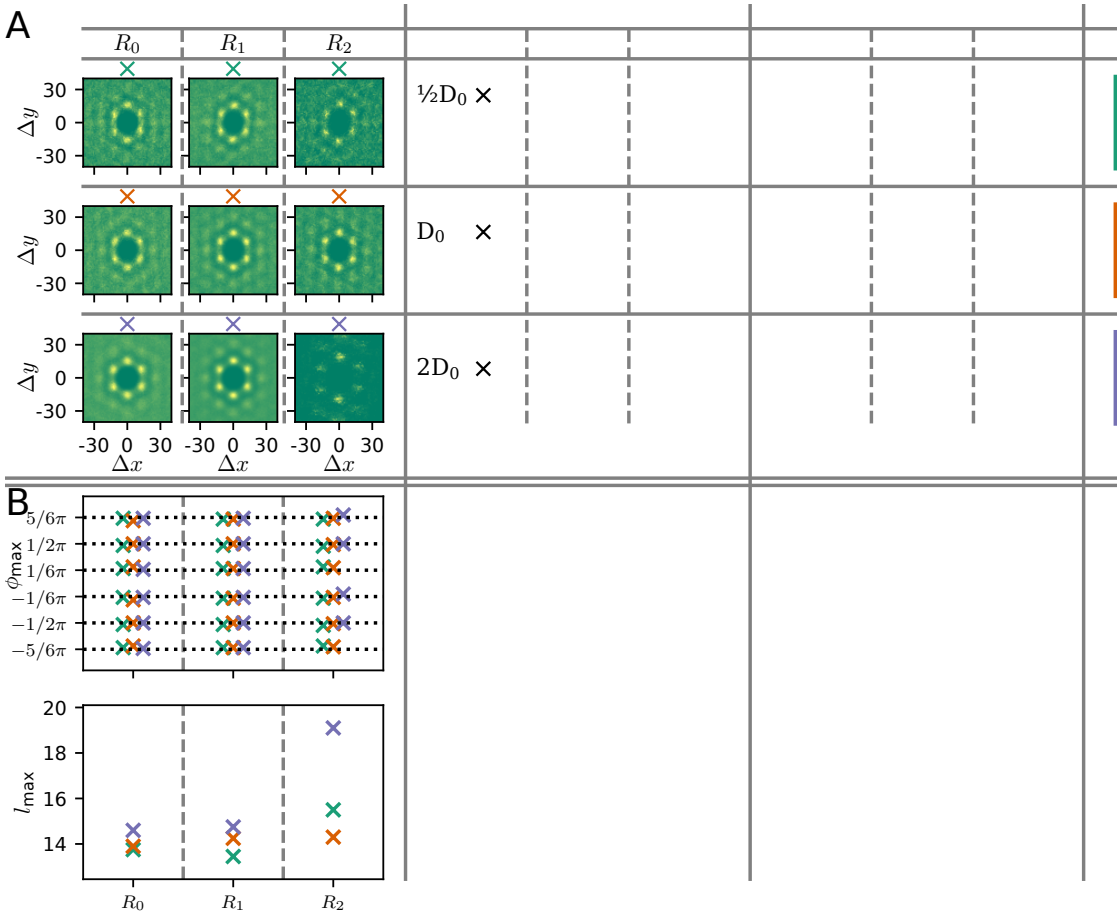


**Figure 12** *Comparison of cellular order in straight channels of varying width.* (A) Radial distribution functions (RDF) for different diameter $D$ for the different regions along the channel. From top to bottom: increase in $D$. In all regions, cells arrange in a regular hexagonal configuration. Low contrast in region $R_2$ for $D = 2D_0$ is due to the reduced invasion speed in the broader channel. (B) Results of quantitative evaluation of the results in part (A). The region is marked by the position of the markers along the horizontal axis of the respective plots. Varying colors indicate variations in $D$ as the small symbols above the plots in part A symbolise. *Upper panel*: Positions of maxima in the angular distribution obtained from radial integration of the RDF. *Lower panel*: position of maximum in the radial distribution obtained from the angular integral of the RDF. Distance of cells is a bit higher closer to the front, but very similar in regions $R_0$ and $R_1$.

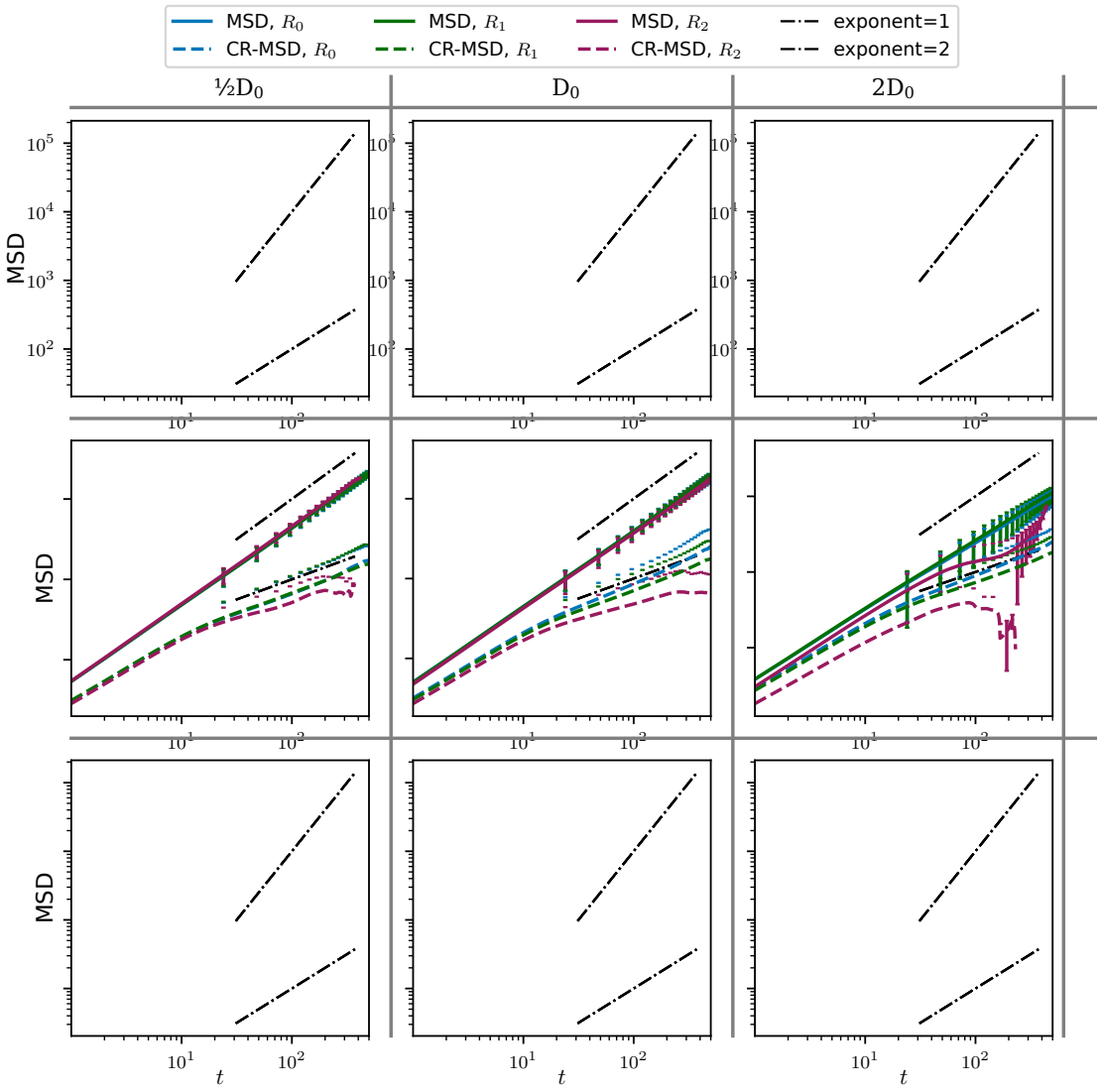


**Figure 13** *Log-log plot of MSD and CR-MSD for varying D in a straight channel (d = D).* The solid lines show the ordinary MSD, the dashed lines the CR-MSD. Ordinary as well as cage-relative MSD behave very similar across regions $R_0$ and $R_1$. In region $R_2$, close to the front, the CR-MSD scales significantly lower, especially for $D = D_0$. Compared to Fig. 10, there are no signs of backflow in region $R_0$, as CR-MSD scales linearly.

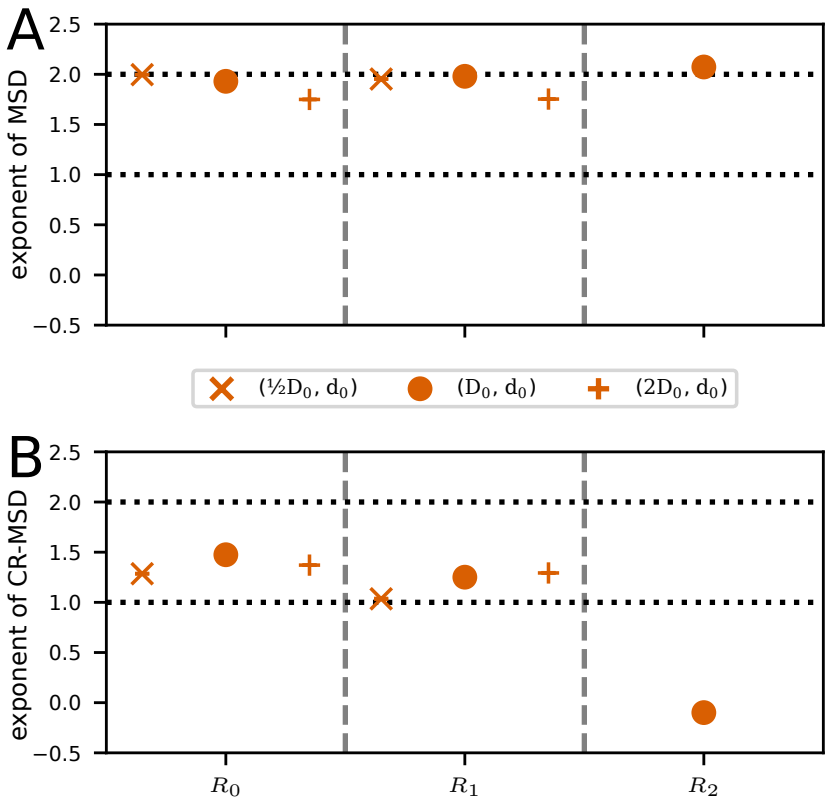


**Figure 14** *Comparison of MSDs in straight channels.* (A) Exponent from monomial fit to the late MSD for separate for regions $R_0$, $R_1$, and $R_2$. Results reflect what could already be seen in Fig. 13: the ordinary MSD in (A) expresses ballistically moving cells while the reduced exponents by the CR-MSD in (B) are lower. The stronger reduction in region $R_2$ is due to the presence of the front.

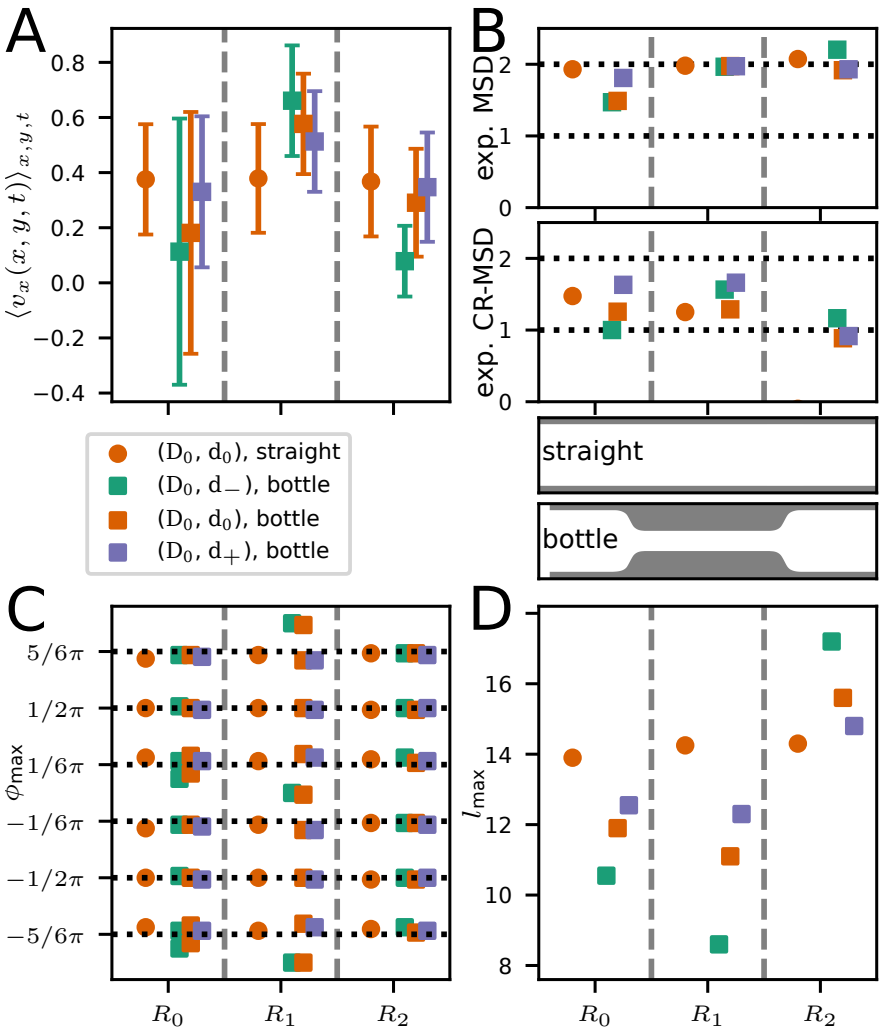


**Figure 15** *Comparison of internal organisation and dynamics for bottleneck channels and a straight channel as sketches between panels B and D illustrate.* (A) Average velocity in channel-axis direction in the three different regions. (B) Comparison of scaling of MSDs. (C) Angles at which maxima in the RDF appear. (D) Typical distance of maxima in the RDF from the center.

### 2.3.3 Additional figures for the configuration with longer funnel/ smoother transition

For more detailed comparisons of results for different funnel shapes, we present additional plots. Figs. 16-20 are in essence the same figures as in the main part of the thesis and Fig. 10, but for the geometry with the slender funnel.

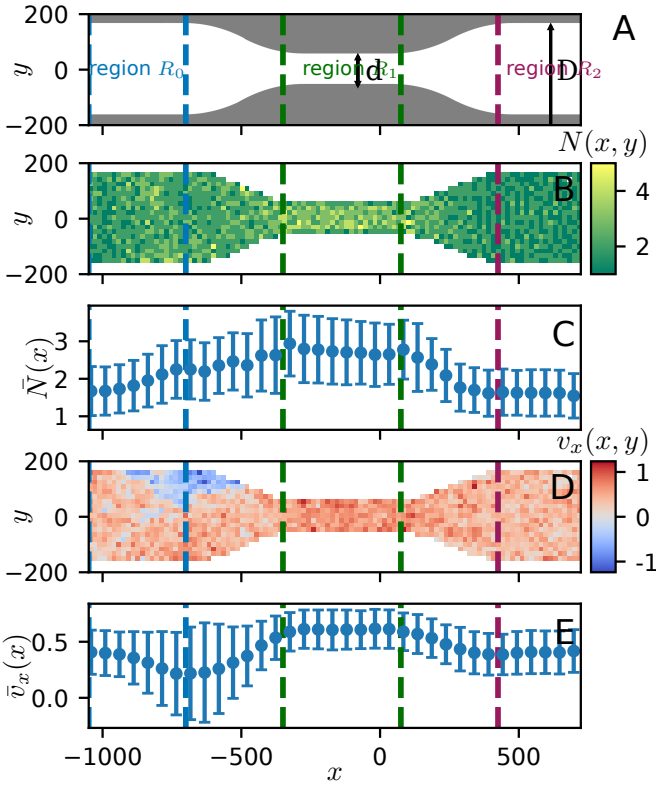


**Figure 16** *Example for simulation in a channel with longer funnel. Diameters $D = D_0, d = d_0$ according to the convention in the main part.* Plot analogous to Fig. 6.2. (A) Geometry, (B) heatmap for particle number, (C) mean number of particles per bin, (D) heatmap for velocity in channel direction, (E) mean velocity in channel direction. In comparison to Fig. 6.2, density and velocity are even more increased in the narrow part. The transition in density as well as velocity is distributed over the full lenght of the funnel, but backflow is still visible.

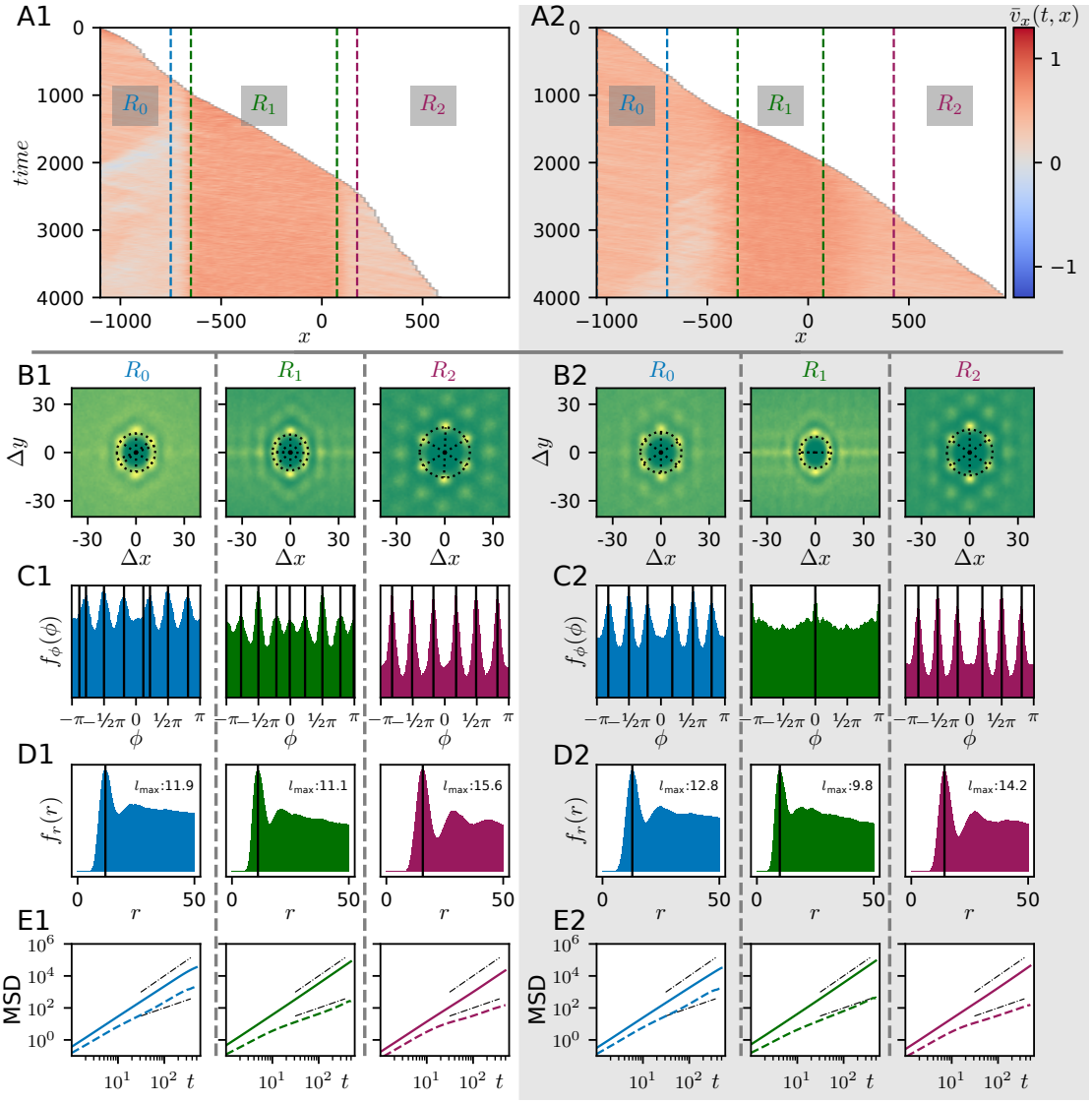


**Figure 17** *Comparison of order and dynamics for a constricted channel, parameters* $D = D_0, d = d_0$. Left side (panels Xa): bottleneck with steep transition, right side (panels Xb): bottleneck with smoother transition. (A) Kymograph of the velocity in channel direction $v_x(t,x)$. Dashed lines indicate transition regions from wider to narrower part. In comparison, the slender funnel leads to later and less backflow and in conjunction an overall faster invasion as the steeper frontline, especially in region $R_2$, shows. (B-D) Radial distribution functions (RDF) for the different regions of the channel. Panels C show the marginal distribution from integrating over the radius, and panels D integration over the polar angle. Vertical black lines in C mark maxima in the angular distribution as detected by the algorithm (for details see section 2.2 in the appendix). The vertical black lines in D mark the respective maximum of the radial distribution which gives the typical nearest-neighbour distance. Especially in the narrow region $R_1$, the slender transition creates a more dense cell sheet and different internal order as the angular distribution shows. (E) Mean-squared displacement (solid line) of cells as well as cage-relative mean-squared displacement (dashed line). Black dashed-dotted lines show linear and quadratic scaling, respectively.

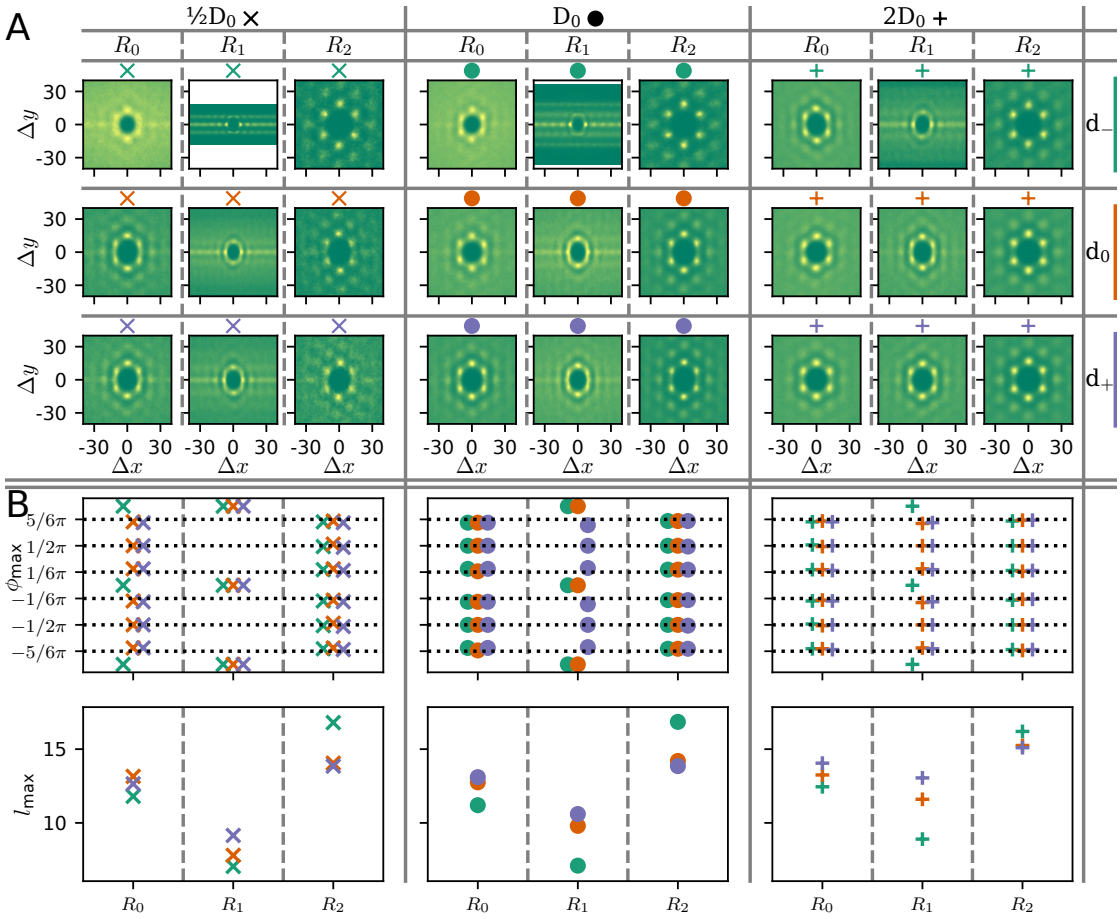


**Figure 18** *Comparison of cellular order in bottleneck channels of varying width with smoother transitions.* (A) Radial distribution functions (RDF) for different diameter $D$ and $d$ for the different regions along the channel. From left to right: increase in $D$, from top to bottom: increase in $d$. (B) Results of quantitative evaluation of the results in part (A). The region is marked by the position of the markers along the horizontal axis of the respective plots. *Upper panel*: Positions of maxima in the angular distribution obtained from radial integration of the RDF. *Lower panel*: Position of maximum in the radial distribution obtained from the angular integral of the RDF. In comparison to the analogous data in shown in Fig. 6.4 in the main part, for the steeper transition, the order in region $R_1$ is different for parameter sets $D = D_0, d = d_0$ and $D = 2D_0, d = d_0$. Especially there is no parameter set where the two distinct peak-patterns overlap. Also, variations in cell-cell distance/ cell density are stronger.

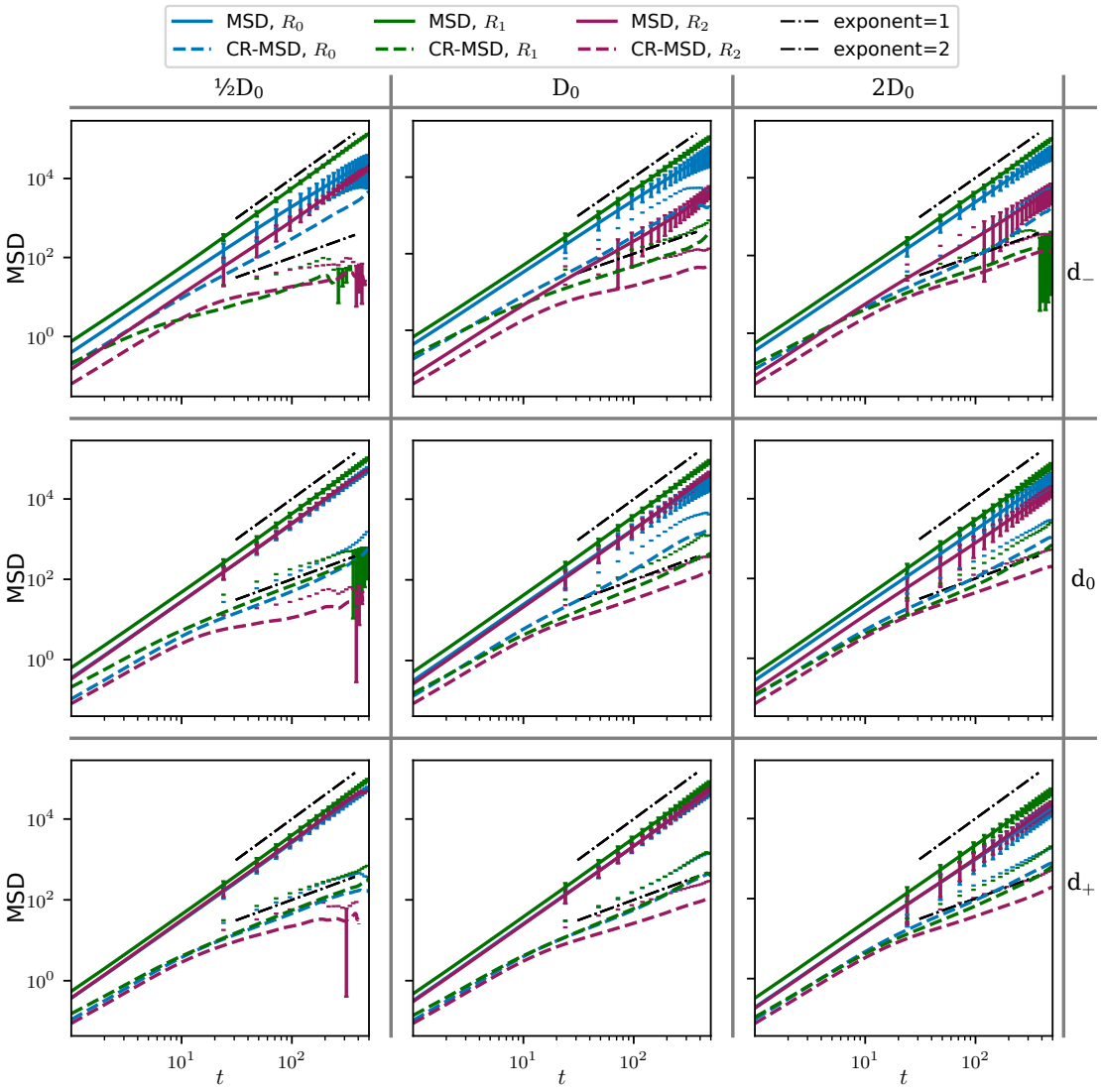


**Figure 19** *Log-log plot of MSD and CR-MSD for varying $D$, $d$ in the channel with the smoother transition.* The solid lines show the ordinary MSD, the dashed lines the CR-MSD. The ordinary MSD scales with exponent 2 in all regions, while the CR-MSD after an initial period of ballistic scaling grows to slower from $t \approx 10$ on. The exception is again the CR-MSD in $R_0$ that in channel regions of smaller $D$ or $d$ grows comparable to the ordinary MSD.

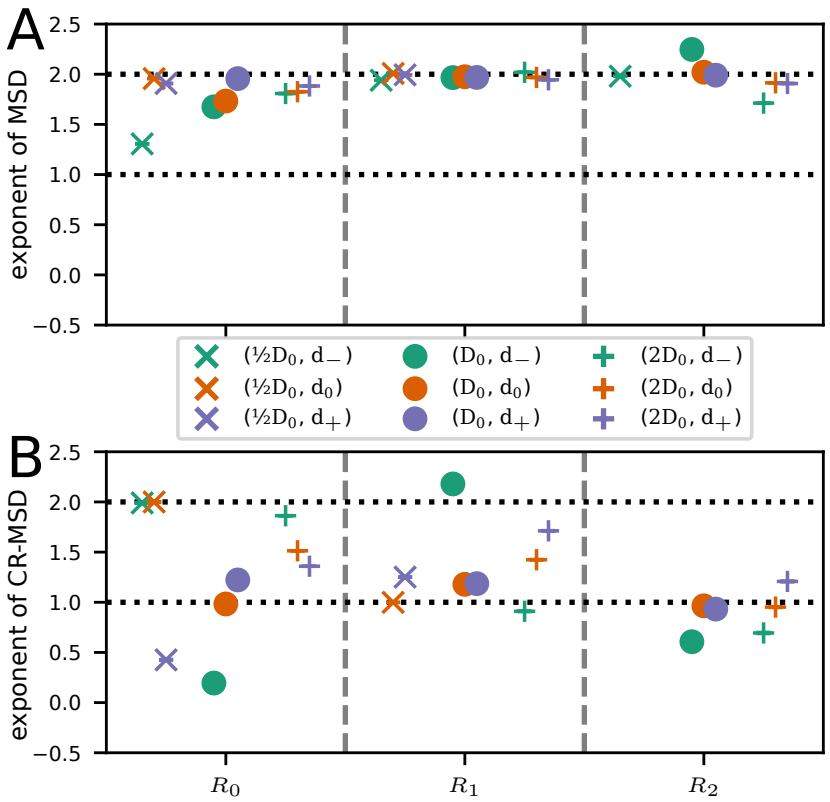


**Figure 20** *Comparison of MSDs in constricted channels of varying width with slender transition.* (A) Exponent from monomial fit to the late MSD for same parameter configurations as in Fig. 19 and separate for regions $R_0$, $R_1$, and $R_2$. (B) Corresponding exponents from monomial fits to the late CR-MSD. Except green cross and the green dot for parameters, the CR-MSD is consistently lower than the ordinary MSD. Missing data in region $R_2$ is because invasion had not progressed significantly far into the region for a sufficiently long time.

## 2.4 Differential adhesion

Higher multicellular living organisms, e.g. humans, consist of cells of different types. The correct arrangement of these different cell types is important for the correct functioning of these organisms and their organs[213, 214, 285]. Various biochemical, genetic, and mechanic mechanisms are involved in the process of forming, maintaining, and restoring these arrangements. One hypothetical mechanism in this context is *differential adhesion* that explains the sorting of cells according to cell type with cell-cell adhesion energies that differ according to which cells are involved[212]. This mechanism can easily be integrated into the CPM.

In our version of the CPM, the constant $B$ controlled the strength of cell-cell adhesion, in the previous study it was set to $B = 10$. To implement differential adhesion between two different cell types, type 0 and type 1, this constant can be generalised to a matrix: $B_{00} = B_{11}$ for common edges between cells of the same type and $B_{01} = B_{10}$ for edges shared between cells of different type. According to the model mechanics, cells should tend to cluster around cells of the same type for $B_{ii} < B_{ij}$ $(i, j = 1, 2)$ for $i \neq j$ and preferably mix for $B_{ii} > B_{ij}$. Snapshots of simulations with $B_{ii} = 10$ and $B_{ij} \in \{5, 10, 20\}$ for $i \neq j$ are shown in Fig. 21. The setup shown corresponds to the straight channel setup considered before with the addition that cells of type 1 are initialised in the top half of the reservoir while cells of type 2 are initialised in the bottom half.

A look at these examples seems to confirm the expectations. For all three cases, cells of type 1 largely stay in the top half of the channel and cells of type 2 in the lower half. For $B_{ij} = 5(i \neq j)$, fewer cells of one type enter the bulk of cells of the other type than in the other examples. Nevertheless, the border between both regions is significantly rugged. In the example for $B_{ij} = 10 \forall i, j$, cell types seemingly blend in a bit more. For this parameter set, cells cannot discern cell types. Finally, choosing $B_{ij} = 20 > B_{ii}(i \neq j)$ apparently leads to significantly enhanced mixing of cells of different type.

This quick test of the implementation of different cell types with cell-type dependend cell-sell adhesion shows that differential adhesion effects can be simulated in the CPM. This opens broad prospects for the application of the CPM in the context of morphogenesis.

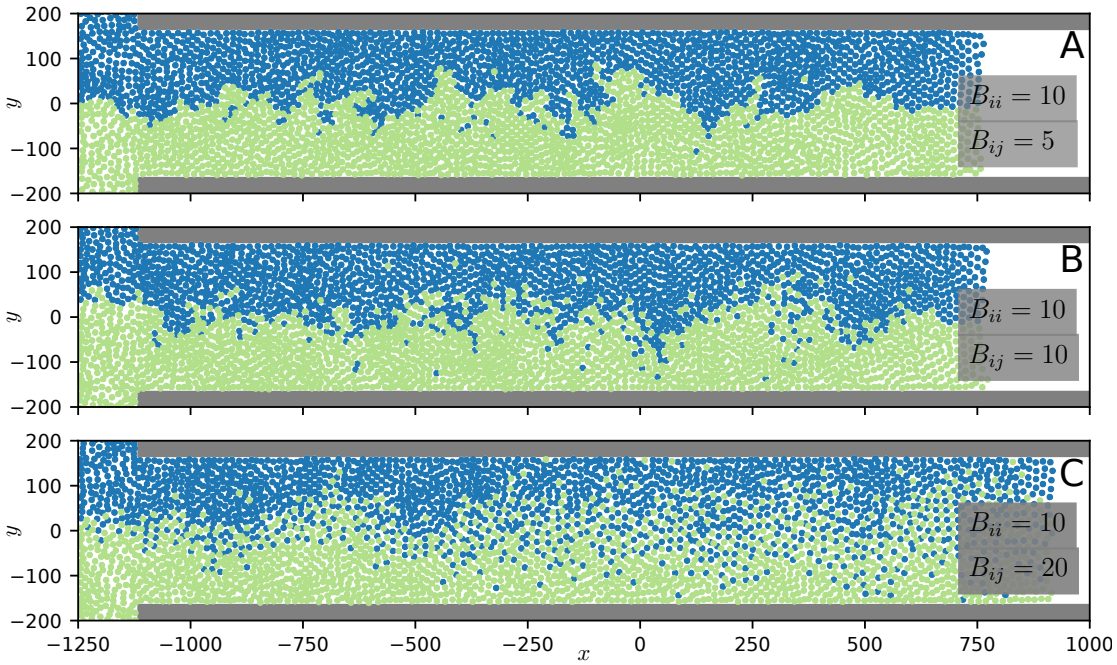


**Figure 21** *Snapshots of a system consisting of two different cell types for varying strength of cell-cell adhesion between different cell types $B_{ij}$.* Cells of one cell type are plotted as blue dots, cells of the other type as green ones. The strenght of adhesion among the same cell types is the same in all three cases: $B_{ii} = 10$. All parameters are the same for both cell types. Cells invade from the reservoir on the left, one type of cells is initialised in the top half of the reservoir, the other one in the lower half. (A) $B_{ij} = 5$, (B) $B_{ij} = 10$, (C) $B_{ij} = 20$. In (B), adhesion is the same regardless of cell types. For lower cross cell-type adhesion (A), less single cells or small groups of cells of one type migrate into the the bulk of the other type, also the interface seems less rough. For the larger value of $B_{ij}$ in C, different cell types clearly mix more.

# 3 Licenses

## 3.1 Royal Society of Chemistry

Copyright permissions from the Royal Society of Chemistry as retrieved from https://www.rsc.org/journals-books-databases/journal-authors-reviewers/licences-copyright-perm on 25/11/2020:

***Author reusing their own work published by the Royal Society of Chemistry***

*You do not need to request permission to reuse your own figures, diagrams, etc, that were originally published in a Royal Society of Chemistry publication. However, permission should be requested for use of the whole article or chapter except if reusing*

*it in a thesis. If you are including an article or book chapter published by us in your thesis please ensure that your co-authors are aware of this.*

*Reuse of material that was published originally by the Royal Society of Chemistry must be accompanied by the appropriate acknowledgement of the publication. The form of the acknowledgement is dependent on the journal in which it was published originally, as detailed in 'Acknowledgements'.*

This applies to the reproduction of [1] in chapter 3.

## 3.2 Springer Nature

Both panels in Figure 4.1 in chapter 4 are reprinted by permission from Springer Nature: "Reale feste und flüssige Körper" by Wolfgang Demtröder © 2015.

License number: 4997760397081, licensee: Felix Kempf, license date: Jan 28, 2021, type of Use: Thesis/Dissertation.

# Bibliography


[1] F. Kempf, R. Mueller, E. Frey, J. M. Yeomans and A. Doostmohammadi. Active matter invasion. *Soft Matter* **15**, 7538–7546, 2019. DOI: 10.1039/C9SM01210A. (Cit. on pp. v, vii, 17, 66, 81, 87, 119).

[2] S. Ramaswamy. The Mechanics and Statistics of Active Matter. *Annual Review of Condensed Matter Physics* **1**(1), 323–345, 2010. DOI: 10.1146/annurev-conmatphys-070909-104101. eprint: https://doi.org/10.1146/annurev-conmatphys-070909-104101. (Cit. on p. 1).

[3] G. Popkin. The physics of life. *Nature* **529**(7688), 16–18, 2016. DOI: 10.1038/529016a. (Cit. on pp. 1, 2).

[4] M. Das, C. F. Schmidt and M. Murrell. Introduction to Active Matter. *Soft Matter* **16**, 7185–7190, 2020. DOI: 10.1039/D0SM90137G. (Cit. on p. 1).

[5] A. P. Deshpande, J. M. Krishnan and S. Kumar. *Active Matter*. Springer-Verlag New York, 2010. Pp. 193–218. DOI: 10.1007/978-1-4419-6494-6. (Cit. on p. 1).

[6] M. C. Marchetti, J. F. Joanny, S. Ramaswamy, T. B. Liverpool, J. Prost, M. Rao and R. A. Simha. Hydrodynamics of soft active matter. *Rev. Mod. Phys.* **85**, 1143–1189, 2013. DOI: 10.1103/RevModPhys.85.1143. (Cit. on p. 1).

[7] C. Bechinger, R. Di Leonardo, H. Löwen, C. Reichhardt, G. Volpe and G. Volpe. Active particles in complex and crowded environments. *Rev. Mod. Phys.* **88**, 045006, 2016. DOI: 10.1103/RevModPhys.88.045006. (Cit. on pp. 1, 2, 6, 12).

[8] D. Needleman and Z. Dogic. Active matter at the interface between materials science and cell biology. *Nature Reviews Materials* **2**(9), 17048, 2017. DOI: 10.1038/natrevmats.2017.48. (Cit. on pp. 1, 12, 61).

[9] G. Gompper *et al.* The 2020 motile active matter roadmap. *Journal of Physics: Condensed Matter* **32**(19), 193001, 2020. DOI: 10.1088/1361-648x/ab6348. (Cit. on p. 1).

[10] P. M. Reis, R. A. Ingale and M. D. Shattuck. Crystallization of a Quasi-Two-Dimensional Granular Fluid. *Phys. Rev. Lett.* **96**, 258001, 2006. DOI: 10.1103/PhysRevLett.96.258001. (Cit. on p. 2).

[11] V. Narayan, S. Ramaswamy and N. Menon. Long-Lived Giant Number Fluctuations in a Swarming Granular Nematic. *Science* **317**(5834), 105–108, 2007. DOI: 10.1126/science.1140414. eprint: https://science.sciencemag.org/content/317/5834/105.full.pdf. (Cit. on p. 2).

[12] H. Chaté, F. Ginelli, G. Grégoire and F. Raynaud. Collective motion of self-propelled particles interacting without cohesion. *Phys. Rev. E* **77**, 046113, 2008. DOI: 10.1103/PhysRevE.77.046113. (Cit. on pp. 2, 13).

[13] A. P. Solon, J.-B. Caussin, D. Bartolo, H. Chaté and J. Tailleur. Pattern formation in flocking models: A hydrodynamic description. *Phys. Rev. E* **92**, 062111, 2015. DOI: 10.1103/PhysRevE.92.062111. (Cit. on p. 2).

[14] D. Geyer, A. Morin and D. Bartolo. Sounds and hydrodynamics of polar active fluids. *Nature Materials* **17**(9), 789–793, 2018. DOI: 10.1038/s41563-018-0123-4. (Cit. on pp. 2, 11).

[15] V. Schaller, C. Weber, E. Frey and A. R. Bausch. Polar pattern formation: hydrodynamic coupling of driven filaments. *Soft Matter* **7**, 3213–3218, 2011. DOI: 10.1039/C0SM01063D. (Cit. on p. 2).

[16] M. E. Cates and J. Tailleur. Motility-Induced Phase Separation. *Annual Review of Condensed Matter Physics* **6**(1), 219–244, 2015. DOI: 10.1146/annurev-conmatphys-031214-014710. (Cit. on pp. 2, 13).

[17] M. Brun-Cosme-Bruny, E. Bertin, B. Coasne, P. Peyla and S. Rafaı. Effective diffusivity of microswimmers in a crowded environment. *J. Chem. Phys.* **150**(10), 104901, 2019. DOI: 10.1063/1.5081507. eprint: https://doi.org/10.1063/1.5081507. (Cit. on pp. 2, 18).

[18] T. Vicsek, A. Czirók, E. Ben-Jacob, I. Cohen and O. Shochet. Novel Type of Phase Transition in a System of Self-Driven Particles. *Phys. Rev. Lett.* **75**, 1226–1229, 1995. DOI: 10.1103/PhysRevLett.75.1226. (Cit. on pp. 2, 10, 13).

[19] J. Toner and Y. Tu. Long-Range Order in a Two-Dimensional Dynamical XY Model: How Birds Fly Together. *Phys. Rev. Lett.* **75**, 4326–4329, 1995. DOI: 10.1103/PhysRevLett.75.4326. (Cit. on pp. 2, 11, 13).

[20] J. Toner and Y. Tu. Flocks, herds, and schools: A quantitative theory of flocking. *Phys. Rev. E* **58**, 4828–4858, 1998. DOI: 10.1103/PhysRevE.58.4828. (Cit. on pp. 2, 11, 13).

[21] J. Toner, Y. Tu and S. Ramaswamy. Hydrodynamics and phases of flocks. *Annals of Physics* **318**(1) Special Issue, 170–244, 2005. DOI: https://doi.org/10.1016/j.aop.2005.04.011. (Cit. on pp. 2, 11, 13).

[22] V. Schaller, C. Weber, C. Semmrich, E. Frey and A. R. Bausch. Polar patterns of driven filaments. *Nature* **467**(7311), 73–77, 2010. DOI: 10.1038/nature09312. (Cit. on pp. 2, 13, 61).

[23] H. Wioland, E. Lushi and R. E. Goldstein. Directed collective motion of bacteria under channel confinement. *New J. Phys.* **18**(7), 075002, 2016. (Cit. on pp. 2, 6, 17).

[24] L. Huber, R. Suzuki, T. Krüger, E. Frey and A. R. Bausch. Emergence of coexisting ordered states in active matter systems. *Science* **361**(6399), 255–258, 2018. DOI: 10.1126/science.aao5434. eprint: https://science.sciencemag.org/content/361/6399/255.full.pdf. (Cit. on pp. 2, 14, 61).

[25] T. E. Angelini, E. Hannezo, X. Trepat, M. Marquez, J. J. Fredberg and D. A. Weitz. Glass-like dynamics of collective cell migration. *Proceedings of the National Academy of Sciences* **108**(12), 4714–4719, 2011. DOI: 10.1073/pnas.1010059108. eprint: https://www.pnas.org/content/108/12/4714.full.pdf. (Cit. on pp. 2, 62, 74, 80).

[26] S. Garcia, E. Hannezo, J. Elgeti, J.-F. Joanny, P. Silberzan and N. S. Gov. Physics of active jamming during collective cellular motion in a monolayer. *Proceedings of the National Academy of Sciences* **112**(50), 15314–15319, 2015. DOI: 10.1073/pnas.1510973112. eprint: https://www.pnas.org/content/112/50/15314.full.pdf. (Cit. on pp. 2, 62, 74, 80).

[27] J.-A. Park *et al.* Unjamming and cell shape in the asthmatic airway epithelium. *Nature Materials* **14**(10), 1040–1048, 2015. DOI: 10.1038/nmat4357. (Cit. on pp. 2, 62, 74, 80).

[28] D. Bi, X. Yang, M. C. Marchetti and M. L. Manning. Motility-Driven Glass and Jamming Transitions in Biological Tissues. *Phys. Rev. X* **6**, 021011, 2016. DOI: 10.1103/PhysRevX.6.021011. (Cit. on pp. 2, 62, 63, 74, 80).

[29] D. M. Sussman, M. Paoluzzi, M. C. Marchetti and M. L. Manning. Anomalous glassy dynamics in simple models of dense biological tissue. *EPL (Europhysics Letters)* **121**(3), 36001, 2018. DOI: 10.1209/0295-5075/121/36001. (Cit. on pp. 2, 62, 63, 74, 80).

[30] T. Sanchez, D. T. N. Chen, S. J. DeCamp, M. Heymann and Z. Dogic. Spontaneous motion in hierarchically assembled active matter. *Nature* **491**(7424), 431–434, 2012. DOI: 10.1038/nature11591. (Cit. on pp. 2, 12, 19, 61).

[31] H. H. Wensink, J. Dunkel, S. Heidenreich, K. Drescher, R. E. Goldstein, H. Löwen and J. M. Yeomans. Meso-scale turbulence in living fluids. *Proc. Natl. Acad. Sci. U. S. A.* **109**(36), 14308–14313, 2012. DOI: 10.1073/pnas.1202032109. eprint: https://www.pnas.org/content/109/36/14308.full.pdf. (Cit. on pp. 2, 11, 18).

[32] F. C. Keber, E. Loiseau, T. Sanchez, S. J. DeCamp, L. Giomi, M. J. Bowick, M. C. Marchetti, Z. Dogic and A. R. Bausch. Topology and dynamics of active nematic vesicles. *Science* **345**(6201), 1135–1139, 2014. DOI: 10.1126/science.1254784. eprint: https://science.sciencemag.org/content/345/6201/1135.full.pdf. (Cit. on pp. 2, 12, 61).

[33] A. Creppy, O. Praud, X. Druart, P. L. Kohnke and F. Plouraboué. Turbulence of swarming sperm. *Phys. Rev. E* **92**, 032722, 2015. DOI: 10.1103/PhysRevE.92.032722. (Cit. on p. 2).

[34] D. Nishiguchi and M. Sano. Mesoscopic turbulence and local order in Janus particles self-propelling under an ac electric field. *Phys. Rev. E* **92**, 052309, 2015. DOI: 10.1103/PhysRevE.92.052309. (Cit. on p. 2).

[35] T. B. Saw, A. Doostmohammadi, V. Nier, L. Kocgozlu, S. Thampi, Y. Toyama, P. Marcq, C. T. Lim, J. M. Yeomans and B. Ladoux. Topological defects in epithelia govern cell death and extrusion. *Nature* **544**, 212–216, 2017. (Cit. on pp. 2, 12, 18, 19, 27, 35, 63, 66).

[36] K.-T. Wu, J. B. Hishamunda, D. T. N. Chen, S. J. DeCamp, Y.-W. Chang, A. Fernández-Nieves, S. Fraden and Z. Dogic. Transition from turbulent to coherent flows in confined three-dimensional active fluids. *Science* **355**(6331), eaal1979, 2017. DOI: 10.1126/science.aal1979. eprint: http://science.sciencemag.org/content/355/6331/eaal1979.full.pdf. (Cit. on pp. 2, 6, 17, 61).

[37] A. Opathalage, M. M. Norton, M. P. N. Juniper, B. Langeslay, S. A. Aghvami, S. Fraden and Z. Dogic. Self-organized dynamics and the transition to turbulence of confined active nematics. *Proc. Natl. Acad. Sci. U. S. A.* **116**(11), 4788–4797, 2019. DOI: 10.1073/pnas.1816733116. eprint: https://www.pnas.org/content/116/11/4788.full.pdf. (Cit. on pp. 2, 6, 12, 17, 61).

[38] P. M. Chaikin and T. Lubensky. *Principles of condensed matter physics*. 6th edition. Cambridge University Press, 2012. (Cit. on pp. 3, 9, 11, 20, 42, 72, 102).

[39] L. Landau and E. Lifshitz. *Fluid Mechanics: Landau and Lifshitz: Course of Theoretical Physics, Volume 6*. v. 6. Elsevier Science, 2013. (Cit. on pp. 3, 70).

[40] M. Kardar. *Statistical Physics of Particles*. Cambridge University Press, 2007. DOI: 10.1017/CBO9780511815898. (Cit. on p. 3).

[41] L. Onsager. Reciprocal Relations in Irreversible Processes. II. *Phys. Rev.* **38**, 2265–2279, 1931. DOI: 10.1103/PhysRev.38.2265. (Cit. on pp. 3, 11, 12).

[42] C. Kittel. *Elementary Statistical Physics*. R.E. Krieger Publishing Company, 1988. (Cit. on pp. 3, 11, 12).

[43] F. S. Gnesotto, F. Mura, J. Gladrow and C. P. Broedersz. Broken detailed balance and non-equilibrium dynamics in living systems: a review. *Reports on Progress in Physics* **81**(6), 066601, 2018. DOI: 10.1088/1361-6633/aab3ed. (Cit. on p. 3).

[44] F. Mura, G. Gradziuk and C. P. Broedersz. Mesoscopic non-equilibrium measures can reveal intrinsic features of the active driving. *Soft Matter* **15**, 8067–8076, 2019. DOI: 10.1039/C9SM01169B. (Cit. on p. 3).

[45] F. S. Gnesotto, G. Gradziuk, P. Ronceray and C. P. Broedersz. Learning the non-equilibrium dynamics of Brownian movies. *Nature Communications* **11**(1), 5378, 2020. DOI: 10.1038/s41467-020-18796-9. (Cit. on p. 3).

[46] U. Seifert. Stochastic thermodynamics, fluctuation theorems and molecular machines. *Reports on Progress in Physics* **75**(12), 126001, 2012. DOI: 10.1088/0034-4885/75/12/126001. (Cit. on p. 3).

[47] R. Wittkowski, A. Tiribocchi, J. Stenhammar, R. J. Allen, D. Marenduzzo and M. E. Cates. Scalar $\phi 4$ field theory for active-particle phase separation. *Nature Communications* **5**(1), 4351, 2014. DOI: 10.1038/ncomms5351. (Cit. on pp. 3, 37, 38).

[48] A. P. Solon, J. Stenhammar, R. Wittkowski, M. Kardar, Y. Kafri, M. E. Cates and J. Tailleur. Pressure and Phase Equilibria in Interacting Active Brownian Spheres. *Phys. Rev. Lett.* **114**, 198301, 2015. DOI: 10.1103/PhysRevLett.114.198301. (Cit. on p. 3).

[49] F. Ginot, I. Theurkauff, D. Levis, C. Ybert, L. Bocquet, L. Berthier and C. Cottin-Bizonne. Nonequilibrium Equation of State in Suspensions of Active Colloids. *Phys. Rev. X* **5**, 011004, 2015. DOI: 10.1103/PhysRevX.5.011004. (Cit. on pp. 3, 37).

[50] S. C. Takatori and J. F. Brady. Forces, stresses and the (thermo?) dynamics of active matter. *Current Opinion in Colloid & Interface Science* **21**, 24–33, 2016. DOI: https://doi.org/10.1016/j.cocis.2015.12.003. (Cit. on p. 3).

[51] C. Nardini, É. Fodor, E. Tjhung, F. van Wijland, J. Tailleur and M. E. Cates. Entropy Production in Field Theories without Time-Reversal Symmetry: Quantifying the Non-Equilibrium Character of Active Matter. *Phys. Rev. X* **7**, 021007, 2017. DOI: 10.1103/PhysRevX.7.021007. (Cit. on p. 3).

[52] A. P. Solon, J. Stenhammar, M. E. Cates, Y. Kafri and J. Tailleur. Generalized thermodynamics of motility-induced phase separation: phase equilibria, Laplace pressure, and change of ensembles. *New Journal of Physics* **20**(7), 075001, 2018. DOI: 10.1088/1367-2630/aaccdd. (Cit. on pp. 3, 13, 37, 38, 59).

[53] U. Seifert. From Stochastic Thermodynamics to Thermodynamic Inference. *Annual Review of Condensed Matter Physics* **10**(1), 171–192, 2019. DOI: 10.1146/annurev-conmatphys-031218-013554. eprint: https://doi.org/10.1146/annurev-conmatphys-031218-013554. (Cit. on p. 3).

[54] E. M. Purcell. Life at low Reynolds number. *American Journal of Physics* **45**(1), 3–11, 1977. DOI: 10.1119/1.10903. eprint: https://doi.org/10.1119/1.10903. (Cit. on pp. 3, 13).

[55] S. E. Luria and M. Delbrück. Mutations of Bacteria from Virus Sensitivity to Virus Resistance. *Genetics* **28**(6) PMC1209226[pmcid], 491–511, 1943. (Cit. on p. 3).

[56] B. Küppers. *Die Berechenbarkeit der Welt: Grenzfragen der exakten Wissenschaften*. Hirzel, 2012. (Cit. on p. 4).

[57] E. Wigner. The Unreasonable Effectiveness of Mathematics in the Natural Sciences. *Communications in Pure and Applied Mathematics* **13**(1), 1960. (Cit. on p. 4).

[58] I. Stewart. The mathematical equation that caused the banks to crash. *The Guardian*, 2012. (Cit. on p. 5).

[59] K. E. Velupillai. The Unreasonable Ineffectiveness of Mathematics in Economics. *Cambridge Journal of Economics* **29**, 849–872, 2005. DOI: 10.1103/PhysRevLett.75.1226. (Cit. on p. 5).

[60] N. N. Taleb. The Black Swan The Impact of the Highly Improbable. *London: Penguin* **36**, 2010. (Cit. on p. 5).

[61] A. Cavagna and I. Giardina. Bird Flocks as Condensed Matter. *Annual Review of Condensed Matter Physics* **5**(1), 183–207, 2014. DOI: 10.1146/annurev-conmatphys-031113-133834. eprint: https://doi.org/10.1146/annurev-conmatphys-031113-133834. (Cit. on pp. 5, 13).

[62] D. Ray, C. Reichhardt and C. J. O. Reichhardt. Casimir effect in active matter systems. *Physical Review E - Statistical, Nonlinear, and Soft Matter Physics* **90**(1), 013019, 2014. DOI: 10.1103/PhysRevE.90.013019. (Cit. on p. 6).

[63] J. Hu, A. Wysocki, R. G. Winkler and G. Gompper. Physical Sensing of Surface Properties by Microswimmers – Directing Bacterial Motion via Wall Slip. *Scientific Reports* **5**(1), 9586, 2015. DOI: 10.1038/srep09586. (Cit. on p. 6).

[64] A. J. T. M. Mathijssen, N. Figueroa-Morales, G. Junot, É. Clément, A. Lindner and A. Zöttl. Oscillatory surface rheotaxis of swimming E. coli bacteria. *Nature Communications* **10**(1), 3434, 2019. DOI: 10.1038/s41467-019-11360-0. (Cit. on pp. 6, 13).

[65] R. Alonso-Matilla, B. Chakrabarti and D. Saintillan. Transport and dispersion of active particles in periodic porous media. *Phys. Rev. Fluids* **4**, 043101, 2019. DOI: 10.1103/PhysRevFluids.4.043101. (Cit. on pp. 6, 18).

[66] M. Brun-Cosme-Bruny, A. Förtsch, W. Zimmermann, E. Bertin, P. Peyla and S. Rafaı. Deflection of phototactic microswimmers through obstacle arrays. *Phys. Rev. Fluids* **5**, 093302, 2020. DOI: 10.1103/PhysRevFluids.5.093302. (Cit. on p. 6).

[67] S. R. K. Vedula, M. C. Leong, T. L. Lai, P. Hersen, A. J. Kabla, C. T. Lim and B. Ladoux. Emerging modes of collective cell migration induced by geometrical constraints. *Proc. Natl. Acad. Sci. U. S. A.* **109**(32), 12974–12979, 2012. DOI: 10.1073/pnas.1119313109. eprint: http://www.pnas.org/content/109/32/12974.full.pdf. (Cit. on pp. 6, 17, 18, 22, 63, 65, 81).

[68] A. K. Marel, M. Zorn, C. Klingner, R. Wedlich-Söldner, E. Frey and J. O. Rädler. Flow and diffusion in channel-guided cell migration. *Biophys. J.* **107**(5), 1054–1064, 2014. DOI: 10.1016/j.bpj.2014.07.017. (Cit. on pp. 6, 17, 22, 63, 65, 81).

[69] A.-K. Marel, N. Podewitz, M. Zorn, J. O. Rädler and J. Elgeti. Alignment of cell division axes in directed epithelial cell migration. *New J. Phys.* **16**(11), 115005, 2014. (Cit. on pp. 6, 17, 22, 65, 81).

[70] Y. Yang, N. Jamilpour, B. Yao, Z. S. Dean, R. Riahi and P. K. Wong. Probing Leader Cells in Endothelial Collective Migration by Plasma Lithography Geometric Confinement. *Scientific Reports* **6**(1), 22707, 2016. DOI: 10.1038/srep22707. (Cit. on pp. 6, 17, 22, 63, 65, 81).

[71] E. Gauquelin, S. Tlili, C. Gay, G. Peyret, R.-M. Mège, M. A. Fardin and B. Ladoux. Influence of proliferation on the motions of epithelial monolayers invading adherent strips. *Soft Matter* **15**, 2798–2810, 2019. DOI: 10.1039/C9SM00105K. (Cit. on pp. 6, 17, 22, 63, 65, 81).

[72] G. Duclos, C. Erlenkämper, J.-F. Joanny and P. Silberzan. Topological defects in confined populations of spindle-shaped cells. *Nat. Phys.* **13**, 58–62, 2017. (Cit. on pp. 6, 17, 35).

[73] G. Duclos, C. Blanch-Mercader, V. Yashunsky, G. Salbreux, J.-F. Joanny, J. Prost and P. Silberzan. Spontaneous shear flow in confined cellular nematics. *Nat. Phys.* **14**(7), 728–732, 2018. DOI: 10.1038/s41567-018-0099-7. (Cit. on pp. 6, 17, 66).

[74] S. Tlili, E. Gauquelin, B. Li, O. Cardoso, B. Ladoux, H. Delanoë-Ayari and F. Graner. Collective cell migration without proliferation: density determines cell velocity and wave velocity. *Royal Society Open Science* **5**(5), 172421, 2018. DOI: 10.1098/rsos.172421. eprint: https://royalsocietypublishing.org/doi/pdf/10.1098/rsos.172421. (Cit. on pp. 6, 63, 65, 81).

[75] H. Wioland, F. G. Woodhouse, J. Dunkel, J. O. Kessler and R. E. Goldstein. Confinement Stabilizes a Bacterial Suspension into a Spiral Vortex. *Phys. Rev. Lett.* **110**, 268102, 2013. DOI: 10.1103/PhysRevLett.110.268102. (Cit. on pp. 6, 17).

[76] J. C. Conrad and R. Poling-Skutvik. Confined Flow: Consequences and Implications for Bacteria and Biofilms. *Annu. Rev. Chem. Biomol. Eng.* **9**(1) PMID: 29561646, 175–200, 2018. DOI: 10.1146/annurev-chembioeng-060817-084006. eprint: https://doi.org/10.1146/annurev-chembioeng-060817-084006. (Cit. on pp. 6, 17).

[77] K. Suzuki, M. Miyazaki, J. Takagi, T. Itabashi and S. Ishiwata. Spatial confinement of active microtubule networks induces large-scale rotational cytoplasmic flow. *Proc. Natl. Acad. Sci. U. S. A.* **114**(11), 2922–2927, 2017. DOI: 10.1073/pnas.1616001114. eprint: http://www.pnas.org/content/114/11/2922.full.pdf. (Cit. on pp. 6, 17).

[78] J. Hardoüin, R. Hughes, A. Doostmohammadi, J. Laurent, T. Lopez-Leon, J. M. Yeomans, J. Ignés-Mullol and F. Sagués. Reconfigurable Flows and Defect Landscape of Confined Active Nematics. arXiv:1903.01787, 2019. (Cit. on pp. 6, 17).

[79] F. J. Segerer, F. Thüroff, A. Piera Alberola, E. Frey and J. O. Rädler. Emergence and Persistence of Collective Cell Migration on Small Circular Micropatterns. *Phys. Rev. Lett.* **114**, 228102, 2015. DOI: 10.1103/PhysRevLett.114.228102. (Cit. on pp. 6, 67, 85).

[80] P. G. Gritsenko, O. Ilina and P. Friedl. Interstitial guidance of cancer invasion. *The Journal of Pathology* **226**(2), 185–199, 2011. DOI: 10.1002/path.3031. eprint: https://onlinelibrary.wiley.com/doi/pdf/10.1002/path.3031. (Cit. on pp. 6, 17).

[81] B. Weigelin, G.-J. Bakker and P. Friedl. Intravital third harmonic generation microscopy of collective melanoma cell invasion. *IntraVital* **1**(1), 32–43, 2012. DOI: 10.4161/intv.21223. eprint: https://doi.org/10.4161/intv.21223. (Cit. on pp. 6, 17).

[82] L. Hall-Stoodley, J. W. Costerton and P. Stoodley. Bacterial biofilms: from the Natural environment to infectious diseases. *Nat. Rev. Microbiol.* **2** Review Article, 95–108, 2004. (Cit. on pp. 6, 17).

[83] J. C. Conrad and R. Poling-Skutvik. Confined Flow: Consequences and Implications for Bacteria and Biofilms. *Annu. Rev. Chem. Biomol. Eng.* **9**, 175–200, 2018. (Cit. on pp. 6, 17).

[84] A. G. Clark and D. M. Vignjevic. Modes of cancer cell invasion and the role of the microenvironment. *Curr. Opin. Cell Biol.* **36**, 13–22, 2015. (Cit. on pp. 6, 17, 65).

[85] P. Friedl and D. Gilmour. Collective cell migration in morphogenesis, regeneration and cancer. *Nature Reviews Molecular Cell Biology* **10**(7), 445–457, 2009. DOI: 10.1038/nrm2720. (Cit. on pp. 6, 61, 65).

[86] P. Friedl and S. Alexander. Cancer Invasion and the Microenvironment: Plasticity and Reciprocity. *Cell* **147**(5), 992–1009, 2011. DOI: 10.1016/j.cell.2011.11.016. (Cit. on pp. 6, 65, 81).

[87] Y. Wu. Collective motion of bacteria in two dimensions. *Quant. Biol.* **3**, 199–205, 2015. (Cit. on pp. 6, 17, 85).

[88] C. Even, C. Marlière, J.-M. Ghigo, J.-M. Allain, A. Marcellan and E. Raspaud. Recent advances in studying single bacteria and biofilm mechanics. *Adv. Colloid Interface Sci.* **247**, 573–588, 2017. (Cit. on pp. 6, 17, 85).

[89] R. Hartmann, P. K. Singh, P. Pearce, R. Mok, B. Song, F. Dıaz-Pascual, J. Dunkel and K. Drescher. Emergence of three-dimensional order and structure in growing biofilms. *Nat. Phys.* **15**, 251–256, 2018. (Cit. on pp. 6, 17, 85).

[90] N. Murisic, V. Hakim, I. G. Kevrekidis, S. Y. Shvartsman and B. Audoly. From Discrete to Continuum Models of Three-Dimensional Deformations in Epithelial Sheets. *Biophysical Journal* **109**(1), 154–163, 2015. DOI: https://doi.org/10.1016/j.bpj.2015.05.019. (Cit. on p. 10).

[91] S. Ishihara, P. Marcq and K. Sugimura. From cells to tissue: A continuum model of epithelial mechanics. *Phys. Rev. E* **96**, 022418, 2017. DOI: 10.1103/PhysRevE.96.022418. (Cit. on pp. 10, 63, 66).

[92] É. Fodor and M. C. Marchetti. The statistical physics of active matter: From self-catalytic colloids to living cells. *Physica A: Statistical Mechanics and its Applications* **504** Lecture Notes of the 14th International Summer School on Fundamental Problems in Statistical Physics, 106–120, 2018. DOI: https://doi.org/10.1016/j.physa.2017.12.137. (Cit. on pp. 10, 12).

[93] R. Mueller, J. M. Yeomans and A. Doostmohammadi. Emergence of Active Nematic Behavior in Monolayers of Isotropic Cells. *Phys. Rev. Lett.* **122**, 048004, 2019. DOI: 10.1103/PhysRevLett.122.048004. (Cit. on pp. 10, 15, 35, 65).

[94] M. R. Shaebani, A. Wysocki, R. G. Winkler, G. Gompper and H. Rieger. Computational models for active matter. *Nature Reviews Physics* **2**(4), 181–199, 2020. DOI: 10.1038/s42254-020-0152-1. (Cit. on pp. 10, 13, 61, 63).

[95] M. E. Cates. *Active Field Theories*. 2019. arXiv: 1904.01330 [cond-mat.stat-mech] (cit. on p. 11).

[96] V. Bratanov, F. Jenko and E. Frey. New class of turbulence in active fluids. *Proc. Natl. Acad. Sci. U. S. A.* **112**(49), 15048–15053, 2015. DOI: 10.1073/pnas.1509304112. eprint: https://www.pnas.org/content/112/49/15048.full.pdf. (Cit. on pp. 11, 18).

[97] J. Dunkel, S. Heidenreich, K. Drescher, H. H. Wensink, M. Bär and R. E. Goldstein. Fluid Dynamics of Bacterial Turbulence. *Phys. Rev. Lett.* **110**, 228102, 2013. DOI: 10.1103/PhysRevLett.110.228102. (Cit. on p. 11).

[98] A. Tiribocchi, R. Wittkowski, D. Marenduzzo and M. E. Cates. Active Model H: Scalar Active Matter in a Momentum-Conserving Fluid. *Phys. Rev. Lett.* **115**, 188302, 2015. DOI: 10.1103/PhysRevLett.115.188302. (Cit. on pp. 11, 37, 38).

[99] I. S. Aranson and L. S. Tsimring. Theory of self-assembly of microtubules and motors. *Phys. Rev. E* **74**, 031915, 2006. DOI: 10.1103/PhysRevE.74.031915. (Cit. on pp. 11, 84).

[100] E. Bertin, M. Droz and G. Grégoire. Boltzmann and hydrodynamic description for self-propelled particles. *Phys. Rev. E* **74**, 022101, 2006. DOI: 10.1103/PhysRevE.74.022101. (Cit. on pp. 11, 84).

[101] E. Bertin, M. Droz and G. Grégoire. Hydrodynamic equations for self-propelled particles: microscopic derivation and stability analysis. *Journal of Physics A: Mathematical and Theoretical* **42**(44), 445001, 2009. DOI: 10.1088/1751-8113/42/44/445001. (Cit. on pp. 11, 84).

[102] A. Peshkov, E. Bertin, F. Ginelli and H. Chaté. Boltzmann-Ginzburg-Landau approach for continuous descriptions of generic Vicsek-like models. *The European Physical Journal Special Topics* **223**(7), 1315–1344, 2014. DOI: 10.1140/epjst/e2014-02193-y. (Cit. on p. 11).

[103] E. Bertin, A. Baskaran, H. Chaté and M. C. Marchetti. Comparison between Smoluchowski and Boltzmann approaches for self-propelled rods. *Phys. Rev. E* **92**, 042141, 2015. DOI: 10.1103/PhysRevE.92.042141. (Cit. on p. 11).

[104] A. P. Solon, M. E. Cates and J. Tailleur. Active brownian particles and run-and-tumble particles: A comparative study. *The European Physical Journal Special Topics* **224**(7), 1231–1262, 2015. DOI: 10.1140/epjst/e2015-02457-0. (Cit. on pp. 11, 13, 84).

[105] I. Maryshev, D. Marenduzzo, A. B. Goryachev and A. Morozov. Kinetic theory of pattern formation in mixtures of microtubules and molecular motors. *Phys. Rev. E* **97**, 022412, 2018. DOI: 10.1103/PhysRevE.97.022412. (Cit. on pp. 11, 84).

[106] I. Maryshev, A. B. Goryachev, D. Marenduzzo and A. Morozov. Dry active turbulence in a model for microtubule–motor mixtures. *Soft Matter* **15**, 6038–6043, 2019. DOI: 10.1039/C9SM00558G. (Cit. on pp. 11, 84).

[107] F. Thüroff, C. A. Weber and E. Frey. Numerical Treatment of the Boltzmann Equation for Self-Propelled Particle Systems. *Phys. Rev. X* **4**, 041030, 2014. DOI: 10.1103/PhysRevX.4.041030. (Cit. on p. 11).

[108] J. Denk and E. Frey. Pattern-induced local symmetry breaking in active-matter systems. *Proceedings of the National Academy of Sciences* **117**(50), 31623–31630, 2020. DOI: 10.1073/pnas.2010302117. eprint: https://www.pnas.org/content/117/50/31623.full.pdf. (Cit. on p. 11).

[109] K. Kruse, J. F. Joanny, F. Jülicher, J. Prost and K. Sekimoto. Asters, Vortices, and Rotating Spirals in Active Gels of Polar Filaments. *Phys. Rev. Lett.* **92**, 078101, 2004. DOI: 10.1103/PhysRevLett.92.078101. (Cit. on p. 11).

[110] F. Jülicher, S. W. Grill and G. Salbreux. Hydrodynamic theory of active matter. *Reports on Progress in Physics* **81**(7), 076601, 2018. DOI: 10.1088/1361-6633/aab6bb. (Cit. on pp. 11, 12).

[111] L. Giomi, L. Mahadevan, B. Chakraborty and M. F. Hagan. Banding, excitability and chaos in active nematic suspensions. *Nonlinearity* **25**(8), 2245–2269, 2012. DOI: 10.1088/0951-7715/25/8/2245. (Cit. on p. 12).

[112] M. L. Blow, S. P. Thampi and J. M. Yeomans. Biphasic, Lyotropic, Active Nematics. *Phys. Rev. Lett.* **113**, 248303, 2014. DOI: 10.1103/PhysRevLett.113.248303. (Cit. on pp. 12, 19, 22, 24, 39, 40, 49, 59).

[113] S. P. Thampi, A. Doostmohammadi, R. Golestanian and J. M. Yeomans. Intrinsic free energy in active nematics. *EPL* **112**(2), 28004, 2015. (Cit. on pp. 12, 29).

[114] J. M. Yeomans. The hydrodynamics of active systems. *La Rivista del Nuovo Cimento* **40**(1), 1–31, 2017. DOI: 10.1393/ncr/i2016-10131-5. (Cit. on p. 12).

[115] D. Dell'Arciprete, M. L. Blow, A. T. Brown, F. D. C. Farrell, J. S. Lintuvuori, A. F. McVey, D. Marenduzzo and W. C. K. Poon. A growing bacterial colony in two dimensions as an active nematic. *Nature Communications* **9**(1), 4190, 2018. DOI: 10.1038/s41467-018-06370-3. (Cit. on p. 12).

[116] T. B. Saw, W. Xi, B. Ladoux and C. T. Lim. Biological Tissues as Active Nematic Liquid Crystals. *Advanced Materials* **30**(47), 1802579, 2018. DOI: https://doi.org/10.1002/adma.201802579. eprint: https://onlinelibrary.wiley.com/doi/pdf/10.1002/adma.201802579. (Cit. on pp. 12, 63, 66).

[117] A. Doostmohammadi, J. Ignés-Mullol, J. M. Yeomans and F. Sagués. Active nematics. *Nat. Commun.* **9**(1), 3246, 2018. DOI: 10.1038/s41467-018-05666-8. (Cit. on pp. 12, 19, 63, 66).

[118] L. Giomi, M. J. Bowick, X. Ma and M. C. Marchetti. Defect Annihilation and Proliferation in Active Nematics. *Phys. Rev. Lett.* **110**, 228101, 2013. DOI: 10.1103/PhysRevLett.110.228101. (Cit. on pp. 12, 18, 19).

[119] L. Giomi, M. J. Bowick, P. Mishra, R. Sknepnek and M. C. Marchetti. Defect dynamics in active nematics. *Philos. Trans. R. Soc., A* **372**(2029), 20130365, 2014. DOI: 10.1098/rsta.2013.0365. eprint: https://royalsocietypublishing.org/doi/pdf/10.1098/rsta.2013.0365. (Cit. on pp. 12, 18).

[120] S. P. Thampi, R. Golestanian and J. M. Yeomans. Vorticity, defects and correlations in active turbulence. *Philos. Trans. R. Soc., A* **372**(2029), 20130366, 2014. DOI: 10.1098/rsta.2013.0366. eprint: https://royalsocietypublishing.org/doi/pdf/10.1098/rsta.2013.0366. (Cit. on pp. 12, 18, 19, 24).

[121] S. J. DeCamp, G. S. Redner, A. Baskaran, M. F. Hagan and Z. Dogic. Orientational order of motile defects in active nematics. *Nature Materials* **14**(11), 1110–1115, 2015. DOI: 10.1038/nmat4387. (Cit. on pp. 12, 19).

[122] A. Doostmohammadi, M. F. Adamer, S. P. Thampi and J. M. Yeomans. Stabilization of active matter by flow-vortex lattices and defect ordering. *Nature Communications* **7**(1), 10557, 2016. DOI: 10.1038/ncomms10557. (Cit. on p. 12).

[123] T. N. Shendruk, A. Doostmohammadi, K. Thijssen and J. M. Yeomans. Dancing disclinations in confined active nematics. *Soft Matter* **13**, 3853–3862, 2017. DOI: 10.1039/C6SM02310J. (Cit. on pp. 12, 19, 24, 27, 66).

[124] K. Thijssen and A. Doostmohammadi. Binding self-propelled topological defects in active turbulence. *Phys. Rev. Research* **2**, 042008, 2020. DOI: 10.1103/PhysRevResearch.2.042008. (Cit. on p. 12).

[125] L. Giomi. Geometry and Topology of Turbulence in Active Nematics. *Phys. Rev. X* **5**, 031003, 2015. DOI: 10.1103/PhysRevX.5.031003. (Cit. on pp. 12, 18, 19).

[126] A. Doostmohammadi, T. N. Shendruk, K. Thijssen and J. M. Yeomans. Onset of meso-scale turbulence in active nematics. *Nat. Commun.* **8** Article, 15326, 2017. (Cit. on pp. 12, 19, 24, 27).

[127] R. Alert, J.-F. Joanny and J. Casademunt. Universal scaling of active nematic turbulence. *Nature Physics* **16**(6), 682–688, 2020. DOI: 10.1038/s41567-020-0854-4. (Cit. on p. 12).

[128] P. Romanczuk, M. Bär, W. Ebeling, B. Lindner and L. Schimansky-Geier. Active Brownian particles. *The European Physical Journal Special Topics* **202**(1), 1–162, 2012. DOI: 10.1140/epjst/e2012-01529-y. (Cit. on p. 12).

[129] J. U. Klamser, S. C. Kapfer and W. Krauth. Thermodynamic phases in two-dimensional active matter. *Nature Communications* **9**(1), 5045, 2018. DOI: 10.1038/s41467-018-07491-5. (Cit. on p. 13).

[130] X.-q. Shi and Y.-q. Ma. Topological structure dynamics revealing collective evolution in active nematics. *Nature Communications* **4**(1), 3013, 2013. DOI: 10.1038/ncomms4013. (Cit. on p. 13).

[131] J. Stenhammar, D. Marenduzzo, R. J. Allen and M. E. Cates. Phase behaviour of active Brownian particles: the role of dimensionality. *Soft Matter* **10**, 1489–1499, 2014. DOI: 10.1039/C3SM52813H. (Cit. on p. 13).

[132] J. Bialké, J. T. Siebert, H. Löwen and T. Speck. Negative Interfacial Tension in Phase-Separated Active Brownian Particles. *Phys. Rev. Lett.* **115**, 098301, 2015. DOI: 10.1103/PhysRevLett.115.098301. (Cit. on pp. 13, 37, 38).

[133] A. Patch, D. M. Sussman, D. Yllanes and M. C. Marchetti. Curvature-dependent tension and tangential flows at the interface of motility-induced phases. *Soft Matter* **14**, 7435–7445, 2018. DOI: 10.1039/C8SM00899J. (Cit. on pp. 13, 37, 38, 59).

[134] J. Elgeti, R. G. Winkler and G. Gompper. Physics of microswimmers—single particle motion and collective behavior: a review. *Reports on Progress in Physics* **78**(5), 056601, 2015. DOI: 10.1088/0034-4885/78/5/056601. (Cit. on p. 13).

[135] J. Blaschke, M. Maurer, K. Menon, A. Zöttl and H. Stark. Phase separation and coexistence of hydrodynamically interacting microswimmers. *Soft Matter* **12**, 9821–9831, 2016. DOI: 10.1039/C6SM02042A. (Cit. on p. 13).

[136] A. M. Maier, C. Weig, P. Oswald, E. Frey, P. Fischer and T. Liedl. Magnetic Propulsion of Microswimmers with DNA-Based Flagellar Bundles. *Nano Letters* **16**(2), 906–910, 2016. DOI: 10.1021/acs.nanolett.5b03716. (Cit. on p. 13).

[137] R. G. Winkler and G. Gompper. *Hydrodynamics in Motile Active Matter*. Ed. by W. Andreoni and S. Yip. Springer International Publishing, Cham, 2018. Pp. 1–21. DOI: 10.1007/978-3-319-42913-7_35-1. (Cit. on p. 13).

[138] C. A. Weber, V. Schaller, A. R. Bausch and E. Frey. Nucleation-induced transition to collective motion in active systems. *Phys. Rev. E* **86**, 030901, 2012. DOI: 10.1103/PhysRevE.86.030901. (Cit. on p. 13).

[139] B. A. Camley and W.-J. Rappel. Physical models of collective cell motility: from cell to tissue. *Journal of Physics D: Applied Physics* **50**(11), 113002, 2017. DOI: 10.1088/1361-6463/aa56fe. (Cit. on pp. 14, 63).

[140] P. J. Albert and U. S. Schwarz. Dynamics of Cell Ensembles on Adhesive Micropatterns: Bridging the Gap between Single Cell Spreading and Collective Cell Migration. *PLOS Computational Biology* **12**(4), 1–34, 2016. DOI: 10.1371/journal.pcbi.1004863. (Cit. on pp. 14, 65).

[141] M. Chiang and D. Marenduzzo. Glass transitions in the cellular Potts model. *EPL (Europhysics Letters)* **116**(2), 28009, 2016. DOI: 10.1209/0295-5075/116/28009. (Cit. on pp. 14, 65).

[142] F. Thüroff, A. Goychuk, M. Reiter and E. Frey. Bridging the gap between single-cell migration and collective dynamics. *eLife* **8**, e46842, 2019. DOI: 10.7554/eLife.46842. (Cit. on pp. 14, 65, 67, 78, 96–98).

[143] I. Singer-Loginova and H. M. Singer. The phase field technique for modeling multiphase materials. *Reports on Progress in Physics* **71**(10), 106501, 2008. DOI: 10.1088/0034-4885/71/10/106501. (Cit. on p. 15).

[144] I. S. Aranson. *Physical Models of Cell Motility*. Springer, Cham, 2016. DOI: 10.1007/978-3-319-24448-8. (Cit. on pp. 15, 65).

[145] S. Najem and M. Grant. Phase-field model for collective cell migration. *Phys. Rev. E* **93**, 052405, 2016. DOI: 10.1103/PhysRevE.93.052405. (Cit. on pp. 15, 66).

[146] F. Ziebert and I. S. Aranson. Computational approaches to substrate-based cell motility. *npj Computational Materials* **2**(1), 16019, 2016. DOI: 10.1038/npjcompumats.2016.19. (Cit. on pp. 15, 66).

[147] R. Alert and X. Trepat. Physical Models of Collective Cell Migration. *Annual Review of Condensed Matter Physics* **11**(1), 77–101, 2020. DOI: 10.1146/annurev-conmatphys-031218-013516. eprint: https://doi.org/10.1146/annurev-conmatphys-031218-013516. (Cit. on pp. 15, 63, 65, 66).

[148] W. Marth and A. Voigt. Collective migration under hydrodynamic interactions: a computational approach. *Interface Focus* **6**(5), 20160037, 2016. DOI: 10.1098/rsfs.2016.0037. eprint: https://royalsocietypublishing.org/doi/pdf/10.1098/rsfs.2016.0037. (Cit. on p. 15).

[149] D. Wenzel, S. Praetorius and A. Voigt. Topological and geometrical quantities in active cellular structures. *The Journal of Chemical Physics* **150**(16), 164108, 2019. DOI: 10.1063/1.5085766. (Cit. on p. 15).

[150] G. Peyret, R. Mueller, J. d'Alessandro, S. Begnaud, P. Marcq, R.-M. Mège, J. M. Yeomans, A. Doostmohammadi and B. Ladoux. Sustained Oscillations of Epithelial Cell Sheets. *Biophysical Journal* **117**(3), 464–478, 2019. DOI: 10.1016/j.bpj.2019.06.013. (Cit. on pp. 15, 66).

[151] R. Staneva, F. El Marjou, J. Barbazan, D. Krndija, S. Richon, A. Clark and D. M. Vignjevic. Cancer cells in the tumor core exhibit spatially coordinated migration patterns. *J. Cell Sci.* **132**(6), jcs.220277, 2019. DOI: 10.1242/jcs.220277. eprint: http://jcs.biologists.org/content/early/2019/02/11/jcs.220277.full.pdf. (Cit. on p. 17).

[152] C. Yang, H. Chen, G. Zeng, G. Yu and S. Luo. Biomass accumulation and control strategies in gas biofiltration. *Biotechnol. Adv.* **28**(4), 531–540, 2010. DOI: https://doi.org/10.1016/j.biotechadv.2010.04.002. (Cit. on p. 17).

[153] M. James, W. J. T. Bos and M. Wilczek. Turbulence and turbulent pattern formation in a minimal model for active fluids. *Phys. Rev. Fluids* **3**, 061101, 2018. DOI: 10.1103/PhysRevFluids.3.061101. (Cit. on p. 18).

[154] J. Elgeti, M. E. Cates and D. Marenduzzo. Defect hydrodynamics in 2D polar active fluids. *Soft Matter* **7**, 3177–3185, 2011. DOI: 10.1039/C0SM01097A. (Cit. on p. 18).

[155] V. Tarle, E. Gauquelin, S. R. K. Vedula, J. D'Alessandro, C. T. Lim, B. Ladoux and N. S. Gov. Modeling collective cell migration in geometric confinement. *Phys. Biol.* **14**(3), 035001, 2017. (Cit. on pp. 18, 35, 63, 65, 66, 81).

[156] D. Marenduzzo, E. Orlandini, M. E. Cates and J. M. Yeomans. Steady-state hydrodynamic instabilities of active liquid crystals: Hybrid lattice Boltzmann simulations. *Phys. Rev. E* **76**, 031921, 2007. DOI: 10.1103/PhysRevE.76.031921. (Cit. on pp. 19, 26).

[157] R. Aditi Simha and S. Ramaswamy. Hydrodynamic Fluctuations and Instabilities in Ordered Suspensions of Self-Propelled Particles. *Phys. Rev. Lett.* **89**, 058101, 2002. DOI: 10.1103/PhysRevLett.89.058101. (Cit. on p. 19).

[158] S. P. Thampi, R. Golestanian and J. M. Yeomans. Velocity Correlations in an Active Nematic. *Phys. Rev. Lett.* **111**, 118101, 2013. DOI: 10.1103/PhysRevLett.111.118101. (Cit. on p. 19).

[159] D. Cortese, J. Eggers and T. B. Liverpool. Pair creation, motion, and annihilation of topological defects in two-dimensional nematic liquid crystals. *Phys. Rev. E* **97**, 022704, 2018. DOI: 10.1103/PhysRevE.97.022704. (Cit. on p. 19).

[160] T. Bittig, O. Wartlick, A. Kicheva, M. González-Gaitán and F. Jülicher. Dynamics of anisotropic tissue growth. *New J. Phys.* **10**(6), 063001, 2008. (Cit. on p. 19).

[161] G. Duclos, S. Garcia, H. G. Yevick and P. Silberzan. Perfect nematic order in confined monolayers of spindle-shaped cells. *Soft Matter* **10**, 2346–2353, 2014. DOI: 10.1039/C3SM52323C. (Cit. on pp. 19, 35).

[162] A. Doostmohammadi, S. P. Thampi, T. B. Saw, C. T. Lim, B. Ladoux and J. M. Yeomans. Celebrating Soft Matter's 10th Anniversary: Cell division: a source of active stress in cellular monolayers. *Soft Matter* **11**, 7328–7336, 2015. DOI: 10.1039/C5SM01382H. (Cit. on pp. 19, 24).

[163] D. Volfson, S. Cookson, J. Hasty and L. S. Tsimring. Biomechanical ordering of dense cell populations. *Proc. Natl. Acad. Sci. U. S. A.* **105**(40), 15346–15351, 2008. DOI: 10.1073/pnas.0706805105. eprint: http://www.pnas.org/content/105/40/15346.full.pdf. (Cit. on pp. 19, 35, 85).

[164] R. Voituriez, J. F. Joanny and J. Prost. Spontaneous flow transition in active polar gels. *EPL* **70**(3), 404, 2005. (Cit. on pp. 19, 26, 33).

[165] S. A. Edwards and J. M. Yeomans. Spontaneous flow states in active nematics: A unified picture. *EPL* **85**(1), 18008, 2009. (Cit. on pp. 19, 33).

[166] M. M. Norton, A. Baskaran, A. Opathalage, B. Langeslay, S. Fraden, A. Baskaran and M. F. Hagan. Insensitivity of active nematic liquid crystal dynamics to topological constraints. *Phys. Rev. E* **97**, 012702, 2018. DOI: 10.1103/PhysRevE.97.012702. (Cit. on p. 19).

[167] P. G. de Gennes and J. Prost. *The Physics of Liquid Crystals*. Oxford University Press, Oxford, 1995. (Cit. on p. 19).

[168] E. Orlandini, M. R. Swift and J. M. Yeomans. A Lattice Boltzmann Model of Binary-Fluid Mixtures. *EPL* **32**(6), 463, 1995. (Cit. on pp. 20, 26, 42).

[169] R. G. Larson. *The structure and rheology of complex fluids*. Oxford University Press, New York (N.Y.), 1999. (Cit. on p. 21).

[170] S. Ramaswamy. The mechanics and statistics of active matter. *Annu. Rev. Condens. Matter Phys.* **1**, 323–345, 2010. (Cit. on p. 22).

[171] N. S. Rossen, J. M. Tarp, J. Mathiesen, M. H. Jensen and L. B. Oddershede. Long-range ordered vorticity patterns in living tissue induced by cell division. *Nat. Commun.* **5** Article, 5720, 2014. (Cit. on p. 24).

[172] A. Doostmohammadi, M. F. Adamer, S. P. Thampi and J. M. Yeomans. Stabilization of active matter by flow-vortex lattices and defect ordering. *Nat. Commun.* **7**, 10557, 2016. (Cit. on p. 24).

[173] E. J. Hemingway, P. Mishra, M. C. Marchetti and S. M. Fielding. Correlation lengths in hydrodynamic models of active nematics. *Soft Matter* **12**, 7943–7952, 2016. DOI: 10.1039/C6SM00812G. (Cit. on p. 24).

[174] P. Guillamat, J. Ignés-Mullol and F. Sagués. Taming active turbulence with patterned soft interfaces. *Nat. Commun.* **8**, 564, 2017. (Cit. on p. 24).

[175] E. Putzig and A. Baskaran. Phase separation and emergent structures in an active nematic fluid. *Phys. Rev. E* **90**, 042304, 2014. DOI: 10.1103/PhysRevE.90.042304. (Cit. on p. 27).

[176] M. Theillard, R. Alonso-Matilla and D. Saintillan. Geometric control of active collective motion. *Soft Matter* **13**, 363–375, 2017. (Cit. on p. 27).

[177] H. Li, X.-q. Shi, M. Huang, X. Chen, M. Xiao, C. Liu, H. Chaté and H. P. Zhang. Data-driven quantitative modeling of bacterial active nematics. *Proc. Natl. Acad. Sci. U. S. A.* **116**(3), 777–785, 2019. DOI: 10.1073/pnas.1812570116. eprint: https://www.pnas.org/content/116/3/777.full.pdf. (Cit. on pp. 35, 85).

[178] H. Gruler, U. Dewald and M. Eberhardt. Nematic liquid crystals formed by living amoeboid cells. *Euro. Phys. J. B* **11**, 187–192, 1999. (Cit. on p. 35).

[179] C. Blanch-Mercader, V. Yashunsky, S. Garcia, G. Duclos, L. Giomi and P. Silberzan. Turbulent dynamics of epithelial cell cultures. *Phys. Rev. Lett.* **120**, 208101, 2018. (Cit. on p. 35).

[180] K. Kawaguchi, R. Kageyama and M. Sano. Topological defects control collective dynamics in neural progenitor cell cultures. *Nature* **545**, 327–331, 2017. (Cit. on p. 35).

[181] T. B. Saw, W. Xi, B. Ladoux and C. T. Lim. Biological Tissues as Active Nematic Liquid Crystals. *Adv. Mater.* **30**(47), 1802579, 2018. DOI: 10.1002/adma.201802579. eprint: https://onlinelibrary.wiley.com/doi/pdf/10.1002/adma.201802579. (Cit. on p. 35).

[182] D. Shao, W.-J. Rappel and H. Levine. Computational Model for Cell Morphodynamics. *Phys. Rev. Lett.* **105**, 108104, 2010. DOI: 10.1103/PhysRevLett.105.108104. (Cit. on p. 35).

[183] I. S. Aranson. *Physical Models of Cell Motility*. Springer International Publishing, Switzerland, 2016. (Cit. on p. 35).

[184] F. Thueroff, A. Goychuk, M. Reiter and E. Frey. Bridging the gap between single cell migration and collective dynamics. bioRxiv/548677, 2019. DOI: 10.1101/548677. eprint: https://www.biorxiv.org/content/early/2019/02/13/548677.full.pdf. (Cit. on p. 35).

[185] M. Poujade, E. Grasland-Mongrain, A. Hertzog, J. Jouanneau, P. Chavrier, B. Ladoux, A. Buguin and P. Silberzan. Collective migration of an epithelial monolayer in response to a model wound. *Proc. Natl. Acad. Sci. U. S. A.* **104**, 15988–15993, 2007. (Cit. on p. 35).

[186] X. Trepat, M. R. Wasserman, T. E. Angelini, E. Millet, D. A. Weitz, J. P. Butler and J. J. Fredberg. Physical forces during collective cell migration. *Nat. Phys.* **5**(6), 426, 2009. (Cit. on p. 35).

[187] S. Mark, R. Shlomovitz, N. S. Gov, M. Poujade, E. Grasland-Mongrain and P. Silberzan. Physical model of the dynamic instability in an expanding cell culture. *Biophys. J.* **98**, 361–370, 2010. (Cit. on p. 35).

[188] W. Demtröder. *Reale feste und flüssige Körper*. Springer Berlin Heidelberg, Berlin, Heidelberg, 2008. Pp. 169–202. DOI: 10.1007/978-3-540-79295-6_6. (Cit. on p. 37).

[189] A. D. Rey and E. E. Herrera-Valencia. Dynamic wetting model for the isotropic-to-nematic transition over a flat substrate. *Soft Matter* **10**, 1611–1620, 2014. DOI: 10.1039/C3SM52034J. (Cit. on pp. 37, 59).

[190] S. Paliwal, V. Prymidis, L. Filion and M. Dijkstra. Non-equilibrium surface tension of the vapour-liquid interface of active Lennard-Jones particles. *The Journal of Chemical Physics* **147**(8), 084902, 2017. DOI: 10.1063/1.4989764. eprint: https://doi.org/10.1063/1.4989764. (Cit. on pp. 37, 38, 59).

[191] T. Speck. Collective forces in scalar active matter. *Soft Matter* **16**, 2652–2663, 2020. DOI: 10.1039/D0SM00176G. (Cit. on pp. 37, 59).

[192] C. F. Lee. Interface stability, interface fluctuations, and the Gibbs–Thomson relationship in motility-induced phase separations. *Soft Matter* **13**, 376–385, 2017. DOI: 10.1039/C6SM01978A. (Cit. on pp. 37, 38).

[193] T. Speck and R. L. Jack. Ideal bulk pressure of active Brownian particles. *Phys. Rev. E* **93**, 062605, 2016. DOI: 10.1103/PhysRevE.93.062605. (Cit. on p. 37).

[194] E. Tjhung, C. Nardini and M. E. Cates. Cluster Phases and Bubbly Phase Separation in Active Fluids: Reversal of the Ostwald Process. *Phys. Rev. X* **8**, 031080, 2018. DOI: 10.1103/PhysRevX.8.031080. (Cit. on pp. 37, 38).

[195] S. Das, G. Gompper and R. G. Winkler. Local stress and pressure in an inhomogeneous system of spherical active Brownian particles. *Scientific Reports* **9**(1), 6608, 2019. DOI: 10.1038/s41598-019-43077-x. (Cit. on p. 37).

[196] T. Speck, J. Bialké, A. M. Menzel and H. Löwen. Effective Cahn-Hilliard Equation for the Phase Separation of Active Brownian Particles. *Phys. Rev. Lett.* **112**, 218304, 2014. DOI: 10.1103/PhysRevLett.112.218304. (Cit. on p. 38).

[197] L. Rapp, F. Bergmann and W. Zimmermann. Systematic extension of the Cahn-Hilliard model for motility-induced phase separation. *The European Physical Journal E* **42**(5), 57, 2019. DOI: 10.1140/epje/i2019-11825-8. (Cit. on p. 38).

[198] J. Berry, C. P. Brangwynne and M. Haataja. Physical principles of intracellular organization via active and passive phase transitions. *Reports on Progress in Physics* **81**(4), 046601, 2018. DOI: 10.1088/1361-6633/aaa61e. (Cit. on p. 38).

[199] C. A. Weber, D. Zwicker, F. Jülicher and C. F. Lee. Physics of active emulsions. *Reports on Progress in Physics* **82**(6), 064601, 2019. DOI: 10.1088/1361-6633/ab052b. (Cit. on p. 38).

[200] M. L. Blow, M. Aqil, B. Liebchen and D. Marenduzzo. Motility of active nematic films driven by "active anchoring". *Soft Matter* **13**, 6137–6144, 2017. DOI: 10.1039/C7SM00325K. (Cit. on pp. 42–44, 58).

[201] P. Yue, J. J. Feng, C. Liu and J. Shen. A diffuse-interface method for simulating two-phase flows of complex fluids. *Journal of Fluid Mechanics* **515**, 293–317, 2004. DOI: 10.1017/S0022112004000370. (Cit. on p. 43).

[202] J.-F. Joanny and S. Ramaswamy. A drop of active matter. *Journal of Fluid Mechanics* **705**, 46–57, 2012. DOI: 10.1017/jfm.2012.131. (Cit. on pp. 45, 58, 59).

[203] S. Trinschek, F. Stegemerten, K. John and U. Thiele. Thin-film modeling of resting and moving active droplets. *Phys. Rev. E* **101**, 062802, 2020. DOI: 10.1103/PhysRevE.101.062802. (Cit. on pp. 45, 56, 58, 59).

[204] E. Tjhung, A. Tiribocchi, D. Marenduzzo and M. E. Cates. A minimal physical model captures the shapes of crawling cells. *Nature Communications* **6**(1), 5420, 2015. DOI: 10.1038/ncomms6420. (Cit. on pp. 45, 58, 59).

[205] D. Khoromskaia and G. P. Alexander. Motility of active fluid drops on surfaces. *Phys. Rev. E* **92**, 062311, 2015. DOI: 10.1103/PhysRevE.92.062311. (Cit. on pp. 45, 58, 59).

[206] A. Loisy, J. Eggers and T. B. Liverpool. How many ways a cell can move: the modes of self-propulsion of an active drop. *Soft Matter* **16**, 3106–3124, 2020. DOI: 10.1039/D0SM00070A. (Cit. on pp. 45, 46, 58, 59).

[207] A. Loisy, J. Eggers and T. B. Liverpool. Tractionless Self-Propulsion of Active Drops. *Phys. Rev. Lett.* **123**, 248006, 2019. DOI: 10.1103/PhysRevLett.123.248006. (Cit. on p. 46).

[208] P. de Gennes and J. Prost. *The Physics of Liquid Crystals*. International Series of Monogr. Clarendon Press, 1993. (Cit. on p. 49).

[209] C. Braga, E. R. Smith, A. Nold, D. N. Sibley and S. Kalliadasis. The pressure tensor across a liquid-vapour interface. *The Journal of Chemical Physics* **149**(4), 044705, 2018. DOI: 10.1063/1.5020991. (Cit. on p. 59).

[210] A. Alizadeh Pahlavan, L. Cueto-Felgueroso, A. E. Hosoi, G. H. McKinley and R. Juanes. Thin films in partial wetting: stability, dewetting and coarsening. *Journal of Fluid Mechanics* **845**, 642–681, 2018. DOI: 10.1017/jfm.2018.255. (Cit. on p. 59).

[211] G. Tortora and B. Derrickson. *Principles of Anatomy and Physiology*. Wiley, 2016. Chap. 4. (Cit. on p. 61).

[212] M. S. Steinberg. Differential adhesion in morphogenesis: a modern view. *Current Opinion in Genetics & Development* **17**(4) Pattern formation and developmental mechanisms, 281–286, 2007. DOI: https://doi.org/10.1016/j.gde.2007.05.002. (Cit. on pp. 61, 63, 81, 117).

[213] J. A. Farrell, Y. Wang, S. J. Riesenfeld, K. Shekhar, A. Regev and A. F. Schier. Single-cell reconstruction of developmental trajectories during zebrafish embryogenesis. *Science* **360**(6392), 2018. DOI: 10.1126/science.aar3131. eprint: https://science.sciencemag.org/content/360/6392/eaar3131.full.pdf. (Cit. on pp. 61, 117).

[214] O. Viader-Llargués, V. Lupperger, L. Pola-Morell, C. Marr and H. López-Schier. Live cell-lineage tracing and machine learning reveal patterns of organ regeneration. *eLife* **7**, e30823, 2018. DOI: 10.7554/eLife.30823. (Cit. on pp. 61, 117).

[215] D. A. Lauffenburger and A. F. Horwitz. Cell Migration: A Physically Integrated Molecular Process. *Cell* **84**(3), 359–369, 1996. DOI: 10.1016/S0092-8674(00)81280-5. (Cit. on p. 61).

[216] T. Risler. *Cytoskeleton and Cell Motility*. Ed. by R. A. Meyers. Springer New York, New York, NY, 2009. Pp. 1–53. DOI: 10.1007/978-3-642-27737-5_112-3. (Cit. on p. 61).

[217] M. Striebel, I. R. Graf and E. Frey. A Mechanistic View of Collective Filament Motion in Active Nematic Networks. *Biophysical Journal* **118**(2), 313–324, 2020. DOI: https://doi.org/10.1016/j.bpj.2019.11.3387. (Cit. on p. 61).

[218] A. Haeger, K. Wolf, M. M. Zegers and P. Friedl. Collective cell migration: guidance principles and hierarchies. *Trends in Cell Biology* **25**(9), 556–566, 2015. DOI: 10.1016/j.tcb.2015.06.003. (Cit. on p. 61).

[219] C. D. Lawson and A. J. Ridley. Rho GTPase signaling complexes in cell migration and invasion. *The Journal of cell biology* **217**(2), 447–457, 2018. DOI: 10.1083/jcb.201612069. (Cit. on pp. 61, 68).

[220] M. Reffay, M. C. Parrini, O. Cochet-Escartin, B. Ladoux, A. Buguin, S. Coscoy, F. Amblard, J. Camonis and P. Silberzan. Interplay of RhoA and mechanical forces in collective cell migration driven by leader cells. *Nature Cell Biology* **16**(3), 217–223, 2014. DOI: 10.1038/ncb2917. (Cit. on p. 61).

[221] B. Ladoux, R.-M. Mège and X. Trepat. Front–Rear Polarization by Mechanical Cues: From Single Cells to Tissues. *Trends in Cell Biology* **26**(6), 420–433, 2016. DOI: 10.1016/j.tcb.2016.02.002. (Cit. on p. 61).

[222] W. Xi, T. B. Saw, D. Delacour, C. T. Lim and B. Ladoux. Material approaches to active tissue mechanics. *Nature Reviews Materials* **4**(1), 23–44, 2019. DOI: 10.1038/s41578-018-0066-z. (Cit. on pp. 62, 63).

[223] A. Brú, S. Albertos, J. Luis Subiza, J. L. García-Asenjo and I. Brú. The Universal Dynamics of Tumor Growth. *Biophysical Journal* **85**(5), 2948–2961, 2003. DOI: 10.1016/S0006-3495(03)74715-8. (Cit. on p. 62).

[224] M. Poujade, E. Grasland-Mongrain, A. Hertzog, J. Jouanneau, P. Chavrier, B. Ladoux, A. Buguin and P. Silberzan. Collective migration of an epithelial monolayer in response to a model wound. *Proceedings of the National Academy of Sciences* **104**(41), 15988–15993, 2007. DOI: 10.1073/pnas.0705062104. eprint: https://www.pnas.org/content/104/41/15988.full.pdf. (Cit. on p. 62).

[225] V. Hakim and P. Silberzan. Collective cell migration: a physics perspective. *Reports on Progress in Physics* **80**(7), 076601, 2017. (Cit. on pp. 62, 63, 65).

[226] B. Ladoux and R.-M. Mège. Mechanobiology of collective cell behaviours. *Nature Reviews Molecular Cell Biology* **18**(12), 743–757, 2017. DOI: 10.1038/nrm.2017.98. (Cit. on pp. 62, 65).

[227] L. Petitjean, M. Reffay, E. Grasland-Mongrain, M. Poujade, B. Ladoux, A. Buguin and P. Silberzan. Velocity Fields in a Collectively Migrating Epithelium. *Biophysical Journal* **98**(9), 1790–1800, 2010. DOI: 10.1016/j.bpj.2010.01.030. (Cit. on p. 62).

[228] L. Atia *et al.* Geometric constraints during epithelial jamming. *Nature physics* **14**, 613–620, 2018. DOI: 10.1038/s41567-018-0089-9. (Cit. on p. 62).

[229] A. Palamidessi *et al.* Unjamming overcomes kinetic and proliferation arrest in terminally differentiated cells and promotes collective motility of carcinoma. *Nature Materials* **18**(11), 1252–1263, 2019. DOI: 10.1038/s41563-019-0425-1. (Cit. on p. 62).

[230] J. A. Mitchel *et al.* In primary airway epithelial cells, the unjamming transition is distinct from the epithelial-to-mesenchymal transition. *Nature Communications* **11**(1), 5053, 2020. DOI: 10.1038/s41467-020-18841-7. (Cit. on p. 62).

[231] T. Chen, T. B. Saw, R.-M. Mège and B. Ladoux. Mechanical forces in cell monolayers. *Journal of Cell Science* **131**(24), 2018. DOI: 10.1242/jcs.218156. eprint: https://jcs.biologists.org/content/131/24/jcs218156.full.pdf. (Cit. on p. 62).

[232] A. Brugués, E. Anon, V. Conte, J. H. Veldhuis, M. Gupta, J. Colombelli, J. J. Muñoz, G. W. Brodland, B. Ladoux and X. Trepat. Forces driving epithelial wound healing. *Nature Physics* **10**(9), 683–690, 2014. DOI: 10.1038/nphys3040. (Cit. on p. 62).

[233] R. Vincent, E. Bazellières, C. Pérez-González, M. Uroz, X. Serra-Picamal and X. Trepat. Active Tensile Modulus of an Epithelial Monolayer. *Phys. Rev. Lett.* **115**, 248103, 2015. DOI: 10.1103/PhysRevLett.115.248103. (Cit. on p. 62).

[234] X. Yang, D. Bi, M. Czajkowski, M. Merkel, M. L. Manning and M. C. Marchetti. Correlating cell shape and cellular stress in motile confluent tissues. *Proceedings of the National Academy of Sciences* **114**(48), 12663–12668, 2017. DOI: 10.1073/pnas.1705921114. eprint: https://www.pnas.org/content/114/48/12663.full.pdf. (Cit. on p. 62).

[235] N. Noll, M. Mani, I. Heemskerk, S. J. Streichan and B. I. Shraiman. Active tension network model suggests an exotic mechanical state realized in epithelial tissues. *Nature Physics* **13**(12), 1221–1226, 2017. DOI: 10.1038/nphys4219. (Cit. on p. 62).

[236] A. Labernadie and X. Trepat. Sticking, steering, squeezing and shearing: cell movements driven by heterotypic mechanical forces. *Current Opinion in Cell Biology* **54** Cell Dynamics, 57–65, 2018. DOI: https://doi.org/10.1016/j.ceb.2018.04.008. (Cit. on p. 62).

[237] T. Zhao, Y. Zhang, Q. Wei, X. Shi, P. Zhao, L.-Q. Chen and S. Zhang. Active cell-matrix coupling regulates cellular force landscapes of cohesive epithelial monolayers. *npj Computational Materials* **4**(1), 10, 2018. DOI: 10.1038/s41524-018-0069-8. (Cit. on p. 62).

[238] N. G. Patel, A. Nguyen, N. Xu, S. Ananthasekar, D. F. Alvarez, T. Stevens and D. T. Tambe. Unleashing shear: Role of intercellular traction and cellular moments in collective cell migration. *Biochemical and Biophysical Research Communications* **522**(2), 279–285, 2020. DOI: https://doi.org/10.1016/j.bbrc.2019.11.048. (Cit. on p. 62).

[239] X. Trepat and J. J. Fredberg. Plithotaxis and emergent dynamics in collective cellular migration. *Trends in Cell Biology* **21**(11), 638–646, 2011. DOI: https://doi.org/10.1016/j.tcb.2011.06.006. (Cit. on p. 62).

[240] R. Sunyer *et al.* Collective cell durotaxis emerges from long-range intercellular force transmission. *Science* **353**(6304), 1157–1161, 2016. DOI: 10.1126/science.aaf7119. eprint: https://science.sciencemag.org/content/353/6304/1157.full.pdf. (Cit. on p. 62).

[241] R. Mayor and C. Carmona-Fontaine. Keeping in touch with contact inhibition of locomotion. *Trends in Cell Biology* **20**(6), 319–328, 2010. DOI: 10.1016/j.tcb.2010.03.005. (Cit. on p. 62).

[242] J. d'Alessandro, A. P. Solon, Y. Hayakawa, C. Anjard, F. Detcheverry, J.-P. Rieu and C. Rivière. Contact enhancement of locomotion in spreading cell colonies. *Nature Physics* **13**(10), 999–1005, 2017. DOI: 10.1038/nphys4180. (Cit. on p. 62).

[243] D. Li and Y.-l. Wang. Coordination of cell migration mediated by site-dependent cell–cell contact. *Proceedings of the National Academy of Sciences* **115**(42), 10678–10683, 2018. DOI: 10.1073/pnas.1807543115. eprint: https://www.pnas.org/content/115/42/10678.full.pdf. (Cit. on p. 62).

[244] M. George, F. Bullo and O. Campàs. Connecting individual to collective cell migration. *Scientific Reports* **7**(1), 9720, 2017. DOI: 10.1038/s41598-017-10069-8. (Cit. on pp. 62, 64).

[245] D. B. Brückner, N. Arlt, A. Fink, P. Ronceray, J. O. Rädler and C. P. Broedersz. *Learning the dynamics of cell-cell interactions in confined cell migration*. 2020. arXiv: 2008.03978 [physics.bio-ph] (cit. on pp. 62, 64).

[246] O. Ilina and P. Friedl. Mechanisms of collective cell migration at a glance. *Journal of Cell Science* **122**(18), 3203–3208, 2009. DOI: 10.1242/jcs.036525. eprint: https://jcs.biologists.org/content/122/18/3203.full.pdf. (Cit. on p. 63).

[247] D. L. Barton, S. Henkes, C. J. Weijer and R. Sknepnek. Active Vertex Model for cell-resolution description of epithelial tissue mechanics. *PLOS Computational Biology* **13**(6), 1–34, 2017. DOI: 10.1371/journal.pcbi.1005569. (Cit. on pp. 63, 66, 81).

[248] A. Hayer, L. Shao, M. Chung, L.-M. Joubert, H. W. Yang, F.-C. Tsai, A. Bisaria, E. Betzig and T. Meyer. Engulfed cadherin fingers are polarized junctional structures between collectively migrating endothelial cells. *Nature Cell Biology* **18**(12), 1311–1323, 2016. DOI: 10.1038/ncb3438. (Cit. on pp. 63, 81).

[249] M. Vishwakarma, J. P. Spatz and T. Das. Mechanobiology of leader–follower dynamics in epithelial cell migration. *Current Opinion in Cell Biology* **66**, 97–103, 2020. DOI: https://doi.org/10.1016/j.ceb.2020.05.007. (Cit. on p. 63).

[250] M. Vishwakarma, B. Thurakkal, J. P. Spatz and T. Das. Dynamic heterogeneity influences the leader-follower dynamics during epithelial wound closure. *Philosophical Transactions of the Royal Society B: Biological Sciences* **375**(1807), 20190391, 2020. DOI: 10.1098/rstb.2019.0391. eprint: https://royalsocietypublishing.org/doi/pdf/10.1098/rstb.2019.0391. (Cit. on pp. 63, 81).

[251] K. Doxzen, S. R. K. Vedula, M. C. Leong, H. Hirata, N. S. Gov, A. J. Kabla, B. Ladoux and C. T. Lim. Guidance of collective cell migration by substrate geometry. *Integrative Biology* **5**(8), 1026–1035, 2013. DOI: 10.1039/c3ib40054a. eprint: https://academic.oup.com/ib/article-pdf/5/8/1026/27302155/c3ib40054a.pdf. (Cit. on p. 63).

[252] K.-H. Nam, P. Kim, D. K. Wood, S. Kwon, P. P. Provenzano and D.-H. Kim. Multiscale Cues Drive Collective Cell Migration. *Scientific Reports* **6**(1), 29749, 2016. DOI: 10.1038/srep29749. (Cit. on pp. 63, 65, 81).

[253] M. B. Mazalan, M. A. Ramlan, J. H. Shin and T. Ohashi. Effect of Geometric Curvature on Collective Cell Migration in Tortuous Microchannel Devices. *Micromachines* **11**(7), 659, 2020. DOI: 10.3390/mi11070659. (Cit. on pp. 63, 65, 81).

[254] D. Sarkar, G. Gompper and J. Elgeti. *A minimal model for structure, dynamics, and tension of monolayered cell colonies*. 2020. arXiv: 2006.04519 [physics.bio-ph] (cit. on p. 63).

[255] S. Banerjee and M. C. Marchetti. *Continuum models of collective cell migration*. 2018. arXiv: 1805.06531 [physics.bio-ph] (cit. on p. 63).

[256] C. Blanch-Mercader, P. Guillamat, A. Roux and K. Kruse. *Quantifying material properties of cell monolayers by analyzing integer topological defects*. 2020. arXiv: 2006.01575 [cond-mat.soft] (cit. on p. 63).

[257] X. Trepat and E. Sahai. Mesoscale physical principles of collective cell organization. *Nature Physics* **14**(7), 671–682, 2018. DOI: 10.1038/s41567-018-0194-9. (Cit. on p. 63).

[258] A. G. Fletcher, M. Osterfield, R. E. Baker and S. Y. Shvartsman. Vertex Models of Epithelial Morphogenesis. *Biophysical Journal* **106**(11), 2291–2304, 2014. DOI: 10.1016/j.bpj.2013.11.4498. (Cit. on pp. 63, 66).

[259] S. Alt, P. Ganguly and G. Salbreux. Vertex models: from cell mechanics to tissue morphogenesis. *Philosophical Transactions of the Royal Society B: Biological Sciences* **372**(1720), 20150520, 2017. DOI: 10.1098/rstb.2015.0520. eprint: https://royalsocietypublishing.org/doi/pdf/10.1098/rstb.2015.0520. (Cit. on pp. 63, 66).

[260] S. Koride, A. J. Loza and S. X. Sun. Epithelial vertex models with active biochemical regulation of contractility can explain organized collective cell motility. *APL Bioengineering* **2**(3), 031906, 2018. DOI: 10.1063/1.5023410. eprint: https://doi.org/10.1063/1.5023410. (Cit. on pp. 63, 66).

[261] B. Buchmann, L. Meixner, P. Fernandez, F. Hutterer, M. Raich, C. Scheel and A. Bausch. Mechanical plasticity of the ECM directs invasive branching morphogenesis in human mammary gland organoids. *bioRxiv*, 2019. DOI: 10.1101/860015. eprint: https://www.biorxiv.org/content/early/2019/11/29/860015.full.pdf. (Cit. on p. 65).

[262] A. W. Holle, N. Govindan Kutty Devi, K. Clar, A. Fan, T. Saif, R. Kemkemer and J. P. Spatz. Cancer Cells Invade Confined Microchannels via a Self-Directed Mesenchymal-to-Amoeboid Transition. *Nano Letters* **19**(4) PMID: 30775927, 2280–2290, 2019. DOI: 10.1021/acs.nanolett.8b04720. eprint: https://doi.org/10.1021/acs.nanolett.8b04720. (Cit. on p. 65).

[263] P. Kameritsch and J. Renkawitz. Principles of Leukocyte Migration Strategies. *Trends in Cell Biology* **30**(10), 818–832, 2020. DOI: https://doi.org/10.1016/j.tcb.2020.06.007. (Cit. on p. 65).

[264] W. Xi, S. Sonam, T. Beng Saw, B. Ladoux and C. Teck Lim. Emergent patterns of collective cell migration under tubular confinement. *Nature Communications* **8**(1), 1517, 2017. DOI: 10.1038/s41467-017-01390-x. (Cit. on p. 65).

[265] M. R. Shaebani, A. Wysocki, R. G. Winkler, G. Gompper and H. Rieger. Computational models for active matter. *Nature Reviews Physics* **2**(4), 181–199, 2020. DOI: 10.1038/s42254-020-0152-1. (Cit. on p. 65).

[266] H. Chaté, F. Ginelli, G. Grégoire, F. Peruani and F. Raynaud. Modeling collective motion: variations on the Vicsek model. *The European Physical Journal B* **64**(3), 451–456, 2008. DOI: 10.1140/epjb/e2008-00275-9. (Cit. on p. 65).

[267] V. Tarle, A. Ravasio, V. Hakim and N. S. Gov. Modeling the finger instability in an expanding cell monolayer. *Integr. Biol.* **7**, 1218–1227, 2015. DOI: 10.1039/C5IB00092K. (Cit. on p. 65).

[268] S. Banerjee and M. C. Marchetti. *Continuum Models of Collective Cell Migration*. Ed. by C. A. M. La Porta and S. Zapperi. Springer International Publishing, Cham, 2019. Pp. 45–66. DOI: 10.1007/978-3-030-17593-1_4. (Cit. on p. 66).

[269] F. Zhou, S. A. Schaffer, C. Schreiber, F. J. Segerer, A. Goychuk, E. Frey and J. O. Rädler. Quasi-periodic migration of single cells on short microlanes. *PLOS ONE* **15**(4), 1–19, 2020. DOI: 10.1371/journal.pone.0230679. (Cit. on pp. 66, 85).

[270] A. Goychuk, D. B. Brückner, A. W. Holle, J. P. Spatz, C. P. Broedersz and E. Frey. *Morphology and Motility of Cells on Soft Substrates*. 2018. arXiv: 1808.00314 [physics.bio-ph] (cit. on pp. 67, 81, 85).

[271] A. Szabó, M. Melchionda, G. Nastasi, M. L. Woods, S. Campo, R. Perris and R. Mayor. In vivo confinement promotes collective migration of neural crest cells. *Journal of Cell Biology* **213**(5), 543–555, 2016. DOI: 10.1083/jcb.201602083. eprint: https://rupress.org/jcb/article-pdf/213/5/543/1372040/jcb_201602083.pdf. (Cit. on pp. 67, 85).

[272] H. Khataee, A. Czirok and Z. Neufeld. Multiscale modelling of motility wave propagation in cell migration. *Scientific Reports* **10**(1), 8128, 2020. DOI: 10.1038/s41598-020-63506-6. (Cit. on p. 67).

[273] S. Banerjee, M. L. Gardel and U. S. Schwarz. The Actin Cytoskeleton as an Active Adaptive Material. *Annual Review of Condensed Matter Physics* **11**(1), 421–439, 2020. DOI: 10.1146/annurev-conmatphys-031218-013231. eprint: https://doi.org/10.1146/annurev-conmatphys-031218-013231. (Cit. on p. 68).

[274] C. Bechinger and E. Frey. *Colloids on Patterned Substrates*. John Wiley & Sons, Ltd, 2007. Chap. 3, pp. 87–158. DOI: https://doi.org/10.1002/9783527682300.ch3. eprint: https://onlinelibrary.wiley.com/doi/pdf/10.1002/9783527682300.ch3. (Cit. on p. 72).

[275] T. Schwann, H. Smith and M. J. Schleiden. *Microscopical researches into the accordance in the structure and growth of animals and plants.* https://www.biodiversitylibrary.org/bibliography/17276 — "Contributions to phytogenesis, translated from the German of Dr. M. J. Schleiden": p. [229]-268. London,Sydenham Society, 1847. P. 314. (Cit. on p. 72).

[276] D. B. Staple, R. Farhadifar, J.-C. Röper, B. Aigouy, S. Eaton and F. Jülicher. Mechanics and remodelling of cell packings in epithelia. *The European Physical Journal E* **33**(2), 117–127, 2010. DOI: 10.1140/epje/i2010-10677-0. (Cit. on p. 73).

[277] R. van Drongelen, T. Vazquez-Faci, T. A. Huijben, M. van der Zee and T. Idema. Mechanics of epithelial tissue formation. *Journal of Theoretical Biology* **454**, 182–189, 2018. DOI: https://doi.org/10.1016/j.jtbi.2018.06.002. (Cit. on p. 73).

[278] M. C. Gibson, A. B. Patel, R. Nagpal and N. Perrimon. The emergence of geometric order in proliferating metazoan epithelia. *Nature* **442**(7106), 1038–1041, 2006. DOI: 10.1038/nature05014. (Cit. on p. 73).

[279] X. H. Zheng and J. C. Earnshaw. On the Lindemann criterion in 2D. *Europhysics Letters (EPL)* **41**(6), 635–640, 1998. DOI: 10.1209/epl/i1998-00205-7. (Cit. on pp. 74, 105).

[280] B. Illing, S. Fritschi, H. Kaiser, C. L. Klix, G. Maret and P. Keim. Mermin–Wagner fluctuations in 2D amorphous solids. *Proceedings of the National Academy of Sciences* **114**(8), 1856–1861, 2017. DOI: 10.1073/pnas.1612964114. eprint: https://www.pnas.org/content/114/8/1856.full.pdf. (Cit. on pp. 74, 80, 105).

[281] Q.-H. Wei, C. Bechinger and P. Leiderer. Single-File Diffusion of Colloids in One-Dimensional Channels. *Science* **287**(5453), 625–627, 2000. DOI: 10.1126/science.287.5453.625. eprint: https://science.sciencemag.org/content/287/5453/625.full.pdf. (Cit. on p. 77).

[282] J.-F. Rupprecht, K. H. Ong, J. Yin, A. Huang, H.-H.-Q. Dinh, A. P. Singh, S. Zhang, W. Yu and T. E. Saunders. Geometric constraints alter cell arrangements within curved epithelial tissues. *Molecular Biology of the Cell* **28**(25) PMID: 28978739, 3582–3594, 2017. DOI: 10.1091/mbc.e17-01-0060. eprint: https://doi.org/10.1091/mbc.e17-01-0060. (Cit. on p. 81).

[283] M. Vishwakarma, J. Di Russo, D. Probst, U. S. Schwarz, T. Das and J. P. Spatz. Mechanical interactions among followers determine the emergence of leaders in migrating epithelial cell collectives. *Nature Communications* **9**(1), 3469, 2018. DOI: 10.1038/s41467-018-05927-6. (Cit. on p. 81).

[284] K. Mardia and P. Jupp. *Directional Statistics*. Wiley Series in Probability and Statistics. Wiley, 2009. (Cit. on p. 103).

[285] L. Wolpert. *Principles of Development*. Oxford University Press, 2002. (Cit. on p. 117).

# Acknowledgements

I would like to thank all the people who supported me during my doctoral studies. First of all, this applies to my supervisor Erwin Frey without whom the whole journey would not have even started. Discussions with you were a great source of inspiration and provided me with new ideas, routes to follow and suggestions for improvement. In course of the various teaching jobs I also gained a broad overview over many fields of physics that not only benefited my actual work but also broadened my view and shaped my general understanding of the world. Same holds for the various travels that you made possible for me, also these were not only beneficial for my scientific output, but also got me to know great people and new landscapes.

Most outstanding were certainly my visits to Oxford where Julia Yeomans and her group for times almost gave me a second home on the historic premises of the colleges of Oxford. Although my stays always felt like passing by too fast I profited immensely from discussion and close collaboration with the people there and not only that: I have best memories about football, which was always number one priority, evenings in the pub, and punting on the canals. I am grateful for all of that.

That being said, it becomes already clear that science is not only about the captains, but to (at least) the same amount also about the teams. Special thanks for countless discussion on science-related and not science-related talking go to: Philipp Geiger (for being an equally tolerant as well as inspiring office mate), Andriy Goychuck (who knows a lot about cells and how to model them and was a great collaborator in teaching me the CPM), and Cornelius Weig (who had major influence on my attitude towards programming and was my personal guide during the first time at the chair). Furthermore to: Caroline Lesperance, Marianne Bauer (and to her parents for providing their home for a very joyful work retreat), Peter Baumgartner, Fridtjof Brauns, David Brückner (who knows a lot about cells), Frau Brunner (who sleeps too little), Chase Broedersz, Raphael Goll, Grześ Gradziuk, his cousin Gyödzsü, Timo Krüger, Ivan Maryshev, Joris Messelink, David Muramatsu (-san; thank you for organising the amazing trip to Japan), Moritz Striebel, Manon Wigbers, Laeschkir Würthner (especially for being an admin), Alexander Ziepke (especially for being an admin), Silke Bergeler, Jonas Denk, Federico Gnesotto, Isabella Graf, Jacob Halatek, Korbinian Pöppel, Lorenz Huber, Johannes Knebel, Matthias Lechner (especially for being an admin), CKarsten Miermans (the most social animal), Federica Mura, Matthias Rank, Emanuel Reithmann (the most thirsty animal), Markus F. Weber, Christoph A. Weber (who introduced me to active matter

in my master thesis), Karl Wienand, Patrick Wilke (especially for being an admin), and the rest of Broedersz/Frey group.

Additional gratitude I owe to Marianne Bauer, Isabella Graf, Sophia Schaffer, and Alexander Ziepke for proofreading this thesis.

In Oxford, my special thanks go to Amin Doostmohammadi for caring for me like a second supervisor and to Romain Mueller who supplied me with the most beautiful code I have ever seen and provided all the support for me to make it uglier. Additionally for great discussions and company: Kristian Thijsen, Luuk Metselaar, Fanlong Meng, Daiki Matsunaga, Ryan Hughes, Andreas Zöttl, and Ousmane Kodio.

I am particularly thankful also to Shinji Deguchi who gave me the opportunity to lecture in front of his students and to Daiki Matsunaga (again), who showed to me the beauty of his home country and spared no efforts to make my stay as enjoyable as possible. You both were wonderful hosts to me in Osaka.

I must not forget to thank the LMU Physics community for their support. They provide an amazing environment for physics graduate students, not only by funding travels and organising workshops or seminars with renowned speakers and Leberkas. It is also due to the positive atmosphere that makes being part of Munich physics enjoyable. This is due to institutions like CeNS, SFB1032, or NIM and the associated people as Marilena Pinto, Susanne Henning, or Joachim Rädler. In a similar way, I profited from the the TMP master's programme and Robert Helling's dedication.

It is also in this environment that I had the pleasure to meet Sophia Schaffer, Matthias Zorn, and Joachim Rädler who were so patient in discussing with me about possible research questions and methods and shared their ideas with me. I am also grateful to have had co-students like Kathi Huber, Jan Dziewior, Markus Götz, Jakob Haidl, Christopher Bremer, Nanni Giunta, Magnus Bauer, Micha Panchenko, Benjamin Spreng, Han Yu, and many more.

Likewise I must not forget the people who introduced me to science in my bachelor's. It was in the group of Andreas Herz, where I as a bachelor student was accepted as a full member from day one. This was especially due to my supervisors Andreas Herz, Martin Stemmler, and Alexander Mathis, but also the other members and people from the Munich computational neuroscience community, among these Yuan Chun-Wei, Olivia Haas, Arne Harz, Franziska Kümpfbeck, Simon Lehnert, Alex Loebel, Johannes Nagele, Johannes Nehrkorn, Dinu Patirniche, and Monika Volk.

Last but not least, I would like to thank my friends and family for the ongoing support. Especially without my mother's backing this (as much as my studies in general) would probably have not been possible. I also want to thank Max Fesl for continuously questioning my profession in intense philosophical discussions on the topic "what does physics have to say anyways?". He maybe is a bit responsible for the far-fetching introduction.

To all of you that I have forgotten to mention go my sincere apology and my deepest gratitude for everything you have done for me.